Energy &
Environmental
Science

ROYAL SOCIETY
OF CHEMISTRY

REVIEW

View Article Online
View Journal | View Issue

Cite this: *Energy Environ. Sci.*, 2021, **14**, 602

Electro-chemo-mechanics of lithium in solid state lithium metal batteries

Yongfu Tang,[ab] Liqiang Zhang,*[a] Jingzhao Chen,[a] Haiming Sun,[a] Tingting Yang,[a] Qiunan Liu,[a] Qiao Huang,*[c] Ting Zhu[d] and Jianyu Huang *[ac]

Using lithium as the anode material to achieve high energy density lithium-ion/metal batteries is the ultimate goal of energy storage technology. A recent development of solid state electrolytes (SSEs) with high ionic conductivity holds great promise for enabling the practical applications of solid state lithium metal batteries (SSLMBs), as the high mechanical strength of SSEs can be harnessed to suppress dendrite growth. However, the application of SSLMBs is hampered by the new multifold problems from the solid–solid contact to dendrites to deleterious interfacial reactions between lithium and the SSEs. In this burgeoning field of SSLMBs, it is imperative to understand the fundamental science of these emerging problems at a very basic level before the application of SSLMBs can be realized. These problems are inter-related and they arise from the intrinsic physical, chemical, and electro-chemo-mechanical properties of lithium. We start this review by providing a brief account of the history of lithium, and how it has evolved from the anode of primary lithium metal batteries to that of liquid electrolyte based rechargeable batteries and to that of SSE based SSLMBs. We then summarize the literature about the mechanical properties of bulk lithium, lithium pillars and lithium whiskers. We analyze from an electro-chemo-mechanical perspective how lithium dendrites penetrate through SSEs and cause short circuits in SSLMBs. We identify possible strategies to mitigate lithium dendrite propagation through SSEs, and summarize our understanding of the lithium reaction with various interfaces, such as Li/$Li_7La_3Zr_2O_{12}$, Li/polyethylene oxide, Li/Na-superionic conductor, and Li/sulfide, with the ultimate goal of developing strategies to mitigate detrimental interfacial reactions and maintain sustainable stable interfaces. We review briefly characterization tools to address the challenging issues in SSLMBs. We conclude by pointing out the outstanding issues in SSLMBs.

Received 7th August 2020,
Accepted 23rd November 2020

DOI: 10.1039/d0ee02525a

rsc.li/ees

Broader context

Vehicle electrification and large scale grid energy storage require batteries with much better performance than the current technology. Liquid electrolyte based lithium ion batteries (LIBs) have reached their energy density limit of about 300 W h kg^{-1}; further increasing their energy density causes great safety concerns. In this context, solid state lithium metal batteries (SSLMBs) using solid state electrolytes (SSEs) pairing with a lithium metal anode promise much higher energy density and safety than current LIBs. However, SSLMBs have not realized their potential to date. In fact, detrimental lithium dendrite growth in SSLMBs is even worse than in liquid electrolyte LIBs. Moreover, the solid–solid contact between electrodes causes large interface resistance, exacerbating the performance of SSLMBs. Lithium dendrite growth and high interface impedance are two major roadblocks in developing SSLMBs. We review lithium mechanics and analyze from an electro-chemo-mechanical perspective how lithium dendrites penetrate through SSEs and cause short circuits in SSLMBs, and identify possible strategies to mitigate lithium dendrite growth. We summarize the lithium reaction with various interfaces, with the ultimate goal of developing strategies to mitigate detrimental interfacial reactions. We review briefly characterization tools to address the challenging issues, and conclude by pointing out the outstanding issues in SSLMBs.

---

[a] *Clean Nano Energy Center, State Key Laboratory of Metastable Materials Science and Technology, Yanshan University, Qinhuangdao 066004, P. R. China. E-mail: liqiangzhang85@163.com, jyhuang8@hotmail.com*
[b] *Hebei Key Laboratory of Applied Chemistry, School of Environmental and Chemical Engineering, Yanshan University, Qinhuangdao 066004, P. R. China*
[c] *School of Materials Science and Engineering, Xiangtan University, Xiangtan, Hunan 411105, P. R. China. E-mail: qiaoh@xtu.edu.cn*
[d] *Woodruff School of Mechanical Engineering, Georgia Institute of Technology, Atlanta, GA 30332, USA*

1. Introduction

Lithium is the lightest metal in the periodic table with a density of 0.534 g cm^{-3}, lighter even than water (density 1 g cm^{-3}). It is a soft, silvery-white alkali metal. It is very reactive with water and highly flammable, and thus must be stored in mineral oil. Fig. 1 gives a brief overview of the history and chronology of lithium and lithium based batteries. In 1817, the Swedish chemist Johan August Arfwedson isolated lithium salt from spodumene and petalite crystalline mineral compounds.[1,2] Pure lithium metal was isolated in 1821 by electrolysis of lithium oxide, and commercial production of lithium started in 1923 by electrolysis of lithium chloride.[1–3] In the mid-1800s lithium salts were used in the medical field to treat diseases ranging from gout to asthma to depression. In the early nineties, lithium chloride was used as a substitute for sodium-rich salt to treat heart diseases. Lithium salt is useful to treat mental illness. For example, Eskalith, Lithobid, Lithonate, and Lithotabs are important mood-stabilizing drugs in the treatment of bipolar disorder in humans.[2]

In the modern era, lithium and its compounds have several industrial applications such as high strength lightweight magnesium lithium alloys[4] and aluminum lithium alloys[5] for aerospace applications. Among all the lithium's applications, the most important ones are lithium ion batteries (LIBs) and lithium metal batteries (LMBs). Lithium has the highest specific capacity (3860 mA h g^{-1}) and the lowest chemical potential (Li^+/Li couple −3.05 V *vs.* SHE), making it a promising anode material for LMBs. In the 1970s a number of primary LMB systems were developed for military, medical and consumer electronics applications. The cathode materials include iodine (I_2), manganese dioxide (MnO_2), thionyl chloride ($SOCl_2$), sulfur dioxide (SO_2), copper oxide (CuO), carbon monofluoride (CF_x), silver vanadium

Yongfu Tang

Yongfu Tang received his PhD degree in Chemical Engineering in 2012 from the Dalian Institute of Chemical Physics, Chinese Academy of Sciences. In 2012, he joined Yanshan University to start his independent research studies. His current research interests mainly focus on the development of key materials and the in situ TEM studies for electrochemical energy conversion devices (including metal–air batteries, lithium–sulfur batteries, metal ion batteries, and supercapacitors). He has authored/coauthored over 60 research papers.

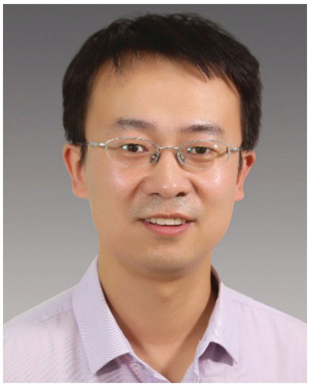

Liqiang Zhang

Liqiang Zhang received his PhD degree in materials science and engineering in 2012 from Zhejiang University. At present, he is a researcher in Yanshan University. His current research interests mainly focus on in situ TEM, particularly in battery materials. He has authored/coauthored over 100 research papers and filed 10 Chinese innovation patents.

Qiao Huang

Qiao Huang received his PhD degree in Materials Science and Engineering from Central South University in 2019. During his PhD from 2016 to 2019, he was a visiting scholar in Prof. Yushin's laboratory in the School of Materials Science and Engineering at the Georgia Institute of Technology. He was appointed as a lecturer in Xiangtan University in 2020. His research interests include cathode materials for rechargeable lithium metal batteries, lithium metal anodes and lithium batteries with solid electrolytes.

Jianyu Huang

Jianyu Huang received his PhD from the Institute of Metal Research, Chinese Academy of Sciences, in 1996. He has been working in the area of electron microscopy and its applications in nanoscience and energy technology for over 20 years. His current research interests focus on in situ studies of batteries and exploring new energy storage mechanisms. He is also interested in developing new technologies to enable cross length scale investigations of nano/energy materials under the influence of external stimuli such as pressure, temperature and gas. Huang's research goal is to correlate structure and composition with electron, phonon, ion, and mass transport properties in nano/energy materials.

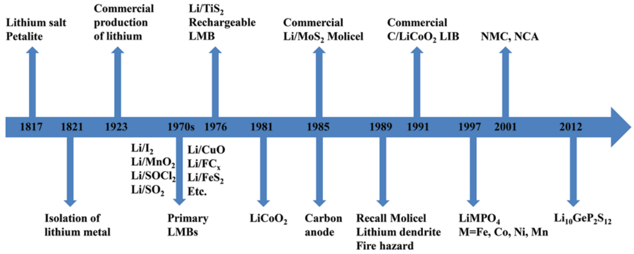

Fig. 1 History and chronology of lithium and lithium based batteries.

oxide ($Ag_2V_4O_{11}$), pyrite (FeS_2), copper sulfide (CuS), vanadium pentoxide (V_2O_5) and silver chromate (Ag_2CrO_4).[6–9] The research on Li/CF_x batteries is still ongoing with the main focus on improving their energy density and power density. The Li/CF_x primary battery with fluorinated graphene delivers a high energy density of 1075 W h kg^{-1} and an excellent power density of 21.46 kW kg^{-1} at a high current density of 10 A g^{-1}, and it has important military applications.[10] The Li/MnO_2 primary battery is still widely used in remote controls, meters, flashlights, and other light emitting devices.

The ever increasing energy storage demand stimulated the development of rechargeable LMBs. Whittingham was the first to create a rechargeable LMB using a lithium anode, $LiPF_6$ dissolved in propylene carbonate electrolyte and a TiS_2 single crystal cathode.[11] The electrochemical reaction occurred *via*: $x\mathrm{Li} + \mathrm{TiS_2} \leftrightarrow \mathrm{Li}_x\mathrm{TiS_2}$, which involved lithium intercalation and de-intercalation during the discharge and charge processes, respectively. The Li/TiS_2 battery had a cell voltage of 2.5 V and delivered an energy density of 480 W h kg^{-1}. Exxon attempted unsuccessfully to commercialize the Li/MoS_2 (Moli Energy) battery[1,12,13] due to the uncontrollable lithium dendrite growth which caused short circuits and fire hazards. Similarly, the development of Li/V_2O_5,[14] Li/V_3O_8 (cell operating at 80–120 °C and based on a polymer electrolyte),[15,16] and Li/MnO_2[16,17] encountered the lithium dendrite problem as well. The recall of the Molicel® in 1989 declared the death penalty of LMBs.[1,8,18]

The safety concerns of LMBs prompted researchers to search for safer battery systems, and the invention of LIBs fulfilled this requirement. In a LIB, the lithium anode is replaced with lithium ion intercalation carbonaceous materials. The technology was based on the early studies of graphite intercalation compounds (Li_xC_6) by chemical and electrochemical procedures.[19–27] In 1981, Goodenough first proposed to use layered $LiCoO_2$ as an intercalation cathode material.[28] Yoshino constructed a LIB using a carbonaceous material synthesized by heat-treatment of petroleum coke as the anode material and Goodenough's $LiCoO_2$ as the cathode material, both of which are intercalation type electrode materials, and $LiClO_4$ dissolved in propylene carbonate as electrolyte.[1,29,30] During the operation of a LIB, Li^+ shuttles back and forth between the anode and cathode; it is thus called a "rocking-chair" battery. Yoshino demonstrated that his LIB was much safer than the LMB; as in an abuse test, the LMB caught fire, yet the LIB did not. The developments eventually led to the commercialization of LIBs in 1991, which unveiled a booming industry of electrochemical energy storage. LIBs are now broadly used in portable electronics, appliances, drones, and electrical vehicles.

The safety improvement of LIBs over LMBs comes at the expense of energy density; that is, the specific capacity of lithium (3860 mA h g^{-1}) is almost ten times higher than that of carbon (374 mA h g^{-1}).[1] As such, for demanding applications such as grid energy storage and electrical vehicles, the energy density of the current LIBs cannot meet the ever increasing demand. The energy density of LIBs using non-aqueous electrolyte has reached its limit, ~300 W h kg^{-1}; further increasing the energy density raises great safety concerns, as organic liquid electrolyte is highly flammable. Although LIBs ease the safety concerns of LMBs, the dendrite problem persists, which is considered as the culprit of most fire accidents. Indeed, numerous fire accidents have taken place since the unveiling of electrical vehicles. Obviously for vehicle electrification, safer energy storage systems than the current LIB technology are urgently required.

SSLMBs using non-flammable SSEs are considered to be safer than liquid electrolyte-based LIBs. SSEs are thought to have wider electrochemical stability windows than conventional liquid electrolyte *via* careful selection of SSE composition.[31,32] Pairing with lithium, SSLMBs are supposed to deliver higher energy density than LIBs. The breakthrough of SSLMBs started from the discovery of fast Li^+ ion conductor $Li_{10}GeP_2S_{12}$ (LGPS) by Kanno's group.[33] They showed that the ionic conductivity of LGPS reached 12 mS cm^{-1} at room temperature, which is comparable to or even higher than those of practical organic liquid electrolytes. The progress in SSEs revives our hope to use lithium metal as the anode material in a SSLMB to realize both high energy density and high safety. Based on linear elasticity theory, Monroe and Newman predicted that if the elastic modulus of the polymer electrolyte is two times greater than that of lithium, the dendrite growth can be suppressed.[34] The prediction stimulates extensive studies searching for mechanically strong SSEs to suppress dendrite growth. However, hitherto the research has not been successful. In fact, experiments show that typical SSEs such as $Li_7La_3Zr_2O_{12}$ (LLZO) and LGPS failed to suppress dendrite growth as predicted; in contrast, dendrites grow even more easily in these SSEs than in liquid electrolyte.

A prevalent explanation regarding the dendrite growth mechanisms in SSLMBs is the mechanical penetration of lithium through the SSE. As shown in Fig. 2a, similar to the dendrite growth in liquid electrolyte based LMBs, a crack or void in the surface of the SSE is the preferred lithium nucleation site due to the electric field amplification.[35] Porz *et al.* proposed that defects, particularly surface cracks, are where high electric fields exist and thus the preferred lithium deposition sites, and the crack tip has high stress concentration, which leads to crack propagation and thus lithium deposition.[36] The crack and lithium propagate from one electrode to the other, leading to the failure of the battery. This hypothesis has received a lot of experimental support. Ren *et al.* demonstrated that a symmetric lithium cell based on $Li_{6.5}La_3Zr_{1.5}Ta_{0.5}O_{12}$ (LLZTO) electrolyte exhibited a short-circuiting phenomenon after polarization at a high applied direct current with a current density of 0.5 mA cm^{-2}, and a scanning electron microscopy (SEM) image of the failed SSE

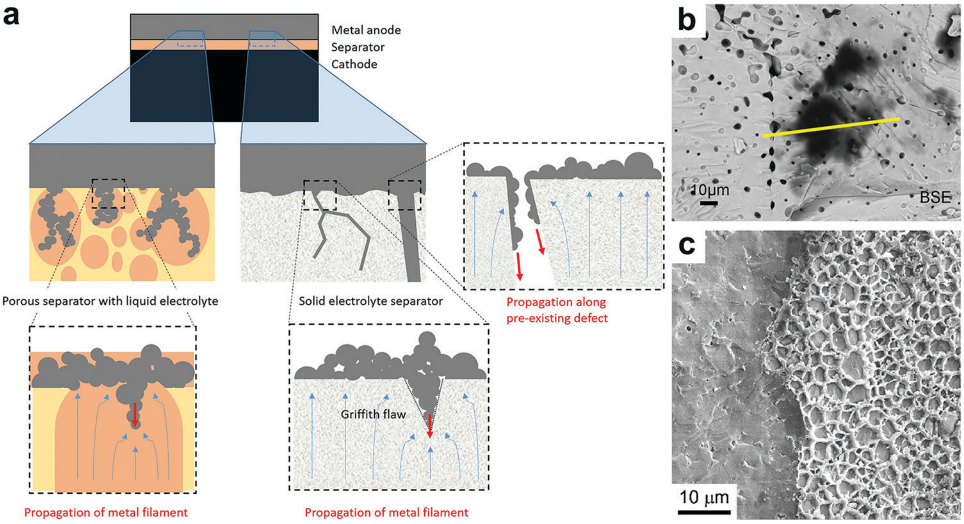

Fig. 2 Lithium dendrites in LMBs. (a) Illustration of lithium metal electrodeposition in liquid electrolytes and SSEs. Red arrows point out lithium dendrite growth towards the separator and blue arrows show electric field lines. A defect mediated failure mechanism of lithium penetration in SSEs is emphasized as opposed to classic 'dendritic' growth. (Reproduced with permission.[35] Copyright the Author(s) 2017. Published by ECS.) (b) A SEM image of the cross-section of the short-circuited LLZTO SSE pellet in backscattered electron (BSE) mode. (Reproduced with permission.[37] Copyright 2015 Elsevier B.V.) (c) SEM image of the web structure in cycled LLZO after exposure to air. Intergranular lithium filaments are observed. (Reproduced with permission.[38] Copyright 2017 Elsevier Ltd.)

showed near-spherical pores which were possible lithium propagation paths (Fig. 2b).[37] The short-circuiting period showed a positive correlation with the relative density of LLZTO electrolyte pellets. Others proposed that lithium dendrites grow through grain boundaries and interconnected pores (Fig. 2c).[38] Cheng *et al.* observed that lithium preferentially deposits along the grain boundaries (intergranularly) of the SSE.[38] They found a honeycomb structure in the crack surface of $Li_{6.25}Al_{0.25}La_3Zr_2O_{12}$, and the diameter of the honeycomb structure agrees very well with the grain size of the ceramic electrolyte.

To avoid the grain boundary effect, Swamy *et al.* investigated lithium dendrite growth in single crystal LLZO.[39] They tested a Au/LLZO/Li cell with a diameter ratio between Au and lithium of 0.5, and with some preformed indentation cracks on the surface of the LLZO under the Au electrode. They discovered that lithium deposition occurred preferentially along the perimeter of the Au electrode rather than from the preformed cracks, where the electric field was the strongest. They concluded that electric field amplification drives lithium penetration from sites on the SSE surface with supercritical surface flaws.

The mechanical penetration mechanism or the electric field enhancement theory is recently challenged by Han *et al.*, who suggested that the high electronic conductivities of LLZO and Li_2S–P_2S_5 SSEs allow Li^+ to combine with electrons to deposit lithium inside these SSEs when the potential reaches the Li-plating potential.[40] They proposed that lithium nucleated from defect sites such as voids randomly, then grew until all the lithium are connected to short the battery. This electronic conductivity-facilitated lithium growth mechanism is different from the mechanical penetration mechanism: in the former lithium nucleates randomly at defect sites with no direction preference, while in the latter lithium penetration is directional from one electrode to the other and controlled by the electric field.

The lithium dendrite problem in SSLMBs is closely related to the mechanical and electrochemical properties of lithium, which have been overlooked in the past due to the fact that lithium is not considered as a structural material, but has attracted a lot of attention lately due to its important battery applications.[41–43] There are a few review papers dealing with the electro-chemo-mechanical phenomenon in solid state batteries;[41,42,44,45] however, hitherto the electro-chemo-mechanics of lithium has not been systematically reviewed, and filling this gap is the main purpose of this review. Wang *et al.* provided a comprehensive review of the interfacial degradation/failure mechanisms, including the contact and electrochemical stability of interfaces, of solid state batteries.[44] Mechanical factors affecting interfacial contact and lithium deposition are highlighted. Their review provides important strategies to construct stable electrode/SSE interfaces, such as introducing interlayers to improve interfacial contact, 3D SSE structures, and plating stress relief to suppress lithium dendrite formation. However, the electro-chemo-mechanics of lithium is not emphasized in their review. Our review thus fills in this gap, emphasizing how the interplay of the mechanics and electrochemistry of lithium dictates the dendrite formation, propagation and interfacial stability between lithium and SSEs.

Zhang *et al.* provided a detailed review about mechanics-related material damage, in particular, cracking in active materials such as cathode materials and de-bonding of active materials with the electrolyte, which may provide important strategies for mitigating the detrimental mechanics-related material damage and alleviating the corresponding performance degradation.[45] However, the electro-chemo-mechanical coupling phenomenon, the main topic of this review, was not discussed in their paper. In fact, this is identified as one of the future research directions, which is "Further understanding on the strong coupling between the mechanics and electrochemistry of SSLMBs through both experimental measurements and theoretical modeling."

Before discussing the electro-chemo-mechanics of lithium, it is beneficial to provide a retrospect of the mechanical properties of lithium to see what we can learn from these past studies to guide current SSLMB research studies.

2. Mechanical properties of lithium

Recent studies demonstrate that the mechanical properties of lithium are closely related to its length scale. The yield strength of lithium increases significantly with decreasing length scale. The notion that "smaller is stronger" found in conventional metals such as copper[46–48] is valid in lithium as well. We therefore divide our discussion into three sections according to different length scales, *i.e.* bulk lithium with grain size above 10 μm, micrometer lithium with the length scale from about 1 to 10 μm, and nanoscale lithium whiskers with diameters less than 1 μm.

2.1. Mechanical properties of bulk lithium (grain size above 10 μm)

The low temperature mechanical properties of lithium were investigated by several groups.[49–54] The results showed that the tensile strength of lithium increases almost linearly with decreasing temperature from 250 to 4.2 K, and it is about 2.7 MPa with an elongation to failure of 27% at 80 K (Table 1).[51] Lithium transforms from a body-centered-cubic (bcc) to hexagonal structure below 72 K without cold work, and from a bcc to faulted face-centered-cubic (fcc) structure if lithium is cold worked below 110 K.[50,52,53] Below room temperature, lithium showed strain hardening, while above room temperature there was no strain hardening. The room temperature shear modulus was measured to be 3.7 GPa. Slip was the main deformation mechanism with the Burgers vector suggested to be 1/2[111] on a (−1−12) plane, and slip on (−101) and (101) with a different Burgers vector was also proposed at room temperature. The plastic behavior of lithium has been found to be similar to the behavior of sodium and hence atypical for a bcc metal.[51]

The temperature dependent elastic and visco-plastic properties of lithium were measured in tension by Tariq *et al.*,[55] and the elastic modulus at room temperature is 7.8 GPa, which is significantly larger than that measured by Schultz.[56] The yield stress at room temperature increases from 0.76 to 1.1 MPa when the strain rate increases from 2×10^{-3} to 1.05 s^{-1}, respectively. Lithium exhibits significant work hardening at high strain rates and room temperature with a very small elastic region. The authors showed that lithium creeps rapidly at higher temperatures, and lithium in the focus lens might undergo some combination of visco-plasticity and creep behavior.[55] Lepage *et al.* investigated the temperature-dependent stress–strain response of the lithium foil between 198 and 398 K at a strain rate of 3×10^{-5} s^{-1}.[57] As shown in Fig. 3a, strain hardening was observed only at the lowest temperature (198 K). For the other temperatures (≥248 K) strain hardening was not observed.[57]

The elastic and plastic mechanical properties and creep behavior of bulk lithium were characterized by Masias *et al.*[58] Elastic properties were measured using an acoustic technique

Table 1 Mechanical properties of metallic lithium

Microstructure	Young's modulus E (GPa)	Shear modulus G (GPa)	Yield stress σ_y (MPa)	Ductility	Temperature (K)	Strain rate 10^{-4} s^{-1}	Method	Deformation mechanism	Ref.
Bulk grain size >1 mm			0.6	∼50%	300	1.1	Tension		49
Single crystal		3.7	∼0.26–0.015	25% tension	100–300	4	Tension and compression	1/2[111] (−1−12)	51
Single crystal			∼0.25–0.05		100–300	2	Tension and compression	bcc to 9R (110) [1−10] shear	54
Bulk grain >300 μm			0.4	28%			Tension	Creep: GB sliding	63
Polycrystal	1.8–2.1		0.48–0.65			8.3–25	Compression		56
Bulk	7.8 at RT, 5 at 323 K, 4 at 348 K		0.41–0.76	3–8%	298–348	20–10 500	Tension	Viscoplasticity and creep	55
	7.8	2.8	0.73–0.81	50%	298	12.1	Acoustic tension	Creep: dislocation climb	58
Pillar 0.98–9.45	21.1 ⟨111⟩ 4.79 ⟨100⟩	2.4 ⟨111⟩ 8.7 ⟨100⟩	15–105			0.5	Compression pillars		64
Film 5 and 8 μm	8.2 for 8 μm film 9.8 for 5 μm film						Nanoindentation		61
Bulk grain 150 μm				25% at RT	198–398	0.3		>248 K: power-law creep <248 K: dislocation glide	57
Bulk grain 110 ± 20 μm	9.43		0.57–1.26	35%		5–5000	Nanoindentation	Creep by dislocation climb	60
Whisker 76 to 608 nm	2.7–21		12–244		RT		Compression whiskers		66

RT: room temperature; GB: grain boundary.

(pulse-echo). The Young's modulus, shear modulus, and Poisson's ratio were determined to be 7.82 GPa, 2.83 GPa, and 0.381, respectively (Table 1).[58] The measured Young's modulus agrees very well with those reported by Tariq *et al.*[55] and Robertson and Montgomery,[59] but differs from that reported by Schultz,[56] and they attributed the difference to the different grain sizes of lithium; namely, polycrystalline lithium has a lower Young's modulus value, and single crystal has a higher value. The grain size effect on the Young's modulus value is caused by the anisotropy of the elastic properties of lithium. The yield strength was determined to be between 0.73 and 0.81 MPa, which agrees very well with previous studies.[55] The authors reported that the time-dependent deformation in tension was significantly different compared to compression. In tension, power law creep was observed with a stress exponent of 6.56, suggesting that creep was controlled by dislocation climb. In compression, time-dependent deformation was characterized over a range of stresses believed to be germane to solid state LMBs (0.8–2.4 MPa). At all compressive stresses, significant barreling and a decrease in strain rate with increasing time were observed.

Through bulk tensile testing and nanoindentation of high purity commercial lithium foil, Fincher *et al.* found that bulk lithium exhibits yield strengths between 0.57 and 1.26 MPa for strain rates from 5×10^{-4} to 5×10^{-1} s^{-1} (Fig. 3b).[60] The results are consistent with those reported from Tariq *et al.*[55] Fincher *et al.* also reported that lithium metal exhibits a length-scale dependency of its hardness at small scales, which decreased from 43 to 7.5 MPa when the indentation depth increased from 250 nm to 10 μm, respectively. The elastic modulus was measured to be 9.43 GPa, which is consistent with the value of 9.8 GPa obtained from indentation on a 5 μm high purity vapor deposited lithium film by Herbert *et al.*[61] Fincher *et al.* showed further that lithium metal demonstrates significant strain rate sensitivity to deformation from nano to bulk scales with stress exponent n = 6.9 measured from nanoindentation and n = 6.55 from bulk tensile testing.[60]

Wang *et al.* studied the mechanical behavior of electroplated mossy lithium at room temperature by flat punch indentation.[62] They found that the Young's modulus of the mossy lithium with a porosity of about 62.3% is much smaller (about 2 GPa) than that (7.8 GPa) of bulk lithium (Fig. 3c). Both the mossy and bulk

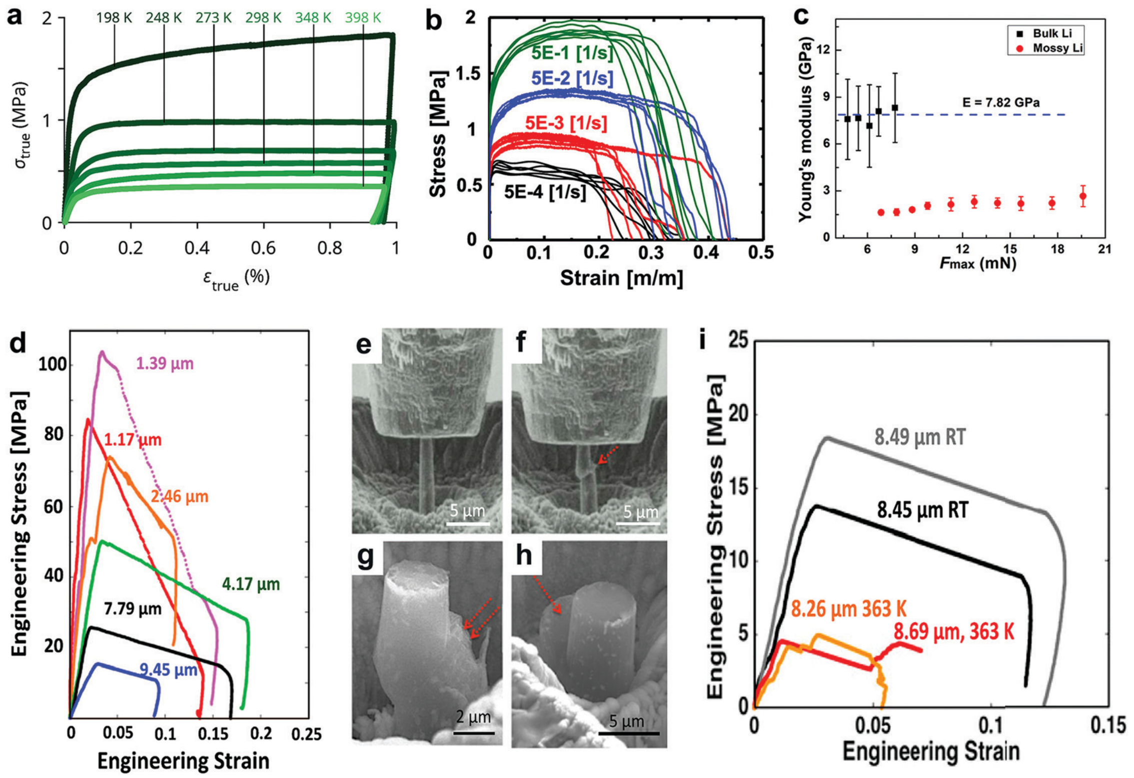

Fig. 3 Mechanical properties of lithium in macro and microscales. (a) Temperature-dependent stress–strain response of the lithium foil was measured between 198 and 398 K at a strain rate of 3×10^{-5} s^{-1}. (Reproduced with permission.[57] Copyright the Author(s) 2019. Published by ECS.) (b) Stress–strain relationship from uniaxial tension testing of the as-received bulk lithium metal, acquired at nominally constant strain rates. (Reproduced with permission.[60] Copyright 2020 Acta Materialia Inc. Published by Elsevier Ltd.) (c) Young's moduli of the mossy and bulk lithium measured with different F_{max} values. The Poisson's ratio is assumed to be 0.3. (Reproduced with permission.[62] Copyright 2019 Author(s). Published under license by AIP Publishing.) (d–h) Room temperature uniaxial compression experiments. (d) Engineering stress–strain data for lithium pillars with different diameters. (e and f) Snapshots of *in situ* compression of a representative 1 μm-diameter lithium pillar. (g and h) Compressed 4 μm-diameter lithium pillars. Arrows point to slip offsets, likely along a ⟨111⟩ direction. (Reproduced with permission.[64] Copyright 2017 National Academy of Sciences.) (i) Engineering stress *versus* engineering strain for uniaxial compression of lithium pillars with diameters of ∼8 μm at room temperature and 363 K. (Reproduced with permission.[64] Copyright 2017 National Academy of Sciences.)

lithium show clearly an indentation creep behavior. Despite its highly porous microstructure, the impression creep velocity of the mossy lithium is less than one-thirtieth of that of bulk lithium under the same stress.

In summary, the Young's modulus, shear modulus and yield strength of bulk lithium are about 7.8 GPa, 3.7 GPa, and less than 1 MPa at room temperature (Table 1).[55,58,63] At low temperatures, lithium exhibits significant strain hardening caused by dislocation activity. Phase transformation from bcc to hexagonal close-packed or faulted fcc also occurs in lithium at low temperatures. At room temperature, lithium does not show strain hardening except for deformation at high strain rates. Diffusional creep or dislocation creep is the main deformation mechanism in lithium at room temperature.

2.2. Mechanical properties of lithium pillars (diameters from 1 to 10 μm)

Xu *et al.* performed *in situ* uniaxial compression experiments on single crystalline lithium pillars with diameters from 980 nm to 9.45 μm at room temperature and 363 K in a SEM.[64] As shown in Fig. 3d–h, they observed a strong size effect in terms of the yield strength at room temperature which increased from 15 to 105 MPa as the pillar diameter decreased from 9.45 to 1.39 μm, respectively. The large size effect is explained in terms of dislocation and multiplication driven plasticity. The authors also reported a strong crystallographic orientation anisotropy of the elastic and shear moduli; namely, density functional theory calculation predicts the elastic moduli $E_{\langle 111\rangle}$ to be 21.1 GPa and $E_{\langle 100\rangle}$ to be 4.79 GPa, and the average shear moduli $G_{\langle 111\rangle}$ to be $\sim$2.4 GPa and $G_{\langle 100\rangle}$ to be $\sim$8.7 GPa. The calculated Young's modulus is consistent with a previous theoretical calculation[65] and recent acoustic measurement.[58] Similar compression experiments were conducted by Zhang *et al.*,[66] showing that the yield strength of the micron-sized lithium pillars is 39–100 MPa, which is consistent with that reported by Xu *et al.*[64] It is noted that large localized shear deformation caused by atomic plane slip was observed in both Zhang *et al.*'s[66] and Xu *et al.*'s[64] experiments, suggesting that dislocation slip is active during the compression experiments. The micron sized pillars exhibit much higher yield strength than the bulk lithium. Xu *et al.* also showed that the yield strength of lithium decreases significantly with increasing temperature, attaining 35 MPa at 90 °C for micron sized lithium, which is about one third of that obtained at room temperature (Fig. 3i).

2.3. Mechanical properties of nanoscale lithium whiskers

The strong size dependent mechanical properties of lithium pillars stimulate studies on the mechanical properties of even smaller lithium structures such as lithium dendrites or whiskers, whose size is in the nanometer regime, but their mechanical properties are not investigated due to technical difficulties in sample fabrication, handling and testing.[67] In this context, Zhang *et al.*[66] and He *et al.*[68] first grew stable lithium whiskers using a novel atomic force microscopy-environmental transmission electron microscopy (AFM-ETEM, Fig. 4a) electrochemical and mechanical device and then conducted real time mechanical property measurements for the *in situ* grown whiskers. In Zhang *et al.*'s set up, an arc-discharged CNT was attached to a conducting AFM tip by electron beam deposition of carbonaceous materials; this assembly was used as a cathode, the scratched lithium metal on the top of a sharp tungsten needle was used as an anode, and the naturally formed Li_2CO_3 on the lithium surface was used as a SSE (Fig. 4a).[66] They achieved *in situ* growth lithium whiskers with diameters ranging from 100 nm to 600 nm in a CO_2 atmosphere while simultaneously observed the stress generation of the growing lithium whisker.[66] It should be mentioned that dendrites and whiskers are sometimes used interchangeably in the literature,[67] although distinction can be drawn between the two: namely dendrites usually refer to tree-like branched structures during the electrochemical plating of metals,[67,69] and whiskers are individual hair-like protrusions that grow out of a metal surface under stress.[70–72] Whisker growth usually occurs on the surfaces of low melting temperature metals such as Sn, In, Zn, Cd, and Sb,[73,74] and whiskers have been observed to grow to several millimeters in length with diameters of a few microns to tens of microns. Sn whisker growth is an outstanding problem in microelectronics, in which the growth of Sn whiskers shorts electronic devices and causes electrical failure of the devices.[70,72] The growth mechanism of Sn whiskers has not been well understood even to date.

In Zhang *et al.*'s experiments, the mechanical properties of lithium whiskers were measured *via* two very different approaches: the first one was the measurement of the stress generation of a growing whisker (hereafter referred to as growth stress) in real time (Fig. 4b), and the second one was the measurement of the compression yield strength of a whisker after its growth (Fig. 4c). As shown in Fig. 4b, a lithium ball nucleated underneath the AFM tip without CNT (261 s) and then necked down to form a whisker (282, 310 and 365 s). The whisker growth ceased due to compression imposed by the AFM cantilever tip under an applied potential. The growth stress increased from tens of MPa to 130 MPa when the diameter of the whisker decreased from 590 nm to 120 nm (Fig. 4d). The growth stress does not represent the yield stress of the whisker, as when the whisker reached certain length, mechanical instability caused buckling or bending of the whisker. Thus the reported maximum growth stress is the lower bound of the real growth stress. Still the 130 MPa growth stress is significantly higher than the yield stress of bulk lithium, which is around 1 MPa. The yield stress increases from 12.2 MPa to 244 MPa when the diameter of the whisker decreases from 607 to 76 nm (Fig. 4e), which is much higher than the growth stress. Both the growth stress and the yield stress exhibit a strong size effect, which is similar to the size effect observed in micron sized metal pillars, which is explained in terms of dislocation starvation or dislocation nucleation mediated plasticity.[48,75,76] The size effect, *i.e.* smaller is stronger, exists in lithium across different length scales (Fig. 4f), suggesting that the mechanical behavior of lithium exhibits similar characteristics to those of other metals.[43]

The surface of the *in situ* grown lithium whisker was covered with a thin layer of Li_2CO_3 with a thickness less than 20 nm (15 nm in Fig. 5a), which played a critical role in the growth of

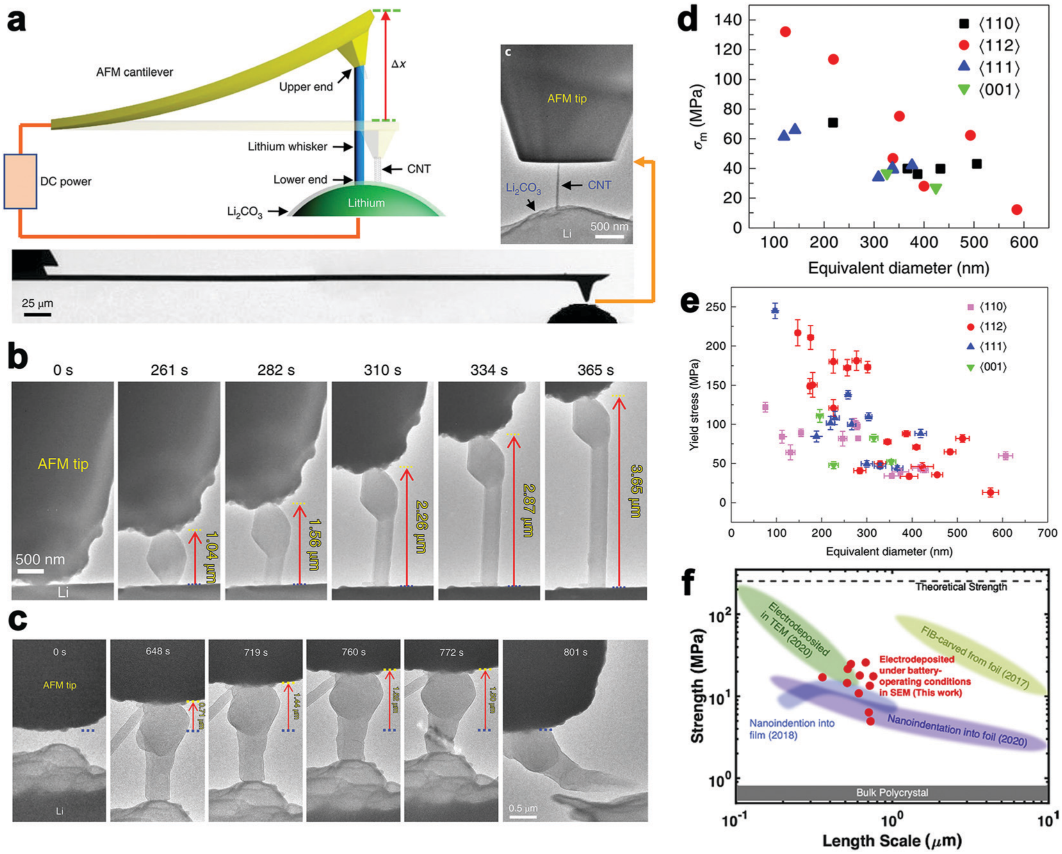

Fig. 4 Mechanical properties of lithium whiskers. (a) Schematic and TEM image of the AFM-ETEM set-up used for observation and measurement of lithium whisker growth. The measured displacement of the cantilever tip is denoted as Δx. (b) *In situ* AFM-ETEM imaging of lithium whisker growth and concurrent measurement of the maximum stress generated by lithium whiskers before their collapse. (c) *In situ* compression testing of the as-grown lithium whiskers. (d) Plot of the maximum stress σ_m *versus* equivalent diameter for growing lithium whiskers with different growth directions. (e) Yield stress *versus* equivalent diameter measured for lithium whiskers with different growth directions. The vertical and horizontal error bars show the standard deviations of yield stress and equivalent diameter, respectively. (Reproduced with permission.[66] Copyright 2020 Springer Nature.) (f) Yield stress *versus* diameter plot for lithium metal across different length scales, showing an apparent size effect; that is, smaller is stronger. (Reproduced with permission.[43] Copyright 2020 Materials Research Society.)

the lithium whisker. The Li_2CO_3 layer was formed by chemical or electrochemical reaction between lithium and CO_2. As such, when no CO_2 was flown into the transmission electron microscopy (TEM) chamber during lithium deposition, no dendrite growth was observed due to the lack of Li_2CO_3 confinement, instead a lithium plate was formed, which was unstable and crumpled soon after its formation (Fig. 5b).[66] When the CO_2 pressure was between 10^{-4} and 3 mbar, individual whiskers grew, and when the CO_2 pressure was greater than 3 mbar, bundles of whiskers or dendrites emerged like the eruption of a volcano (Fig. 5c).[66] The surface Li_2CO_3 layer played another important role in stabilizing the as-grown lithium whisker under the electron beam illumination, thus enabling *in situ* mechanical property measurements. Similar gas pressure dependent lithium morphologies were also observed by Yulaev *et al.*[77]

It should be noted that the thin surface Li_2CO_3 layer may have a significant impact on the measured yield strength of lithium whiskers, since the yield strength of Li_2CO_3 is much larger than that of lithium. To evaluate the effects of the surface Li_2CO_3 layer on the measured mechanical properties of lithium whiskers, Zhang *et al.* considered the Li/Li_2CO_3 whisker as an elasto-plastic core–shell cylinder. Based on the rule of mixtures for composites,[66] the Young's modulus $E_{\mathrm{Li/Li_2CO_3}}$ of the core–shell cylinder can be estimated as $E_{\mathrm{Li/Li_2CO_3}} = (E_{\mathrm{Li}}A_{\mathrm{Li}} + E_{\mathrm{Li_2CO_3}}A_{\mathrm{Li_2CO_3}})/(A_{\mathrm{Li}} + A_{\mathrm{Li_2CO_3}})$, where E_{Li} and $E_{\mathrm{Li_2CO_3}}$ denote the Young's moduli of the lithium core and Li_2CO_3 shell, respectively; A_{Li} and $A_{\mathrm{Li_2CO_3}}$ denote the cross-sectional areas of the lithium core and Li_2CO_3 shell, respectively. For a representative composite Li/Li_2CO_3 whisker, the diameter of the lithium core and the thickness of the Li_2CO_3 shell are taken as 260 nm and 5 nm based on Zhang *et al.*'s work, respectively; the typical values of the Young's modulus and Poisson's ratio of the lithium core are taken as E_{Li} = 6 GPa, ν_{Li} = 0.3, respectively; and those of the Li_2CO_3 shell as $E_{\mathrm{Li_2CO_3}}$ = 21.5 GPa, $\nu_{\mathrm{Li_2CO_3}}$ = 0.3, respectively. From the above rule-of-mixture formula, the predicted Young's modulus of the composite whisker is 7.28 GPa, which is about 20% more than that of pure lithium whiskers without surface Li_2CO_3. Although the yield strength measurements were influenced by the surface Li_2CO_3 layer, we believe that the influence of Li_2CO_3 on the *in situ* measured growth stress of the lithium whisker is negligible, as the surface

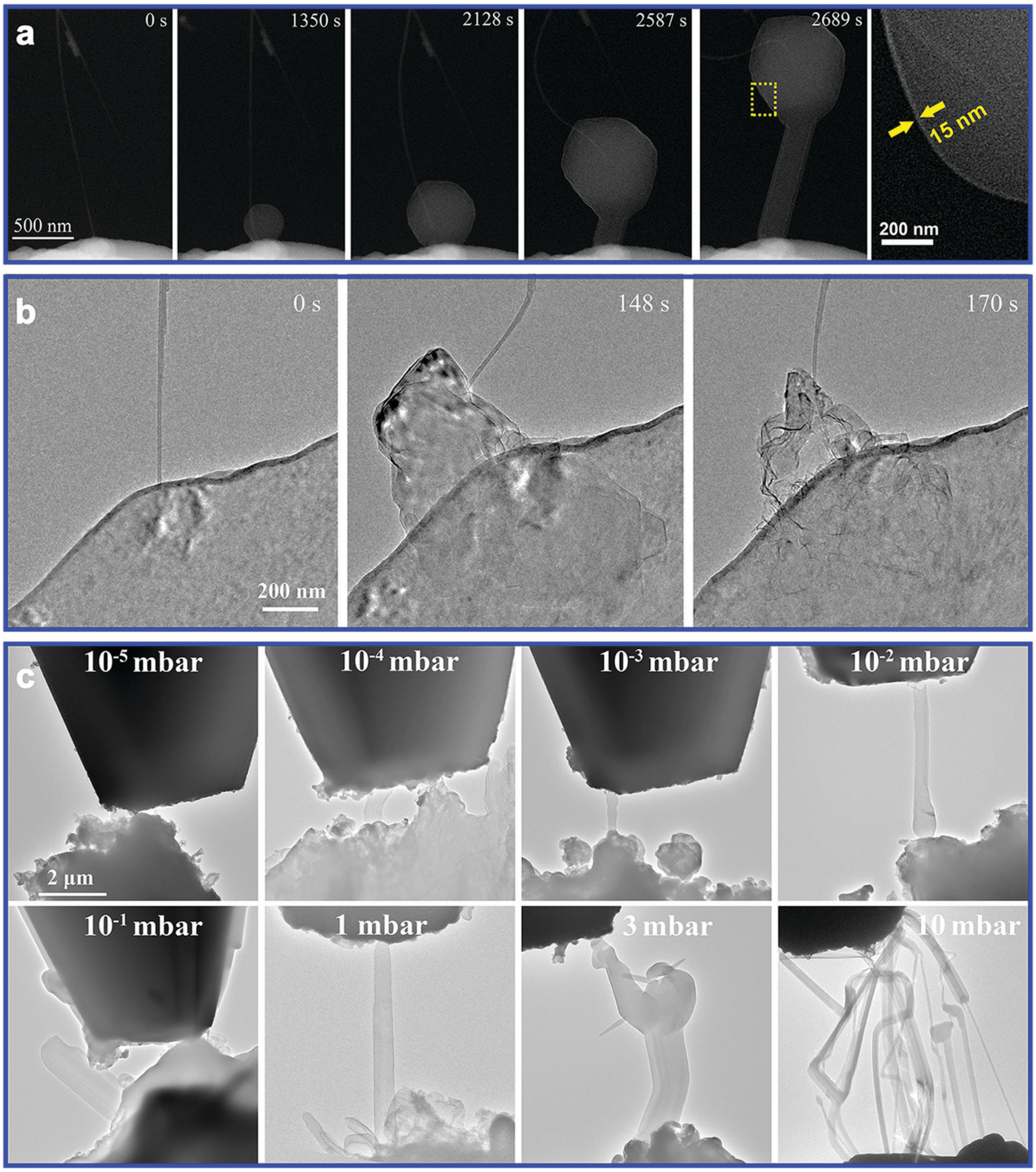

Fig. 5 Effect of the CO_2 gas pressure on the growth of lithium whiskers in an AFM-ETEM experiment. (a) Time-lapse TEM images of the as-growing lithium whisker with a Li_2CO_3 surface layer in scanning transmission electron microscopy-annular dark field (STEM-ADF) mode. (b) Lithium deposition under no-gas conditions. (c) *In situ* observations of growth of lithium whiskers at different CO_2 pressures. TEM images showing no lithium whisker growth at 10^{-5} mbar; growth of individual lithium whiskers from 10^{-4} to 3 mbar; and bursting of numerous dendrites at 10 mbar of CO_2 pressure. (Reproduced with permission.[66] Copyright 2020 Springer Nature.)

Li_2CO_3 layer is extremely thin in a growing lithium whisker. Therefore the yield strength of the lithium whisker is at least 130 MPa.

Citrin *et al.* investigated the mechanical properties of lithium pillars with diameters from 360 to 759 nm grown in a commercial $LiCoO_2$/lithium phosphorus oxynitride (LiPON)/Cu solid-state thin-film cell *in situ* in a SEM equipped with nanomechanical capabilities. They reported an average Young's modulus to be 6.76 ± 2.88 GPa, with an average yield stress of 16.0 ± 6.82 MPa.[43] Their reported yield stress value for the submicron sized lithium pillar is much smaller than that reported by Zhang *et al.*,[66] and the reason for this discrepancy is unclear.

For lithium, room temperature (300 K) corresponds to a homologous temperature of $0.66T_m$ ($T_m = 180.5$ °C = 453.5 K is the melting temperature of lithium[78]), meaning that creep is the main deformation mechanism for lithium. We summarize recent results on the creep properties of lithium in the following.

2.4. Creep of lithium

Creep can be characterized by measuring the strain as a function of time in constant force or constant-displacement-rate experiments.[58,78] There are two mechanisms of creep: dislocation creep, which exhibits power-law behaviors; and diffusional creep which shows linear-viscous characteristic. The rate of both is usually limited by diffusion, so both follow Arrhenius's law,[78] understanding of which mechanism is in operation can generally refer to the deformation mechanism map,[58,78] which shows the range of stress and temperature dependent deformation mechanisms. The creep mechanism is expressed by eqn (1):[58]

$$\dot{\varepsilon} = A\sigma^n d^{-p}\exp(-Q_c/RT) \tag{1}$$

where $\dot{\varepsilon}$ is the steady-state strain rate, A is a constant, σ is the stress, n is the stress exponent, d is the grain size, p is the grain size exponent, Q_c is the activation energy for creep, T is the absolute temperature and R is the gas constant (8.31 J mol^{-1} K^{-1}). For creep above $T/T_m > 0.5$ the stress exponent n is typically in the range of 1–7.[58,78] Different n values suggest different creep mechanisms: n values of $\sim$1 – diffusion; n values between 3 and 7 – a dislocation mechanism; $n \cong 3$ – dislocation glide; and $n \cong 5$–7 – dislocation climb.[58,78] For $n = 1$, p can be either 2 for creep controlled by lattice diffusion or 3 for creep controlled by grain boundary diffusion. Masias *et al.* conducted tensile creep experiments at 0.4 MPa at room temperature for lithium, and they reported a stress exponent of 6.56,[58] which agrees excellently with the value of 6.4 for lithium at room temperature tested in compression by Sargent and Ashby.[78] This value suggests that the creep of lithium is controlled by dislocation climb, which is mediated by atom diffusion.[58,78] The creep of Na and K was reported to follow a similar mechanism to lithium.[78]

Lepage *et al.* performed systematic studies on the creep behavior of lithium.[57] From strain-rate temperature dependent tensile experiments, they observed strain hardening at high strain rates ($>2 \times 10^{-2}$ s^{-1}) and low temperatures ($<$198 K), while at strain rates lower than 3×10^{-3} and temperatures above 248 K no strain hardening was observed. They suggested that under normal battery operating conditions, the deposited lithium in LMBs might experience significant creep deformation, and they provided a deformation mechanism map based on the lithium deposition height and current density. For example, at a pressure of 1.2 MPa and at a strain rate of 2×10^{-3} s^{-1}, the minimum height for power-law creep is h = 0.55 μm.

Creep is particularly important in governing the lithium deposition morphologies in SSLMBs, which depends on the stress condition, current density, temperature, grain size, *etc.* Understanding the creep properties of lithium under battery operational conditions can have a profound impact in controlling the lithium morphologies and thus the performance of SSLMBs.

3. Dendrites in SSLMBs

After understanding the mechanics of lithium, a natural question is then: how can the lithium mechanics be translated to the understanding of the lithium dendrite problem in SSLMBs? A major promise of SSLMBs is perhaps their potential to solve the dendrite problem in liquid electrolyte based LMBs. Based on the Monroe and Newman model,[34] when the shear modulus of SSE is over two times that of lithium, dendrite growth is suppressed by the SSE. However, it is now clear that dendrites still grow even though the Monroe and Newman criterion is satisfied. The reason for this discrepancy may be two fold. Firstly, the Monroe and Newman model is based on linear elasticity theory; however, lithium experiences large plastic deformation during propagation.[60,64,66] Secondly, Monroe and Newman assume the electrolyte to be perfect, but real electrolytes such as SSEs have a large number of defects such as voids and cracks. We conducted a survey of the literature to glean a mechanistic understanding of the origin of dendrite growth and propagation in SSEs mainly from an electro-chemo-mechanical perspective.

3.1. Dendrites in inorganic SSEs

One example of the impact of lithium mechanics on SSLMBs is the lithium deposition induced crack propagation and lithium infiltration into hard ceramic electrolyte. Porz *et al.* suggested that during the charging of LMBs lithium preferentially deposits in the surface cracks, which causes stress concentration at the crack tip, leading to crack propagation and the initiation of new cracks until they go through the entire SSE and short the SSLMB.[36] The stress buildup can easily reach the GPa level in these cracks, depending on the amount of overpotential applied.[36,66,79] Based on the studies of lithium mechanics, Lepage *et al.*[57] proposed to incorporate plasticity, creep and viscous flow into the crack propagation model (Fig. 6a and b) proposed by Porz *et al.*[36] The same is true for dendrite growth in liquid electrolyte, in which the impacts of plasticity and creep on the lithium dendrite growth and propagation have not been considered. For example, without external pressure, mossy dendritic lithium grows out of the anode during charge, and most of the mossy lithium loses electrical or mechanical contact with the anode, rendering it "dead" lithium upon discharge.[57,67,80] "Dead" lithium contributes to the low coulombic efficiency and degradation of the battery. By contrast, when under stack pressure in a coin cell, patches or flat films of lithium are plated on the anode during charge. The mechanical stress has a profound impact on the morphology of the lithium deposited.

3.1.1. Nucleation and propagation of lithium dendrites in SSEs.

Pre-existing voids and cracks provide initial spaces for lithium nucleation and infiltration. The initial lithium deposition preferentially occurs at the triple point where lithium metal, SSE, and voids/cracks meet due to the current focusing effect, and then the lithium grows unhindered along these defects.[81] The lithium infiltration induces high stress and further expands the voids and the cracks. Finally, the elongated lithium filament continuously infiltrates the propagated voids/cracks until the short circuit of the battery occurs. The lithium deposition induced expansion of the pre-existing voids and cracks during the discharge/charge cycling was observed by Seitzman *et al. via* synchrotron-based X-ray tomography in a Li_3PS_4 (LPS) SSE based SSLMB at a low current density of 100 μA cm^{-2}.[82] They visualized the expansion of a crack from a width of 11.7 to 26.0 μm after 3 discharge/charge cycles. A similar mechanical crack-opening mechanism for lithium filament propagation was also observed in LLZO based SSLMBs *via operando* optical and SEM imaging.[83]

A good example of lithium propagation along defects is demonstrated recently by Westover *et al.*, who designed a thin film battery with a $LiCoO_2$ cathode, a LiPON electrolyte, and a top layer with a copper current collector and an artificial LiPON–LiPON interface parallel to the cathode.[84] Upon electrochemical cycling, lithium metal rapidly deposited at the edge of the Cu current collector and then propagated along the 2D LiPON–LiPON interface (Fig. 6c). Their results prove unambiguously that LiPON can suppress dendrite penetration, even though its shear modulus (31 GPa)[85,86] is much smaller than that of LLZO (>60 GPa),[87–89] with dendrites penetrating LLZO easily but not LiPON. They attributed the dendrite suppression by LiPON to its homogeneous and pore-free morphology, while pores and cracks are always present in the LLZO. This result underscores the importance of structural uniformity and defect engineering in suppressing lithium dendrite growth.

A grain boundary is another site for lithium filament propagation in inorganic SSEs due to its lower elastic modulus (a "soft" region) than the bulk region.[38,90] The variations of microstructure and composition in the vicinity of the grain boundary cause a decrease of modulus in this region. Molecular dynamics calculation predicts that the shear modulus of the grain boundary is $\sim$50% as high as that of the bulk region.[90] The clear presence of lithium filaments in the grain boundaries was observed in both polycrystalline LLZO[38] and polycrystalline LPS.[36] However, whether or not filaments entered at grain boundaries could not be determined. It is possible that grain boundaries could serve as preferential sites for nucleation and pathways for propagation.

Lithium mechanics can also impact surface coating layers which are broadly used to protect the lithium anode. Creep of lithium can produce cracks in the coating, which results in the dysfunction of the surface coating. Lithium deposition induced cracks and fracture in the Cu film current collector were indeed observed by SEM.[43,91–93] When studying the effect of current density on electrochemical lithium deposition/dissolution at the LiPON/Cu interfaces in a Li/LiPON/$Li_{1.3}Al_{0.3}Ti_{1.7}(PO_4)_3$ (LATP)/LiPON/Cu cell, it was found that the lithium nucleation rate and the saturation density of lithium nuclei increased with increasing current density. When the current density was smaller than 300 μA cm^{-2}, lithium islands continued to separately grow under a Cu film to the critical sizes to produce small cracks in the Cu film, resulting in isolated lithium rod growth from the cracks. As shown in the top view of the Cu coated LiPON surface, the pressure reached 400 MPa at the nucleation stage in the deposited lithium, thus causing fracture of the Cu film current collector (with a thickness from 30 to 90 nm) and the growth of lithium whiskers from the crack (Fig. 6d). The deposited lithium between the Cu film current collector and the LLZO SSE can even penetrate the Cu film and form whisker-like lithium.[93] These observations provide unambiguous evidence that lithium deposition can generate very high stress. The formation of blisters and cracks was apparently attributed to the non-uniform lithium deposition underneath the Cu film originating from the large lithium nucleation barrier on the Cu film, highlighting the importance of reducing the lithium nucleation energy to minimize the lithium deposition induced stress.

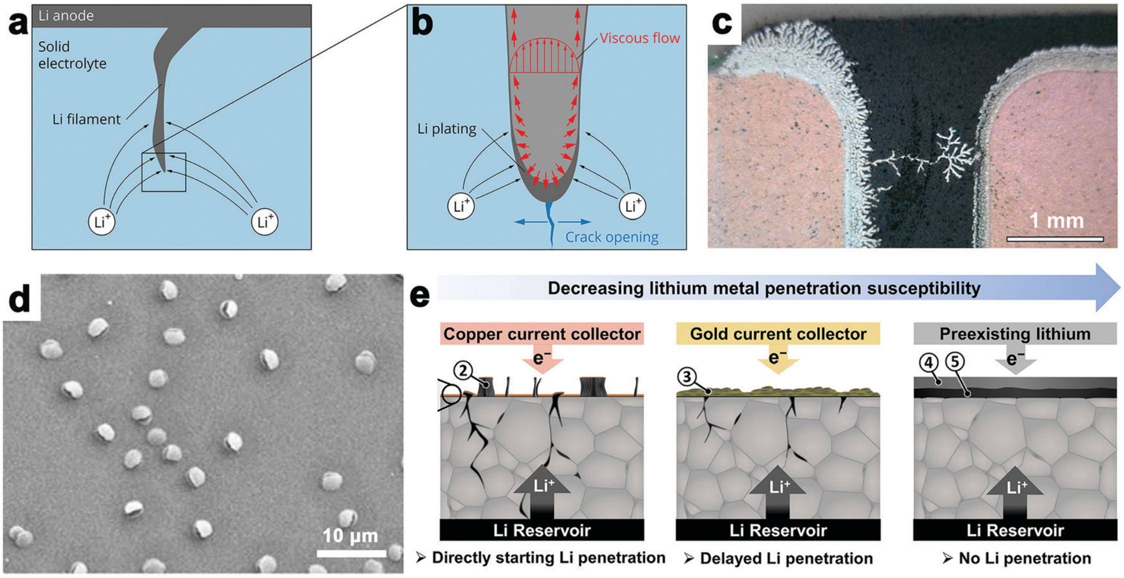

Fig. 6 Lithium deposition and propagation in inorganic SSEs. (a) Schematic of a lithium filament in a SSE matrix. In ceramic SSEs, lithium can penetrate surface flaws, forming a filament. (b) Stress accumulates at the tip of the lithium filament as a function of current density, while there is viscous flow with a boundary layer away from the tip. (Reproduced with permission.[57] Copyright the Author(s) 2019. Published by ECS.) (c) Optical micrographs of the Cu current collectors and tree-like lithium dendrites. (Reproduced with permission.[84] Copyright 2019 American Chemical Society.) (d) A top-view SEM image showing the blister formation and cracking in the Cu film coated on a LiPON surface due to lithium deposition induced stress. (Reproduced with permission.[92] Copyright 2015 The Electrochemical Society.) (e) Schematic showing the plating behavior at an apparent (geometrical) current density of 100 μA cm^{-2} using a copper current collector (left) and a gold current collector (middle), and plating below a pre-existing dense lithium layer (right). (Reproduced with permission.[93] Copyright 2019 Elsevier Inc.)

The lithium deposition induced fracture of the Cu film should be ascribed to the non-uniform lithium deposition and the lithium deposition induced internal stress. As shown in Fig. 6e,[93] during plating using a lithiophobic copper thin-film electrode, the lithium nucleation energy is high, leading to whisker- and dendrite-like deposition. While during plating using a lithiophilic gold current collector, Li_2Au alloy forms, leading to more uniform lithium deposition, and lithium penetration was delayed. Plating on the pre-existing lithium does not show any indication for lithium penetration, and stable plating can be achieved due to the low nucleation energy. Yan *et al.* explored the nucleation pattern of lithium on various metal substrates and unravelled a substrate-dependent growth phenomenon that enables selective deposition of lithium metal.[94] With the aid of binary phase diagrams, they found that no or small nucleation barriers are present for metals exhibiting a definite solubility in lithium, whereas appreciable nucleation barriers exist for metals with negligible solubility. Low nucleation barriers facilitate uniform lithium deposition, while high nucleation barriers should be responsible for non-uniform lithium deposition and dendritic lithium growth.

The fracture of the Cu film current collector indicates that large mechanical stress much higher than the yield strength of bulk lithium is produced during lithium deposition, suggesting that pure mechanical property studies on lithium may not be translated directly to the lithium mechanics in SSLMBs. As in all previous mechanical property characterization, particularly the creep experiments, the applied load was usually very low less than a MPa. The yield strength of the bulk lithium is less than 1 MPa. However, the stress generation during lithium deposition can be a few orders of magnitude higher than the stress applied in the mechanical test of bulk lithium. Furthermore, the lithium deposition is not a pure mechanical process, it is an electrochemical and mechanical coupling process. The study of the mechanical behavior of lithium in SSLMBs needs to be investigated from an electro-chemo-mechanical perspective.[41,42,44] More importantly, the lithium stripping/deposition takes place in a confined volume, usually with nanometer feature size and under the so-called stack pressure, and the lithium surface is usually covered with a solid electrolyte interphase (SEI) layer, all of which may alter the lithium mechanics significantly.

In summary, voids, cracks and grain boundaries are the preferred lithium nucleation sites due to electrical focusing effects on these sites. High lithium nucleation barriers lead to inhomogeneous nucleation and large mechanical stress in the medium. The lithium deposition induced stress can break the Cu film current collector, leading to dendrite nucleation and propagation. Controlling the defects and uniformity of the SSE and appropriate design of the current collector to reduce the lithium nucleation barriers are essential in optimizing the lithium deposition morphologies.

3.1.2. Overpotential driven lithium deposition induced stress. The stress (σ) generation due to lithium deposition in a surface crack in a SSE under an overpotential $\Delta\phi$ can be calculated using the following equation:[36]

$$\sigma V_m = F\Delta\phi \qquad (2)$$

where F is Faraday's constant ($F = 9.65 \times 10^4$ C mol^{-1}) and V_m is the molar volume of lithium metal ($V_m = 13$ cm^3 mol^{-1}). Eqn (2) relates the electrochemical work (right side of the equation) to the mechanical work (left side of the equation), thus forming the basis for predicting mechanical failure. For example, an overpotential of $\Delta\phi$ = 100 mV corresponds to a mechanical stress σ = 750 MPa, which can easily cause cracks and their propagation in a SSE (Fig. 6a and b).[36,49,79,95,96]

The large stress generated by the overpotential-driven lithium deposition causes lithium metal to creep. At room temperature, the homologous temperature for lithium is $T/T_m = 0.66$, so lithium should exhibit a large creep strain rate $\varepsilon(T,\sigma)$ (where σ is the deviatoric shear stress) by dislocation power-law creep or diffusional creep mechanisms, according to the deformation mechanism map of metals.[78,79] Creep imparts an effective viscosity $\eta \equiv \sigma/\varepsilon(T,\sigma)$, so lithium may behave like an "incompressible fluid", transferring large mechanical stress generated by the overpotential (according to (eqn (2)) to media such as SSE, similar to the fluid in a hydraulic system. Consequently, flaws such as pores and microcracks are detrimental, as lithium can easily infiltrate into these free spaces. A more quantitative estimation of how the critical fracture stress of SSE is related to the flaw size is discussed in the following.

The fracture stress σ_f of a ceramic SSE can be calculated using the following equation:[66,97–99]

$$\sigma_f = K_{IC}(\pi a_c)^{-1/2} \qquad (3)$$

where K_{IC} is the fracture toughness of the SSE, and a_c is the critical flaw size such as the pore or grain size. As an example, let's consider the LLZO SSE reported by Ren *et al.*[37] From Fig. 2b, the typical pore size is about 5 μm, and the fracture toughness K_{IC} of LLZO is about 1 MPa.[99] Plugging these values into eqn (3) yields $\sigma_f \cong 250$ MPa. According eqn (2), an overpotential of only 33 mV produces such a critical stress to cause fracture of the SSE. From eqn (3) and Fig. 7a, it is seen that as the flaw size decreases, the critical fracture stress increases dramatically, suggesting that reducing the flaw size such as the pore size of the SSE can suppress the crack propagation and thus dendrite penetration.

Sulfide SSEs such as $Li_2S–P_2S_5$, LGPS, and LPS have been widely reported to have a high room temperature ion conductivity ($>10^{-4}$ S cm^{-1}) and are considered as the most potential SSE candidates for a new class of LMBs.[33,100,101] However, short circuits of sulfide based LMBs has frequently been reported,[32,102–105] which possibly originates from their weaker mechanical properties than oxide-based SSEs such as garnet LLZO and perovskite $Li_{0.33}La_{0.57}TiO_3$ (LLTO).[87,106,107] Kim *et al.* showed that lithium can more easily penetrate pelletized argyrodite Li_6PS_5Cl (LPS-Cl) SSEs at high stacking pressures than at low stacking pressures.[104] The fracture toughness of LPS-Cl is 0.23 MPa m$^{1/2}$,[108] and according to eqn (3), the fracture stress σ_f = 130 MPa for a flaw size of 1 μm, and 58 MPa for a flaw size of 5 μm.

More recent experiments indicate that the stress generated by lithium deposition can easily reach a few hundred MPa. The high stress can be relieved through Coble creep along interfaces. Using *in situ* TEM, Chen *et al.* investigated the deposition and stripping of metallic lithium or sodium held within a large number of parallel hollow tubules made of an ionic–electronic conductor (MIEC).[79] They showed that these alkali metals, as single crystals, can grow out of and retract inside the tubules *via* mainly diffusional Coble creep along the MIEC/metal phase boundary (Fig. 7b). Lithium was seen to surpass obstacles such as closed cap bamboo compartments inside the hollow tubules, indicating that the lithium morphology change was not displacive/convective, but diffusive. Their observations provide direct evidence that dislocation power-law creep is not the dominant creep mechanism. They showed that the diffusion coefficient of the interface between lithium and the MIEC and the surface of lithium $D_{\text{Li}}^{\text{interface}} \cong D_{\text{Li}}^{\text{surface}} \cong 2 \times 10^{-7}\ \text{cm}^2\ \text{s}^{-1}$ is about an order of magnitude higher than the bulk diffusivity $D_{\text{Li}}^{\text{bulk}} \cong 10^{-8}\ \text{cm}^2\ \text{s}^{-1}$.

In brief, the overpotential driven lithium deposition can generate a few hundred to GPa level stress in media such as SSEs. Under such large stress, lithium behaves as an "incompressible fluid", transferring large stress into media such as SSEs, causing fracture of the SSEs and failure of SSLMBs.

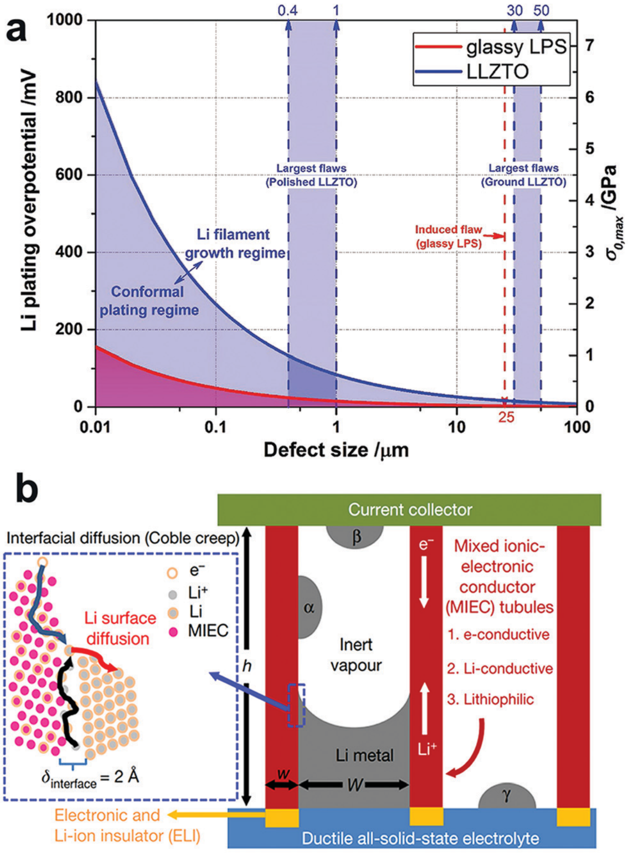

Fig. 7 (a) Inverse square root dependence of the lithium plating overpotential and crack-extension stress ($\sigma_{0,\text{max}}$) on defect size in the glassy sulfide and LLZTO SSEs. Vertical lines correspond to the large-flaw population of the indicated experimental samples. (Reproduced with permission.[36] Copyright 2017 Wiley-VCH Verlag GmbH & Co. KGaA, Weinheim.) (b) Schematic process of creep-enabled lithium deposition/stripping in a MIEC tubular matrix, where Coble creep dominates *via* interfacial diffusion along the MIEC/Li_{bcc} incoherent interface. (Reproduced with permission.[79] Copyright 2020 Springer Nature.)

3.2. Dendrites in polyethylene oxide (PEO)

In contrast to inorganic SSEs such as LLZO, which generally have high Young's moduli from tens to a few hundred GPa,[87] the Young's moduli and tensile strengths of PEO polymer SSEs, which are widely used in polymer SSLMBs, are usually less than 100 MPa and 1 MPa, respectively;[109–114] however, a PEO SSE can sustain a large plastic elongation of up to 500%, indicating its large deformability (Fig. 8a–d).[109] This phenomenon is mainly attributed to the disentanglement of polymer chains during tensile deformation that, consequently, reduces the degree of tortuosity in the path of ion transport. As such, the ionic conductivity of PEO increases with strain. It is known that lithium deposition induced stress can easily reach a few hundred to GPa level; therefore, dendrite penetration through PEO electrolyte is expected given the low Young's modulus of PEO. More studies were devoted towards improving the mechanical strength of PEO electrolytes *via* strategies such as using inorganic fillers, composite polymers, and multilayered structures. As shown in Table 2, the mechanical properties of these engineered PEO-derived electrolytes were generally improved as compared to pure PEO electrolytes.[109,110,115–118]

Theoretical studies have been performed to understand the mechanisms of dendrite penetration through PEO electrolyte. As shown in Fig. 8e, Barai and coworkers analyzed the propensity of growth of dendritic protrusion by constructing an appropriate computational procedure,[119] and they demonstrated that increasing the elastic modulus of PEO leads to the prevention of dendritic protrusions through the reduction of the exchange current density and the dendritic protrusion height. The resulting enhancement of yield strength can stabilize the dendritic protrusions, even with a shear modulus of the PEO two orders of magnitude smaller than that of lithium (Fig. 8f).[119] Monroe and Newman modeled a parallel-electrode lithium/polymer cell in a galvanostatic charging state; they revealed that the dendrite growth can be significantly slowed down by lowering the current density, and by limiting the interelectrode distance in a certain range, the cell failure can be postponed, but this advantage decreases as the distance increases.[120]

Experimental observations of the dendrite growth induced short circuit in PEO are challenging due to the buried interface.[121,122] There are a few reports about *in situ* observations of dendrites in PEO by home-made optical microscopy. Rosso *et al.* and Brissot *et al.* performed *in situ* optical microscopy observations of the dendritic lithium deposition in PEO in a symmetrical Li/PEO/Li cell (Fig. 8g).[111,123] Their experimental set-up allowed them to measure simultaneously the variation of the cell potential, the evolution of the dendrites, and the variation of the ionic concentration in the electrolyte around the dendrites. They demonstrated that the current density played a significantly role in the dendrite growth due to the existence of local current inhomogeneities.[111,123] In another study, Liu *et al.* studied the dendrite suppression effect of ionic liquid (*N*-methyl-*N*-propylpiperidinium bis(trifluoromethanesulfonyl)imide) additive in a PEO/LiTFSI electrolyte system using a digital optical microscope (Keyence VHX-100).[124] They found that the addition of ionic liquid could increase the onset time of dendrite growth and simultaneously reduce the interfacial resistance; they attributed

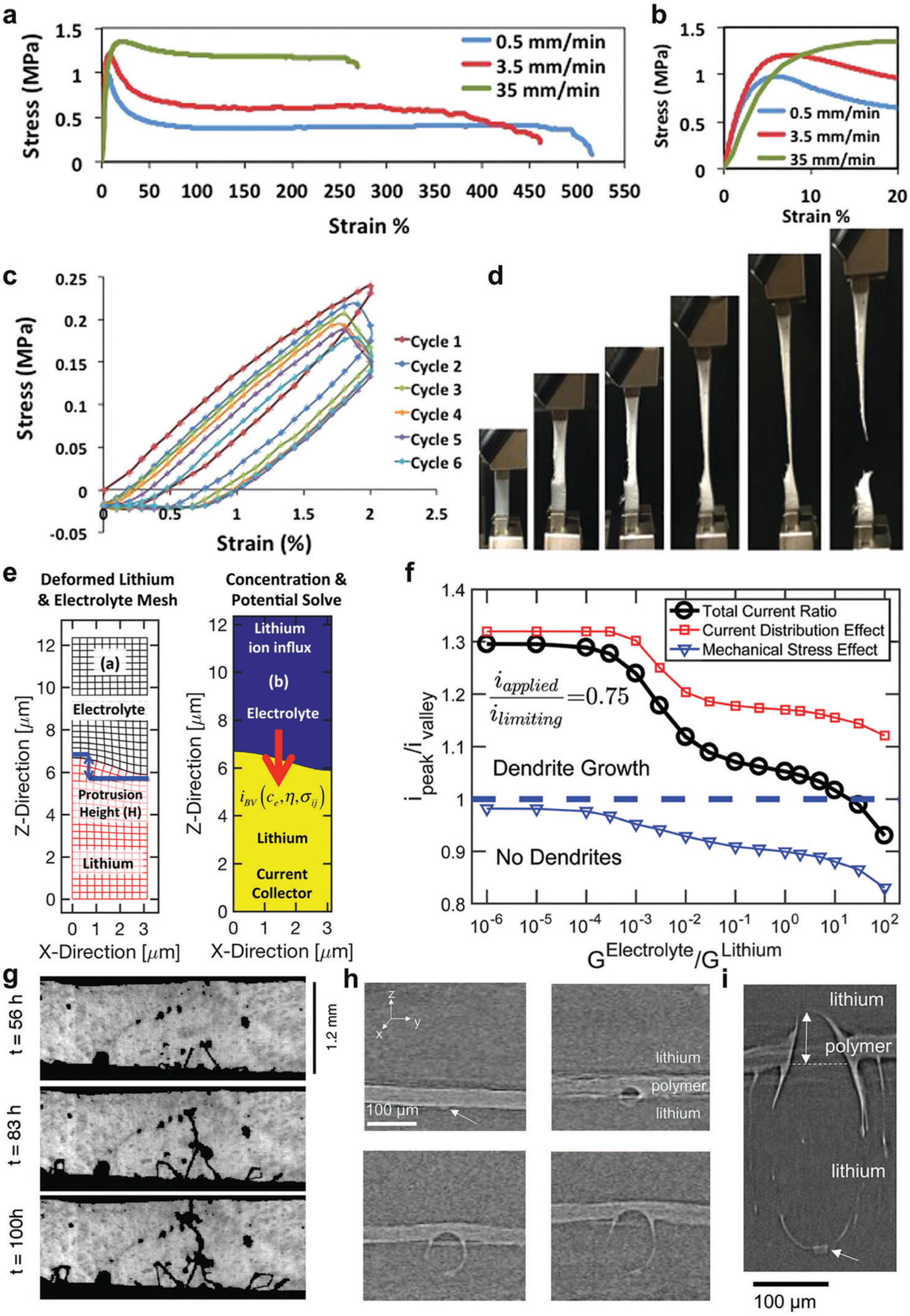

Fig. 8 Lithium dendrites in PEO SSEs. (a–d) Tensile stress–strain behavior of a solid PEO electrolyte film: (a) at three different strain rates of 0.5, 3.5 and 35 mm min^{-1}, exhibiting up to 450% elongation, (b) magnified curves below 20% strain, (c) stress–strain hysteresis effect and (d) photo images of a PEO sample subjected to tensile deformation. (Reproduced with permission.[109] Copyright 2016, Springer Nature.) (e) Schematic diagram of the computational domains used for solving the mechanics, concentration and potential problems. (Left) Lithium and electrolyte meshes used to determine the stress evolution around the dendritic protrusion. (Right) Computational domains on which the concentration and potential distributions were calculated. (Reproduced with permission.[119] Copyright the Owner Societies 2017.) (f) Ratio of the current at the peak to that at the valley plotted with respect to the shear modulus of the electrolyte phase (black circles). (Reproduced with permission.[119] Copyright the Owner Societies 2017.) (g) Dendritic growth in PEO electrolyte. The inter-electrode distance is 1.2 mm. (Reproduced with permission.[111,123] Copyright 2006 Elsevier Ltd. Copyright 1999 Elsevier Science S.A.) (h) X-ray tomograms of the *yz* plane in a symmetric Li/PS–PEO/Li cell with the polystyrene-*block*-PEO copolymer SSE showing the growth of a lithium globule. The dark gray phase is lithium metal and the light gray phase is the polymer electrolyte. The small, light gray spot at the base of the globule is an impurity particle that was initially present in the lithium foil. (Reproduced with permission.[125] Copyright the Author(s) 2016. Published by ECS.) (i) An X-ray tomogram showing a globule puncturing a polystyrene-*block*-poly(ethylene oxide) (SEO) electrolyte membrane. The dark gray phase is lithium metal and the light gray phase is the polymer electrolyte. (Reproduced with permission.[125] Copyright the Author(s) 2016. Published by ECS.)

Table 2 Mechanical properties of PEO based SSEs

Components	Young's modulus E	Shear modulus G (GPa)	Tensile strength σ_{ts} (MPa)	Elongation %	Strain rate	Ref.
PEO/$LiClO_4$			0.99	509	0.5 mm min^{-1}	109
			1.02	457	3.5 mm min^{-1}	
			1.54	278	35 mm min^{-1}	
PEO/PDMS/$LiClO_4$	1.0 MPa					263
PEO/ANF/$LiPF_6$	5.0 ± 0.05 GPa	1.8 ± 0.06	170 ± 5			110
PEO/SiO_2/LiTFSI	~0.43 GPa				0.2% s^{-1}	115
PEO/PVDF–HFP/$LiPF_6$	44.3 ± 10.6 MPa		15.0 ± 1.5	~479 ± 136%		116
PEO/sisal whiskers/LiTFSI	72 MPa					117
PEO/PEO-*b*-PE/$LiClO_4$	114.21 MPa		7.29 MPa	1142.53%		118
PEO/$LiClO_4$	~5.1 MPa		~0.32 MPa	~417%		

PDMS: polydimethylsiloxane; ANF: aramid nanofibers; PEO-*b*-PE: poly(ethylene oxide)-*block*-polyethylene.

the suppression of the lithium dendrite formation to the low interlayer resistance between lithium and the composite polymer electrolyte (CPE).

Rosso *et al.* and Brissot *et al.* directly observed dendrite growth from the lithium electrode, which then propagated towards the counter electrode until penetration, by optical microscopy.[111,123] They found that the onset of dendritic growth was hardly visible on the potential evolution. The evolution of the potential with time was only slightly affected by the growth of the dendrite; in fact, the short-circuit was only clearly visible when the dendrite had reached the counter electrode. Then a marked decrease in the potential was observed in the cyclic voltammetry (CV) curve,[111,123] followed by an erratic evolution and a clear short-circuit. The nucleation and growth of a lithium globule in a symmetric Li/PS–PEO/Li cell with the polystyrene-*block*-PEO copolymer SSE were observed by Harry *et al. via* an X-ray tomography technique (Fig. 8h), and the lithium globule penetrated the polymer SSE (Fig. 8i).[125]

To mitigate dendrite growth in PEO electrolyte, Tung *et al.* synthesized a membrane comprised of Kevlar-derived aramid nanofibers assembled in a layer-by-layer manner infiltrated with PEO. The ultimate tensile strength, Young's modulus and shear modulus were $\sigma = 170 \pm 5$ MPa, $E = 5.0 \pm 0.05$ GPa and $G = 1.8 \pm 0.06$ GPa,[110] respectively, which are much higher than those of bare PEO electrolyte ($\sigma \approx 1$ MPa, $E < 100$ MPa, $G < 10$ MPa).[110,114] Most importantly, the pore size of the composite electrolyte was only 20 nm. The combined mechanical strength with small pore size effectively prevented copper dendrite growth at a current density of 10.3 mA cm^{-2}. In a lithium symmetrical cell using the composite electrolyte, it lasted 2500 cycles at a current density of 0.25 mA cm^{-2}. It is interesting to note the shear modulus of the Kevlar nanofibers and PEO composite is actually smaller than that of lithium, a violation of the Monroe and Newman criterion,[34] yet it still suppressed lithium dendrite growth. They attributed this to the small pore size of the composite electrolyte (20 nm), which is much smaller than the diameter of typical lithium dendrites (a few hundred nm); as such, the dendrites were suppressed at the lithium and electrolyte interface.

In summary, most research studies have been focused on constructing hybrid PEO SSEs with high moduli to inhibit dendrite growth according to the theory of Monroe and Newman.[34] However, dendrites can grow and penetrate both pure and reinforced PEO electrolytes with elastic moduli lower or much higher than that of lithium,[126,127] implying that the SSE modulus (Young's modulus or shear modulus) may not be the only mechanical factor limiting dendrite growth. Several other mechanical parameters such as yield stress, tensile strength, and the strain of elongation at break of PEO-derived SSEs should also be considered in suppressing dendrite penetration. Moreover, dendrite growth in PEO SSEs is also determined by many other factors such as the current density,[128] the mechanical strength of the supporting structure for PEO,[110] and the pore size of the supporting structure.[69] The mechanical strength of the PEO is not the only controlling element. It is the electro-chemo-mechanics that dictates the dendrite growth and penetration in PEO-based SSEs; for example, enhancing the ionic conductivity can suppress lithium dendrite growth even with a low modulus of 0.1 MPa *via* the cross-linked polyethylene/PEO electrolytes.[129]

3.3. Electro-chemo-mechanics of ''dead'' lithium in SSLMBs

Another serious problem for the applications of LMBs is the formation of inactive or ''dead'' lithium during plating/stripping cycling. ''Dead'' lithium consists of diverse lithium compounds within the SEI, such as LiF, Li_2CO_3, Li_2O, $ROCO_2Li$, and inactive metallic lithium which is electrically isolated. The formation mechanism and quantification of ''dead'' lithium have been investigated in liquid organic electrolyte based LMBs.[130–132] The ''dead'' lithium in the SEI is accumulated with increased plating/stripping cycling due to the continuous reaction between the newly deposited lithium and the electrolyte. The metallic ''dead'' lithium is often caused by the preferred stripping from the root rather than the tip of the lithium dendrite.[130,132] The formation of ''dead'' lithium often causes the capacity loss and volume expansion of the lithium anode, which deteriorate the performance of LMBs. Fang *et al.* distinguished the inactive lithium in the SEI and the inactive metallic lithium by combining water titration and gas chromatography.[131] The content of inactive metallic lithium was determined by the reaction of $2Li + 2H_2O \rightarrow 2LiOH + H_2$. For comparison, few studies about ''dead'' lithium in SSLMBs were reported possibly due to the buried interfaces, making *in situ* characterization difficult. Wang *et al.* investigated Li/garnet interfaces *via* neutron depth profiling (NDP) and found the formation of ''dead'' lithium in SSLMBs, and then suggested a promising strategy to decrease the ''dead'' lithium.[133] Strategies such as 3D host structures, high stack pressure and improved wettability between the lithium anode and SSEs, reducing the interfacial resistance, thus rendering uniform lithium deposition/stripping, may be adopted. In summary, "dead" lithium in SSLMBs is an unexplored research area; more research studies are required in this area.

4. Interfaces in SSLMBs

Another major roadblock in SSLMBs is the high interfacial resistance that originated from the poor solid–solid contact and the deleterious chemical or electrochemical Li/SSE interfacial reactions.[134,135] Thermodynamically most SSEs are not stable with lithium, and they are chemically reduced to form detrimental interfacial reaction products upon contacting lithium.[40,136,137] High interfacial resistance reduces the critical current density (CCD) and the lifetime of SSLMBs. Great endeavors have been devoted towards reducing the interfacial resistance and improving the interfacial stability, which include applying an external pressure to improve the physical contact between lithium and the SSEs, interlayer coating to modify the wettability of the Li/SSE interface and prevent detrimental interfacial reactions, and interface modification. These strategies aim to improve the physical contact and/or the chemical and electrochemical compatibility between lithium and the SSEs. A detailed account is provided in the following.

4.1. Stack pressure

It has been shown that the application of mechanical pressure is beneficial to the cycle life and plating morphology of lithium metal cells.[81,138–145] The benefit of applied pressure is thus to confine lithium growth and plastically deformed lithium to maintain a more planar, low surface area morphology. During lithium stripping, the stack pressure may mitigate void formation in the lithium anode by pressure induced creep of lithium.

4.1.1. Stack pressure in LLZO based SSLMBs. Krauskopf *et al.* showed that mechanical pressure has a very strong effect on the interface kinetics in LMBs because of the plastic deformation of lithium.[138] They investigated the interfacial resistance changes with different external pressures in a Li/LLZO/Li symmetric cell, and they found that the Li/LLZO interfacial resistance became very small and decreased virtually to 0 Ω cm^2 at a high external pressure of 400 MPa.[138] They interpreted this observation by the concept of constriction resistance and showed that the contact geometry in combination with the ionic transport in the SSE dominated the interfacial contributions for a clean interface in equilibrium. Constriction resistances are electrical contact resistances that are caused by insufficient contact between electrical conductors and the resulting current line bundling near discrete contact spots. This theory originally describes the contact resistance of monometallic contact surfaces by separate contact spots that increase their contact area because of plastic deformation under an applied force. The distribution of these spots is defined by the small-scale surface roughness as schematically shown in Fig. 9a. The constriction resistance can be calculated through eqn (4), which is determined by the applied force N and the Vickers hardness H and the electrical resistivity ρ or conductivity σ of the contacted materials.

$$R_{\text{int}} = \frac{\rho}{2} \cdot \sqrt{\frac{\pi \cdot H}{N}} = \frac{1}{2 \cdot \sigma_{\text{Li}^+}} \cdot \sqrt{\frac{\pi \cdot H_{\text{Li}}}{N}} \tag{4}$$

Fig. 9b shows the theoretically estimated and the experimentally determined interfacial resistances, which agree very well with each other. The authors showed that by increasing the pressure to 400 MPa in an isostatic press setup, no interfacial resistance contributions were observed anymore, proving that the interface is not intrinsically highly resistive and that very high pressures are necessary at room temperature to obtain intimate and complete contact between lithium and the SSE. They showed further that the contact resistance increase during charge was caused by pore formation in the lithium anode, and applying external pressure might erase the pore due to the creep of lithium, thus reducing the contact resistance. As shown in Fig. 9c, if the local current density does not exceed the vacancy diffusion limit in the metal, the interface remains structurally stable (left in Fig. 9c). When the externally applied local current density exceeds the diffusion limit, vacancies supersaturate and accumulate to form pores near the interface, which will grow and lead to increasing contact loss (middle in Fig. 9c). Adatom diffusion of the metal pore surface may cause a second, higher diffusion limit. For comparison, when external pressure is applied, pores will be annihilated because of the plastic deformation of the lithium metal and contact loss is restricted (right in Fig. 9c).[138] Kasemchainan *et al.* confirmed that higher stacking pressure tends to suppress void formation, thus permitting higher current density during cycling.[81] They found that creep rather than lithium diffusion dominates the lithium transport to the interface. Therefore, the external pressure should be higher than the yield stress of lithium to achieve its plastic deformation *via* creep to replenish lithium to the voids formed during lithium stripping. Based on eqn (1), the strain rate of lithium is proportional to the exponent of stress during the creep of lithium. The higher external pressure would provide more driving force to replenish lithium to the voids, leading to a higher CCD on lithium stripping.

A CCD on stripping is identified that results in dendrite formation on plating and cell failure.[81] When the stripping current density removes lithium from the interface faster than it can be replenished, voids form in lithium at the interface and accumulate on cycling, increasing the local current density at the interface and ultimately leading to dendrite formation on plating, short circuit and cell death. The CCD increases with increasing stack pressure on stripping, indicating lithium creep as the dominant mechanism for transporting lithium to the Li/LPS-Cl interface. Similar results were reported in the sodium/Na–β″-alumina interface.[139] They suggested that considerable pressure might be required to achieve even moderate power densities in solid-state cells. It is interesting to note that the LLZO SSE appears to be able to sustain a high stack pressure of 400 MPa without fracture, as the fracture stress of LLZO is about

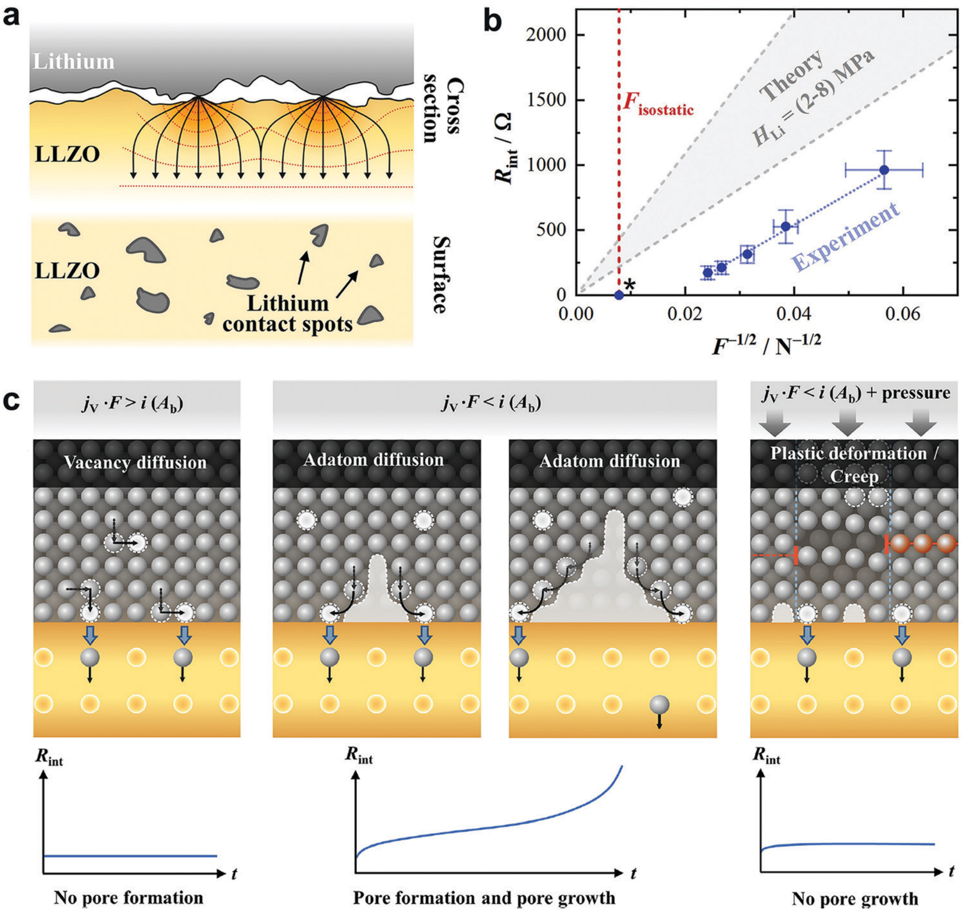

Fig. 9 Effect of stack pressure in the lithium deposition in garnet SSEs. (a) Schematic representation of the Li/LLZO interface showing a few contact points as the origins of constriction and the resultant bending of the current lines at the interface, which is the basis of the applied theory. The arrows schematically indicate current lines. Equipotential lines are shown as red dotted lines. (b) Calculating the interfacial resistances assuming a Vickers hardness for lithium in the range from 2 to 8 MPa gives a gray background area. (c) Schematic of the different mechanisms that facilitate charge transfer at the lithium metal anode under anodic load (limiting cases). (Reproduced with permission.[138] Copyright 2019 American Chemical Society.)

250 MPa for a flaw size of about 5 μm. The reason for the high fracture resistance of LLZO is unclear and warrants further investigation.

Wang *et al.* utilized stack pressure to correlate mechanics with the electrochemical behavior of Li/LLZO/Li symmetric cells during galvanostatic cycling.[140] They demonstrated that significant polarization occurs at a current-dependent "critical stack pressure". The polarization is attributed to the increased interfacial resistance caused by voids present at the interface during lithium stripping. The authors suggested that at low pressures the lithium stripping rate exceeds the rate of replenishing *via* lithium creep at the interface, inducing the formation of voids and ultimately increasing resistance. These results are consistent with those reported by Krauskopf *et al.*[138]

In short, stack pressure renders intimate contact between lithium and LLZO due to the creep of lithium, thus reducing the contact resistance dramatically. Under high external pressure, creep rather than lithium diffusion is the dominant mechanism transporting lithium to the interfaces. As room temperature corresponds to a homologous temperature of $0.66T_m$ for lithium,[78] high pressure and high temperature promote creep of lithium dramatically under normal battery operation conditions. Stack pressure is particularly important in the lithium stripping process, as the high stack pressure facilitates the creep of lithium, so that the replenishment overwhelms the removal of lithium during stripping, thus avoiding the formation of voids at the Li/SSE interface, which is the rate limiting factor for the lithium anode. Results of a kinetic model proposed by Krauskopf *et al.* showed that the interface remains morphologically stable only when the anodic current density does not exceed a critical value of approximately 100 μA cm^{-2}, which is not high enough for practical cell setups employing a planar geometry.[138] They highlighted that future research on lithium metal anodes on SSEs needs to focus on the transport within and the morphological instability of the metal electrode. Obviously CCD for stripping corresponding to the removal of lithium was determined by the external pressures before the SSE fractured, since the pressure dominates the creep induced lithium transport.

4.1.2. Stack pressure in sulfide based SSLMBs.

Doux *et al.* studied systematically stack pressure influence on the performance of SSLMBs using LPS-Cl electrolyte.[145] They showed that the stacking pressure impacts dramatically the short circuit and longevity of SSLMBs. Namely, at 75 MPa stack pressure, the

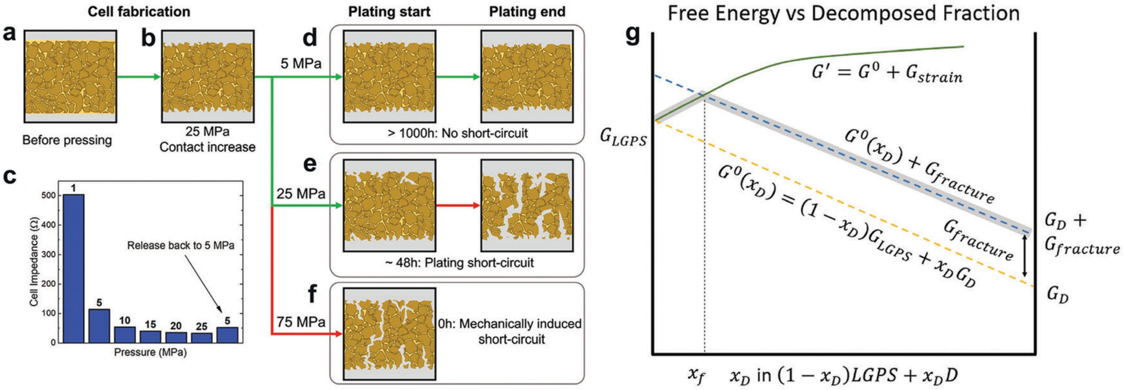

Fig. 10 Effect of the stack pressure on the shorting behavior of SSLMBs. (a) During cell fabrication, the contact between the electrolyte and lithium metal was poor before pressing the lithium metal on the electrolyte pellet. (b) Pressing the lithium metal at 25 MPa allowed for proper wetting of the electrolyte and (c) induced a large drop in the symmetric cell impedance, even when the pressure was later released to 5 MPa. (d) Plating and stripping at a stack pressure of 5 MPa: no creeping of lithium inside the SSE pellet was observed and therefore the cell cycled for more than 1000 h. (e) At a stack pressure of 25 MPa, lithium slowly creeped between the grains of the SSE and plating occurred on these dendrites, eventually shorting the cell after 48 h. (f) When the stack pressure was too high, lithium creeped through the electrolyte and formed dendrites that mechanically short the cell. (Reproduced with permission.[145] Copyright 2020 Wiley-VCH Verlag GmbH & Co. KGaA, Weinheim.) (g) Illustration of the impact of strain on LGPS decomposition, where x_D is the fraction of LGPS that decomposed. The dashed orange line represents the Gibbs energy ($G_0(x_D)$) of a binary combination of pristine LGPS and an arbitrary set of decay products (D) when negligible pressure was applied. The solid-green line shows the Gibbs energy when a mechanical constraint was applied to the LGPS. (Reproduced with permission.[147] Copyright 2019 Wiley-VCH Verlag GmbH & Co. KGaA, Weinheim.)

LMB cell already shorted before cycling began due to lithium creeps through pores in the SSE (Fig. 10a–f). At 25 MPa, the cell cycled for 48 hours before failure. At 5 MPa, the cell cycled for more than 1000 h before short circuit failure. The authors attributed the longer cycle lifetime at lower stacking pressure to the creep properties of lithium, which is unable to creep into the pores of the SSE at low pressure. They showed further that the impedance of a lithium metal symmetric cell depended strongly on the pressure applied to improve the contact between the electrolyte and the lithium. If a pressure of only 1 MPa was used, the cell impedance exceeded 500 Ω, which decreased to ≈110 Ω at 5 MPa, 50 Ω at 10 MPa, 40 Ω at 15 MPa, 35 Ω at 20 MPa, and 32 Ω at 25 MPa. The result is in accord with that reported by Krauskopf *et al.*[138] However, in a Li/LLZO/Li symmetric cell, a pressure as high as 400 MPa was required to reduce the Li/LLZO interfacial resistance to virtually 0 Ω. It appears that the stack pressure requirement for reducing the interfacial resistance is very different between garnet type SSEs and sulfide type SSEs, with the latter requiring much lower stack pressure than the former. The reason for the difference may be two fold. Firstly, sulfide electrolytes are much softer than LLZO; thus an intimate contact may be easier to establish in the former than in the latter. Secondly, lithium may exhibit better wettability with sulfide SSEs than with LLZO.

In addition to reducing the interfacial resistance, the electrochemically stable window of sulfide SSEs can be extended *via* the mechano-electrochemical effect by external stack pressure or core–shell confinement design, which efficiently improves the interfacial stability between the lithium anode and sulfide electrolytes.[146,147] As shown in Fig. 10g, since LGPS tends to expand upon decomposition, the Gibbs strain (G_{strain}) increases and acts as the mechanical stress to restrict the expansion of LGPS.[147] At some fracture point, denoted x_{f}, the Gibbs energy of the system exceeds the energy needed to fracture the mechanical constraints (the blue dashed line). The highlighted gray path is the suggested ground state for a mechanically constrained LGPS system. For this reason, the region $x_{\text{D}} < x_{\text{f}}$ is metastable. It is theoretically predicted that the stable electrochemical window of the LGPS SSE could be extended from 1.7–2.1 V to 1.2–3.9 V when the constraint's effective compressibility increases from 0 to 20 GPa.[147] A stability window of 0.7–3.1 V and a quasi-stability window of up to 5 V for $\text{Li}_{10}\text{Si}_{1+x}\text{P}_{2-x}\text{S}_{12}$ sulfide electrolytes with a high Si composition in the shell are achieved which are much larger than the previously predicted one of 1.7–2.1 V. The mechanical confinement of the amorphous shell on the crystalline core plays an important role in the voltage stability of $\text{Li}_{10}\text{Si}_{1+x}\text{P}_{2-x}\text{S}_{12}$ sulfide electrolytes.[146] A mechanical constriction for the LGPS *via* a graphite layer under 100 MPa external pressure made the Li/LGPS/Li cell operate at an ultrahigh current density of 10 mA cm^{-2} without short-circuit and lithium dendrite formation.[148]

In summary, mechanical pressure reduces the interfacial resistance, extends the electrochemical stability window and increases the CCD of sulfide SSEs. The pressure required to achieve a low interfacial resistance is much smaller in the Li/sulfide interfaces than the Li/LLZO interfaces, possibly due to the softer sulfide electrolyte rendering intimate contact between lithium and sulfide at lower pressures. In fact, if the pressure is too high, lithium may creep to short the cell directly in sulfide based SSLMBs. The electrochemically stable window of the LGPS SSE can be extended from 1.7–2.1 V to 1.2–3.9 V when the constraint's effective compressibility increases from 0 to 20 GPa. The correlations between the external pressure and the CCD of both stripping and plating need further investigations by considering the interplay of mechanics and electrochemistry/chemistry to control the interfacial stability of sulfide based SSLMBs.

4.2. Chemo-mechanics of the Li/LLZO interface—the wettability

A major issue with the Li/LLZO interface is the interface wettability.[135,149,150] The wettability between lithium and LLZO is a critical factor in determining the interfacial resistance; namely, a fully wetted Li/LLZO interface leads to a very low interfacial resistance; in contrast, a poorly wetted Li/LLZO interface causes very high contact resistance. A review of the Li/LLZO interfacial wettability provides vital information regarding how to improve the wettability between lithium and LLZO, thus improving the battery performance. Moreover, the wettability between lithium and LLZO is indeed related to the lithium mechanics, as the wettability or the adhesion strength between lithium and LLZO is determined by the interplay between the surface tension of lithium metal and the interfacial bonding strength and interactions, which are closely related to the chemo-mechanics of lithium and LLZO. Indeed, Wang *et al.* correlated the interface resistance with the interfacial adhesion of the Li/LLZO interface,[151] and they found that when the tensile adhesion strength was 1.1 kPa, the interfacial resistance was 330 kΩ cm^2. By contrast, when the tensile adhesion strength reached 8 MPa, the interfacial resistance decreased to 7 Ω cm^2. Apparently lithium mechanics plays a vital role in the wettability of the interfaces and in turn the interfacial resistances. Therefore it is critical to improve the wettability between lithium and LLZO so as to boost the battery performance.

There are conflicting reports regarding the wettability of the LLZO surface to lithium. One of the complications arises from the surface conditions of LLZO, *i.e.* whether or not it is covered with a surface Li_2CO_3 layer. When LLZO is exposed to air, it reacts with moisture and CO_2 to form Li_2CO_3, which is lithiophobic. Although many reports claim that the surface of LLZO was cleaned up by mechanical polishing, or physical or chemical treatment before assembling a cell, complete removal of Li_2CO_3 is not trivial.[149,150] The consensus appears to be that a clean LLZO surface without any Li_2CO_3 contamination is lithiophilic, while that with Li_2CO_3 is lithiophobic.

Sharafi *et al.* experimentally measured the contact angles between the molten lithium and LLZO with and without the Li_2CO_3 surface, which were 142° and 95°, respectively (Fig. 11a–d).[152] The interfacial adhesion energies were calculated to be 0.1 and 0.67 J m^{-2} for the Li/Li_2CO_3 and Li/LLZO interfaces, respectively, and the calculated wetting angles were 142° and 95° for the former and the latter, respectively (Fig. 11e and f).[152] The larger wetting angle obtained by calculation than by experiments was attributed to the incomplete removal of Li_2CO_3 in the experiments. The higher interfacial adhesion energy of the Li/LLZO interface than that of the Li/Li_2CO_3 interface indicates a stronger interfacial interaction in the former than in the latter. There are also reports that wettability is controlled by the lithium metal, not LLZO; as such, by alloying lithium with carbon or by removing the surface Li_2O layer in lithium, the Li/LLZO interface becomes lithiophilic, regardless of the surface species on LLZO.[153]

In short, enormous efforts have been devoted towards modifying either the LLZO surface or the lithium surface to obtain a lithiophilic interface so as to reduce the Li/LLZO interfacial resistance (Table 3). Strategies such as physical treatment (mechanical polishing, frictional rubbing, heat treatment), chemical treatment (carbon reduction, acid treatment, viscosity tuning) and interlayer deposition were adopted, which are summarized in the following. The artificial interlayer also plays an important role as a stable "SEI film" on garnet LLZO-based electrolytes during plating/stripping cycles, improving the power density and long-term cycling stability of cells. A brief overview of these techniques is provided in the following.

4.2.1. Artificial interlayers. Luo *et al.* changed the chemical properties of garnet $Li_{6.85}La_{2.9}Ca_{0.1}Zr_{1.75}Nb_{0.25}O_{12}$ (LLCZN) from lithiophobic to lithiophilic through an ultrathin coating of amorphous Si with a thickness of 10 nm deposited by plasma-enhanced chemical vapor deposition (PECVD).[154] The wettability transition was due to the reaction between lithium and Si and the *in situ* formation of lithiated Si. As a result, a Li/Si–LLCZN/Li symmetric cell exhibited much smaller impedance and excellent stability upon plating/stripping cycles compared to cells using bare garnet SSE. Coatings of Au,[155] Ag,[156] Sn,[157] and Ge[158] have similar effects to that of Si, which is essentially caused by the reaction of lithium with these elements to form lithiophilic alloy phases, thus reducing the interfacial resistances. Dipping LLZO into a molten Li–Sn alloy also has a similar effect to the coating of Sn onto the surface of LLZO.[159]

Huo *et al.* used magnetron sputtering to deposit a 24 nm thick Cu_3N film on the surface of LLZTO, which was then subjected to reaction with molten lithium to form a Cu/Li_3N MIEC layer.[160] The Li/MIEC/LLZTO interfacial resistance was much lower (38.4 Ω cm^2) than that of the Li/LLZTO interface (1138.5 Ω cm^2). The CCD under which the cell failed reached a record value of 1.2 mA cm^{-2} for the Li/MIEC/LLZTO/Li cell, thanks to the reduced interfacial resistance. Because the Cu nanoparticles dispersed in the Cu_3N matrix are excellent electronic conductors, the MIEC layer renders a uniform electric field distribution, thus preventing lithium dendrite formation effectively. Coatings of MoS_2,[161] Li_3N,[162] and ZnO[163] produced similar effects to that of Cu_3N.

The interfacial resistance was reduced by using atomic layer deposition (ALD) of a thin layer of Al_2O_3 5–6 nm in thickness on the surface of the LLCZN SSE.[154] Experimental and computational results revealed that the oxide coating enabled wetting of metallic lithium in contact with the garnet electrolyte surface and the lithiated-alumina interface allowed effective lithium ion transport between the lithium metal anode and garnet electrolyte.

Zhang *et al.* coated the LLZTO surface with Na, then lithium disk was attached to the Na-coated LLZTO and heated at 230 °C for 30 min, where a eutectic Na–Li intermediate layer was formed between lithium and LLZTO.[164] They showed that Li–Na alloy exhibits better wettability with LLZTO than either lithium or Na with LLZTO. Symmetric lithium cells with a Li–Na interlayer showed a resistance of 38 Ω cm^2 at 60 °C, which is significantly lower than that of symmetric lithium cells without an interlayer (1144 Ω cm^2). Fu *et al.* reported that melt-casting lithium doped with 0.5 wt% Na on the surface of a LLZTO SSE can reduce the Li/LLZTO interfacial resistance due to the transfer of Li_2CO_3 from the grain boundaries of the LLZTO to the surface of lithium.[150]

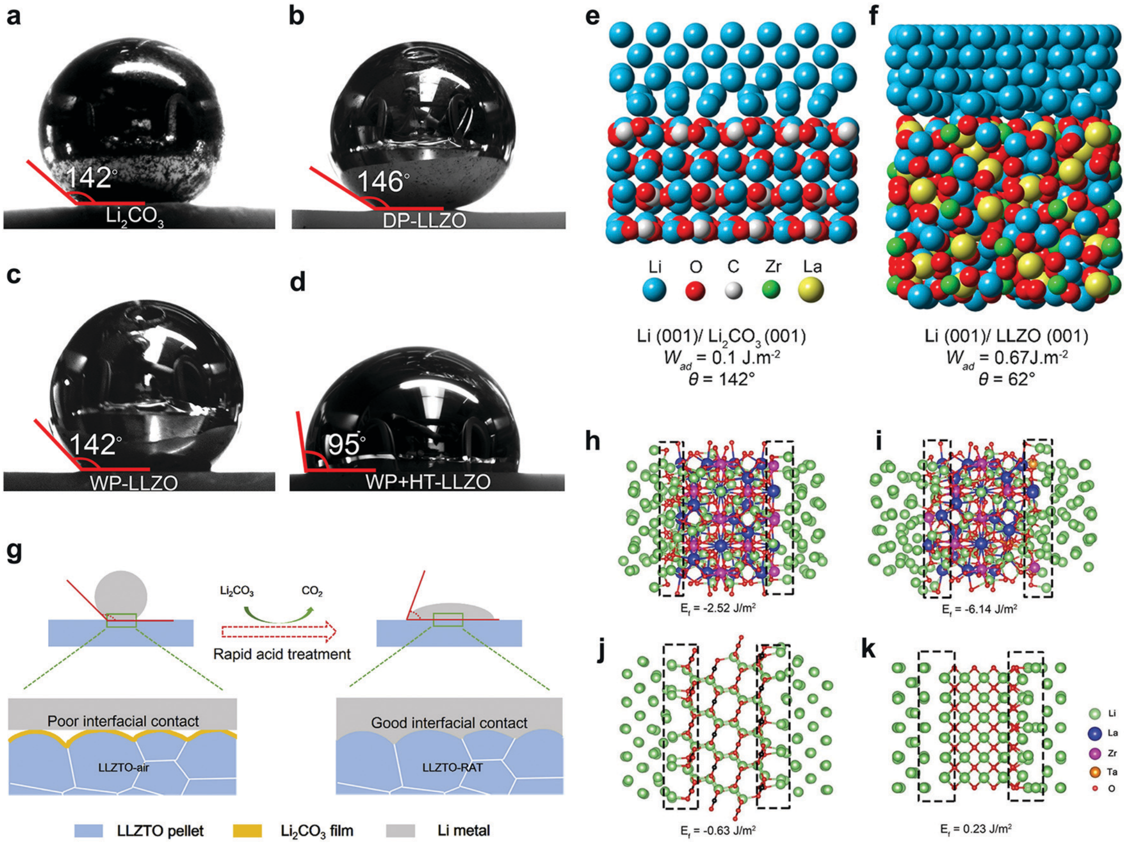

Fig. 11 Lithium wetting on LLZO SSEs. (a–d) Contact angle measurements of molten lithium on (a) Li_2CO_3, (b) dry polished-LLZO, (c) wet polished-LLZO, and (d) wet polished-LLZO after heat treatment at 500 °C. (Reproduced with permission.[152] Copyright 2017 American Chemical Society.) (e and f) Calculated works of adhesion (W_{ad}), contact angles (θ), and atomic structures for the (e) Li/Li_2CO_3 and (f) Li/LLZO interfaces. (Reproduced with permission.[152] Copyright 2017 American Chemical Society.) (g) Schematic illustration of the Li/LLZTO interface before and after rapid acid treatment. (Reproduced with permission.[166] Copyright 2019 Published by Elsevier Ltd.) (h–k) First-principles calculations of different interfaces: Li/LLZO (h), Li/LLZTO (i), Li/Li_2CO_3 (j), and Li/Li_2O (k). (Reproduced with permission.[153] Copyright 2020 Wiley-VCH Verlag GmbH & Co. KGaA, Weinheim.)

4.2.2. Chemical and physical treatments. Chemical treatments including carbon reduction, acid treatment and heat treatment are widely used to improve the lithium wetting on the LLZO.

Li *et al.* introduced a simple method to remove Li_2CO_3 and the protons in the garnet framework by reacting garnet with carbon at 700 °C, in which carbon reacts with Li_2CO_3 on garnet *via* $Li_2CO_3 + C \rightarrow Li_2O + 2CO$ to remove all the Li_2CO_3 from the garnet.[165] Consequently, the surface of the garnet turned from lithiophobic to lithiophilic, and the Li/LLZTO-C interfacial resistance changed from 1210 to 28 Ω cm^2.

Huo *et al.* introduced a rapid acid treatment method to remove the surface Li_2CO_3 layer on LLZTO, and turned the original lithiophobic surface to lithiophilic (Fig. 11g).[166] As such, the interfacial resistance decreased from 940 to 28 Ω cm^2. The removal of Li_2CO_3 was based on the following chemical reaction: $Li_2CO_3 + 2HCl \rightarrow 2LiCl + CO_2 + H_2O$. They reported that it took only 30 s to remove all the Li_2CO_3 from the LLZTO surface, and longer acid treatment deteriorates the ionic conductivity of the SSE, which could be attributed to acid corrosion to the porous SSE that weakened the Li^+ migration across grain boundaries.

The surface structure of LLZTO can be modified by heat treatment.[167] The rationale is that with increasing heat-treatment temperature some Li_2CO_3 on the LLZTO surface was removed due to the thermal decomposition of Li_2CO_3, leading to a thinner insulating layer, which then resulted in lower interfacial resistance. The interfacial resistance reached a minimum at 700 °C, which is close to the Li_2CO_3 decomposition temperature. The interfacial resistance increased for cells with LLZTO heat-treated at 800 °C, which is the temperature when LLZTO starts to decompose. A similar heat treatment effect was observed in LLZO.[168]

It was reported by the same group that by combining wet polishing and heat treatment of LLZO, a clean LLZO surface with virtually no Li_2CO_3 was obtained.[152] Remarkably, such careful control of surface chemistry reduced the interfacial resistance to 2 Ω cm^2, lower than that of liquid electrolytes, without the need for interlayer coatings. The origin of ultra-low resistance was associated with interfacial chemistry, lithium wettability, and electrochemical phenomena. The Li/LLZO interface without Li_2CO_3 exhibits much better adhesion and wettability than the Li/Li_2CO_3 interface. From this study, it can be concluded that the high interfacial resistance between lithium and LLZO SSEs presented in the vast amount of previous studies originates mainly from the surface species

Table 3 Wetting properties of lithium with LLZO derived SSEs

SSE	Surface W/WO Li_2CO_3, modification	Wettability	Cell configuration	$R_{interface}$ (Ω cm^2)	Stable current density (mA cm^{-2})/lifetime (h)	Ref.
LLCZN (LLZO doped with Ca, Nb)	No	LPHO	Li/SSE/Li	925	—	154
	Si interlayer	LPHI	Li/Si-coated SSE/Li	127	0.2/30	
LLCZN	No	LPHO	Li/SSE/Li	1710	—	169
	Al_2O_3 interlayer	LPHI	Li/ALD Al_2O_3-coated SSE/Li	34	0.2/90	
LLZTO	No	LPHO	Li/LLZTO/Li	1138.5	0.1/8	160
	Cu_3N + Li → Cu + Li_3N MIEC layer	LPHI	Li/LLZTO/MIEC/Li	38.4	0.1/1000	
			Li/LLZTO/LCO	3354.7	—	
			Li/LLZTO/MIEC/LCO	1029.2	—	
LLZTO	Thin layer Au	LPHI	Li/LLZTO/Li	1500	0.5/∼0.04	155
			Li/Au/LLZTO/Au/Li	190	0.5/22.5, 0.25/150	
LLZTO	No	LPHO	Li/LLZTO/Li	572 at 60 °C	0.05/8 at 60 °C	164
	Na interlayer	LPHI	Li/Na/LLZTO/Na/Li	54 at RT, 19 at 60 °C	0.1/3000 (60 °C), 0.1/600 (RT)	
			Li/Na/LLZTO/LFP	—	—	
			Li/Na/LLZTO/FeF_3 + IL	—	—	
LLZTO	Yes	LPHO	Li/LLZTO/Li	1210 at RT, 725 at 65 °C	0.05/∼7	165
LLZTO-C	Carbon treatment	LPHI	Li/LLZTO-C/Li	28 at RT, 9 at 65 °C	0.4/150	
			Li/PEO/LLZTO-C/PEO/Li	—	1/100 at 65 °C	
			Li/LLZTO-C/LFP + PEO	92 at 65 °C	0.1/40 cycle at 65 °C	
LLZTO	Yes	LPHO	Li/LLZTO–air/Li	940	0.1/5	166
	Rapid acid treatment	LPHI	Li/LLZTO–RAT/Li	26	0.2/700	
			Li/LLZTO–air/LFP	—	—	
			Li/LLZTO–RAT/LFP	3513.4	—	
			Li/LLZTO–RAT/LCO	1978.2	—	
LLZTO	No	LPHI	Li_F/LLZTO/Li_F	—	0.1/70	153
	No	LPHI	Li_R/LLZTO/Li_R	6.95	13.3/80	
	Rubbing LLZTO in molten Li	LPHI	Li_R/LLZTO/Li_R	492.6	0.1/50	
LLZTO	No	LPHO	Li/LLZTO/Li	381	0.3/3	173
	Li–C composite	LPHI	Li–C/LLZTO/Li–C	11	0.3/250	174 175
LALZWO	Pencil drawing graphite, 1 μm		Li/LALZWO/Li	675	0.05/20	176
			Li/C–LALZWO–C/Li	52.5	0.3/100	
			Li/C–LALZWO–C/NMC532	—	—	
LLCZNO	Cu_6Sn_5 interlayer		Li/LLCZNO/Li	1489	0.1/38	157
			Li/Sn–LLCZNO/Li	168	0.25/300	
			Li/Cu_6Sn_5LLCZNO/Li	236	0.25/300	
			Li/LLCZNO/LCO	1081 at 100th cycle	—	
			Li/Sn–LLCZNO/LCO	767 at 100th cycle	—	
			Li/Cu_6Sn_5LLCZNO/LCO	356 at 100th cycle	—	
LLZTO	MoS_2 interlayer		Li/LLZTO/Li	62	0.2/25	161
			Li/MoS_2–LLZTO–MoS_2/Li	14	0.2/40	
LLZTO	Yes	LPHO	Li/LLZTO/Li	1256 at 60 °C	0.2/30 at 60 °C	162
	Li_3N interlayer	LPHI	Li/Li_3N–LLZTO–Li_3N/Li	90 at 60 °C	0.2/150 at 60 °C	
			Li/Li_3N–LLZTO–Li_3N/LFP	71 at 60 °C	—	
LLCZNO	Ag interlayer, 100, 300, 500 nm		Li/LLCZNO/Li	1534	0.1/72	156
			Li/Ag–LLCZNO/Li	66	0.2/100	
			Li/Ag–LLCZNO/LMO	—	—	
LLCZNO	Ge interlayer 20 nm, e-beam evaporation		Li/LLCZNO/Li	925		158
			Li/Ge–LLCZNO–Ge/Li	115		
			Li/Ge–LLCZNO–Gel/LFP	—		
LLCZNO	Yes	LPHO	Li/LLCZNO/Li	1900	—	163
	ALD ZnO 30 nm	LPHI	Li/ZnO–LLCZNO–ZnO/Li	450	0.1/50	
LLZO	Polishing & heat treatment		Li/LLZO/Li	From 200 to 1	0.2/200	152
LLZTO	PEO–LiTFSI & temperature		Li/PEO–LiTFSI–LLZTO-PEO–LiTFSI/Li	10 800 180 after heat treatment	0.03/1.7 0.03/7	167
LLZAO	LLZAO-SG: 20–40 μm		Li/LLZO-SG/Li	37		178
	LLZAO-LG: 100–200 μm		Li/LLZO-LG/Li	130		
LLZO	Temperature		Li/LLZO/Li	5822		168
			Li/LLZO/Li, heating to 175 °C cooling to RT	514		
				2.7 for 175 °C treated cell		

Li_F: Li foil; Li_R: rubbing LLZTO in molten Li; W/WO: with/without; RT: room temperature; $R_{interface}$: interfacial resistance; LPHO: lithiophobic; LPHI: lithiophilic.

such as Li_2CO_3 and LiOH. Therefore, it is a prerequisite to obtain a clean SSE surface in order to achieve a low interfacial resistance.

4.2.3. Rubbing LLZTO in molten lithium.

Zheng *et al.* argued that it is the Li_2O layer on the surface of lithium rather than Li_2CO_3 on the surface of SSE that dictates the resistance of the Li/SSE interface.[153] They reported very different results from the literature: namely regardless of with/without Li_2CO_3 on the LLZTO surface, the SSE is always lithiophilic. They showed that by rubbing a LLZTO pellet covered with a 3 nm thick Li_2CO_3 surface layer into a molten lithium sphere, a near intimate contact between lithium and LLZTO was obtained. They suggested that by rubbing the LLZTO pellet in the molten lithium back and forth, the Li_2O layer on the surface of the lithium metal was broken, enabling fresh lithium to contact with the LLZTO surface, thus forming a lithiophilic Li/LLZTO interface with low impedance. First-principles calculations (Fig. 11h–k) showed that the interface formation energies of Li/LLZO, Li/LLZTO, Li/Li_2CO_3, and Li/Li_2O are −2.52, −6.14, −0.63, and 0.23 J m^{-2}, respectively, suggesting that the order of wettability with lithium is LLZTO > LLZO > Li_2CO_3 > Li_2O. In this context, the previous studies using interlayers (Al_2O_3, Si, Au, C) to modify the garnet surface and decrease the Li/LLZO interfacial resistance[155,165,169–171] were interpreted as using the interlayer to break the surface Li_2O layer on the lithium metal to obtain a lithiophilic Li/LLZTO interface with a low interfacial resistance, which reached as low as 6.95 Ω cm^2.[172] The low interfacial resistance led to a record high current density of 13.3 mA cm^{-2} in a Li/LLZTO/Li symmetric cell, which is even higher than the typical current density in liquid electrolyte based LIBs. However, this record high current density was obtained in a limited capacity measurement, which differs from the widely used time-constant measurement; therefore, the validity of their data needs further verification.

4.2.4. Li–C composites.

Duan *et al.* prepared a Li–C composite by mixing graphite powder into molten lithium, and they showed that the Li–C composite exhibited intimate contact with LLZTO.[173] They showed that the LLZTO surface without Li_2CO_3 was lithiophobic, which contradicts with other reports.[153,165,166] The improved Li–C/LLZTO interface contact may be attributed to the following three factors: (1) the viscosity of Li–C is 33 times higher than that of lithium, which decreased the surface tension of molten lithium; (2) the Li–C composite and LLZTO show favorable reaction with a small reaction energy of −20 to −100 meV per atom, suggesting a minor interfacial reaction, which facilitates the wettability; and (3) the surface Li_2CO_3 layer might still exist even after polishing the LLZTO pellet, and previous computation studies indicate a low binding energy between lithium and Li_2CO_3, rendering a poor contact between lithium and Li_2CO_3. Using a similar approach, replacing the graphite powder with g-C_3N_4[174] or BN nanosheets,[175] a Li–C_3N_4 or Li–BN composite renders good wettability between lithium and LLZTO. One additional advantage of Li–C_3N_4 or Li–BN over Li–C is that the former may form a fast lithium ion conductor, *i.e.* Li_3N, at the interface, which further improves the interface ion conductivity.

Pencil drawing graphite on $Li_{5.9}Al_{0.2}La_3Zr_{1.75}W_{0.25}O_{12}$ (LALZWO) generates similar results to a Li–C composite.[176] A graphite layer with a thickness of about 1 μm was coated on both surfaces of LALZWO pellets by pencil painting. Then, the coated pellets were sandwiched between two pieces of lithium metal (the thickness was 1 mm) to assemble the symmetric cells. After that, all cells were heated at 210 °C for 30 min under an Ar atmosphere so that LiC_6 was formed at the interface. The Li/SSE interface with a graphite layer exhibited lithiophilic characteristics.

4.2.5. Abietic resin coating.

Wang *et al.* reported a novel technique of converting a lithiophobic interface into a lithiophilic one through a simple abietic resin acid coating.[177] The surface of Cu foil is lithiophobic; however, after coating abietic resin acid, the Cu surface became lithiophilic. The authors attributed the change to the formation of Li–O and Li–C bonds which are the main driving forces for the improved wettability of molten lithium. Molten lithium reacted with molten abietic resin acid to form a mixture of LiOH, Li_2O/–COOLi, LiC_6, Li_2C_2, carboxy, methyl, and methylene groups at the Li/Cu interface. The effect of abietic resin acid coating is extended to organic coatings with –COOH, –OH, –SO_3H, –NH_2, –NH–, –Si–O, –F, –Cl, –Br, and –I groups, or element additives including Mg, In, Ca, Sr, Ba, Sc, Y, Rh, Ir, Pd, Pt, Au, Cd, Hg, Ga, Tl, Ge, Pb, As, Sb, Bi, S, Se, and Te.[177] The formation of Li–O, Li–N, Li–F, Li–Cl, Li–Br and Li–I bonds derived from the O, N, F, Cl, Br, and I-containing organic groups contributed to the improved wettability between molten lithium and the organic coating. When the inorganic alloying elements were introduced into lithium, the surface tension of molten lithium decreased, and the liquid metals could easily spread onto the substrates. Intrinsically, the mechanisms of the improved wettability of molten lithium by the chemical strategy are ascribed to the negative free energies for the reactions between molten lithium and lithiophilic substances and the newly formed bonds favoring better wettability.

4.2.6. Size effect on the interfacial resistance.

Cheng *et al.* reported that LLZO with smaller grain size exhibited smaller interfacial resistance.[178] They synthesized Al-substituted LLZO (LLZAO) with different grain sizes: *i.e.* LLZAO-SG samples with 10–20 μm grain sizes and LLZAO-LG samples with 100–200 μm grain sizes. The interfacial resistances of the Li/LLZAO-SG and Li/LLZAO-LG samples were 37 and 130 Ω cm^2, respectively, and the CCDs were 0.134 and 0.09 mA cm^{-2}, respectively. The authors concluded that the better performance observed for the small-grained samples was attributed to the larger relative amount of surface layer grain boundaries, rather than grain orientation and grain boundary misorientation effects. They suggested that LLZO SSEs should have small grains and multiple grain boundaries to ensure the good performance of SSLMBs. However, the physics and chemistry behind this grain size dependent interfacial resistance are unclear. In fact, grain boundaries hinder ion conduction;[179,180] thus more grain boundaries should deteriorate rather than improve the performance of SSLMBs.

A similar grain size effect was observed in Na–β″-alumina (composition: 8.85 wt% Na_2O; 0.75 wt% Li_2O; balance Al_2O_3).[181]

The CCDs were 240 and 700 mA cm^{-2} for samples with grain sizes of 5.2 and 1.1 μm, respectively. Na dendrite induced breakdown was initiated at lower average current densities for larger grain size electrolyte. The fracture strengths of the SSEs decreased significantly with increasing grain size. Therefore, a connection between the CCD and fracture strength of the SSE was established: that is, the higher the fracture strength of SSE, the higher the CCD, suggesting that the electrochemical failure and mechanical failure were inter-related. Although the mechanical failure and electromechanical failure are not equivalent, it should be stressed that the mechanical properties strongly affect the electrical ones.[181]

In summary, physical treatment such as mechanical polishing, frictional rubbing, and heat treatment; and chemical treatment including carbon reduction, acid treatment, and interlayer and abietic resin acid coating can improve the wettability of lithium with LLZO and reduce the interfacial resistance and thus improve the CCD. The principle of these treatments is to either reduce the surface tension of lithium or change the LLZO surface from lithiophobic to lithiophilic. Reducing the grain size of the SSE improves not only its mechanical properties but also the CCD.

4.3. Stability of Li/Na-superionic conductor (NASICON) and Li/sulfide interfaces

Theoretical calculation indicates that the chemical/electrochemical stability windows of NASICON and sulfide SSEs with lithium are much narrower than that of LLZO. Therefore, the issues in the Li/NASICON and Li/sulfide interfaces arise mainly from the deleterious interfacial reactions rather than from the wettability to lithium. Interfacial reactions usually cause large volume changes of the interfaces, and cyclic volume expansion and shrinkage lead to the formation of a large number of cracks even fracture of the SSEs, causing mechanical failure of the cells.[182] Furthermore, interfacial reactions may generate insulating interphases at the interfaces, which increase the interfacial resistance and in turn the polarization, and eventually lead to the failure of the cell.[170] In this context, our overviews of the interfacial stability of NASICON and sulfide SSEs focus mainly on the chemical/electrochemical reactions of SSEs with lithium, electro-chemo-mechanically interfacial degradation mechanisms and mitigation strategies.

4.3.1. Lithium reactions with NASICON and sulfide SSEs

4.3.1.1. Theoretical prediction of interfacial reactions. To investigate the chemical/electrochemical interfacial stability between the lithium anode and SSEs, Zhu *et al.*[183] and Richards *et al.*[137] performed first principles calculations to predict the thermodynamics of the reactions between the SSEs and lithium. The results demonstrate that almost all the Li/SSE interfaces are thermodynamically unstable, because they can be reduced by the highly reactive lithium with a low redox potential (Fig. 12a). The predicted high reduction potentials of 1.75 and 2.16 V for perovskite LLTO and NASICON-type LATP, respectively, are in accord with the reduction potentials of 1.7 and 2.4 V in CV measurements.[184,185] Lower reduction potentials of 0.69 and 0.05 V *versus* Li^+/Li for LiPON and LLZO, respectively, indicate their higher interfacial stability with the lithium anode than LLTO and LATP. It should be noted that the experimentally measured stability windows are much wider than that predicted by theory. For example, the LLZO SSE can be stable with lithium over 5 V, and this significantly large stability window is explained in terms of kinetic stability.[136,186] The formation of stable interphases may act as passivated SEIs to prevent further reaction of lithium with LLZO, similar to the role of SEIs in liquid electrolytes.[67,187–191] A similar extended stability window for kinetic reasons was reported in NASICON-type and sulfide SSEs.[137]

4.3.1.2. Experiments probing interfacial reactions. It was recently found that SSLMBs with NASICON and sulfide SSEs failed due to increasing polarization.[170,192] As reported by Wu *et al.*, short circuiting was observed in LLZO based SSLMBs after several cycles (Fig. 12b) due to lithium dendrite penetration. In contrast, LATP based SSLMBs terminated after the continuously increasing polarization for 60 h without short circuit, suggesting an internal disconnection of the cell (Fig. 12c).[170] Increasing internal resistance caused by the thickening interphase layer due to the continuously chemical or electrochemical reactions between the lithium anode and the SSEs is suggested to be the culprit for the cell failure. Similar failure mechanisms were also observed in SSLMBs with perovskite LLTO and sulfide SSEs besides NASICON-type SSEs.[182,193–195]

Considering the reactive and conductive natures of the *in situ* formed interphase layers between lithium and SSEs, the Li/SSE interfaces can be distinguished into three types (Fig. 12d–f):[182] thermodynamically stable interfaces (Fig. 12d), thermodynamically unstable interfaces (Fig. 12e), and the last containing kinetically unstable ones and stable ones (Fig. 12f). Few prevalent SSEs exhibit thermodynamic stability because the reduction potentials of most SSEs are higher than 0 V *vs.* Li^+/Li. Based on the composition phase diagram, non-metal elements sulfur, phosphorus, nitrogen, oxygen and halides in the SSEs are finally reduced to Li_2S, Li_3P, Li_3N, Li_2O and lithium halides, respectively, which are stable for contacting with the lithium anode. First principles calculations[136,137,183] indicate that the reduction potential is 0 V for these lithium compounds. Computations and experiments suggest that the *in situ* formation of these stable lithium compounds can efficiently passivate and protect the lithium anode, acting as the SEI layer to stabilize the lithium anode, similar to the SEI layer on the lithium anode in liquid electrolyte.[137] These stable SEI passivation layers in the SSLMBs exhibit high ionic conductivity but electronic insulation, which prevent further reaction between lithium and the SSEs (Fig. 12f).[182] For example, the final products Li_2S and Li_3P for LPS[31,193] endow these sulfide SSEs with kinetically interfacial stability with lithium anodes. LiPON and anti-perovskite Li_3OCl SSEs also show similar kinetically interfacial stability with the lithium anode due to the formation of a stable SEI passivation layer of the Li_3P, Li_2O, Li_3N or LiCl phase.[196–198]

By contrast, the elements germanium and titanium in LLTO, LATP, $Li_{1+x}Al_xGe_{2-x}(PO_4)_3$ (LAGP) and LGPS are reduced to the corresponding metals or lithium alloys, which causes the continuous thickening of the unstable interphase layers between the lithium anode and the SSEs due to the mixed conductive characteristics of the interphase layer.[199] Due to the mixed conductivity for both ions and electrons of this mixed conducting interphase (MCI) layer,[199] the interfacial reactions proceed continuously in the SSEs, causing interfacial instability (Fig. 12e).[182] Indeed, Li_2S, Li_3P and Li–Ge alloy were detected in the interphase layer when LGPS contacted with the lithium anode.[194] The formation of the interphase layer in the Li/LGPS interface dramatically increases the interfacial resistance.[194] Li–Sn and Li–Si alloys formed in the Li/$Li_{10}SnP_2S_{12}$ and Li/$Li_{10}SiP_2S_{12}$ interfaces cause similar interfacial instability to the Li/LGPS interface.[200]

Similarly, due to the reduction of Ti^{4+} and Ge^{4+} to Ti^{2+} and Ge^{2+} and even metallic Ti and Li–Ge alloys in perovskite type SSEs such as LLTO[182] and NASICON type SSEs such as LATP and LAGP,[201] MCI layers were also formed in the Li/SSE interfaces,[199] as revealed by *in situ* and *ex situ* XPS. Due to the continuous reactions and unstable interfaces, interfacial engineering on the lithium anode such as incorporating artificial SEIs or protective layers is required when these unstable SSEs were used in SSLMBs to obtain kinetically stable interfaces and to improve the cycle performance of the batteries.

Among all the SSEs examined, garnet LLZO shows the lowest reduction potential of 0.05 V.[136,183,202] The low reduction potential and small decomposition energy suggest that LLZO may be kinetically stabilized to lithium metal, which is supported by the experimental results showing no reduction at 0 V in the CV experiment[203] of a Li/LLZO/Li cell. However, reaction of garnet LLZO with lithium metal was observed at elevated temperatures. Cracks were present in LLZO when it was immersed in molten lithium, while no cracks were observed in the pristine sample.[204] Below 0.05 V, LLZO was lithiated and reduced to Li_2O, Zr_3O, and La_2O_3, and Zr_3O even further reduced to Zr metal below 0.004 V.[136] The chemical reaction

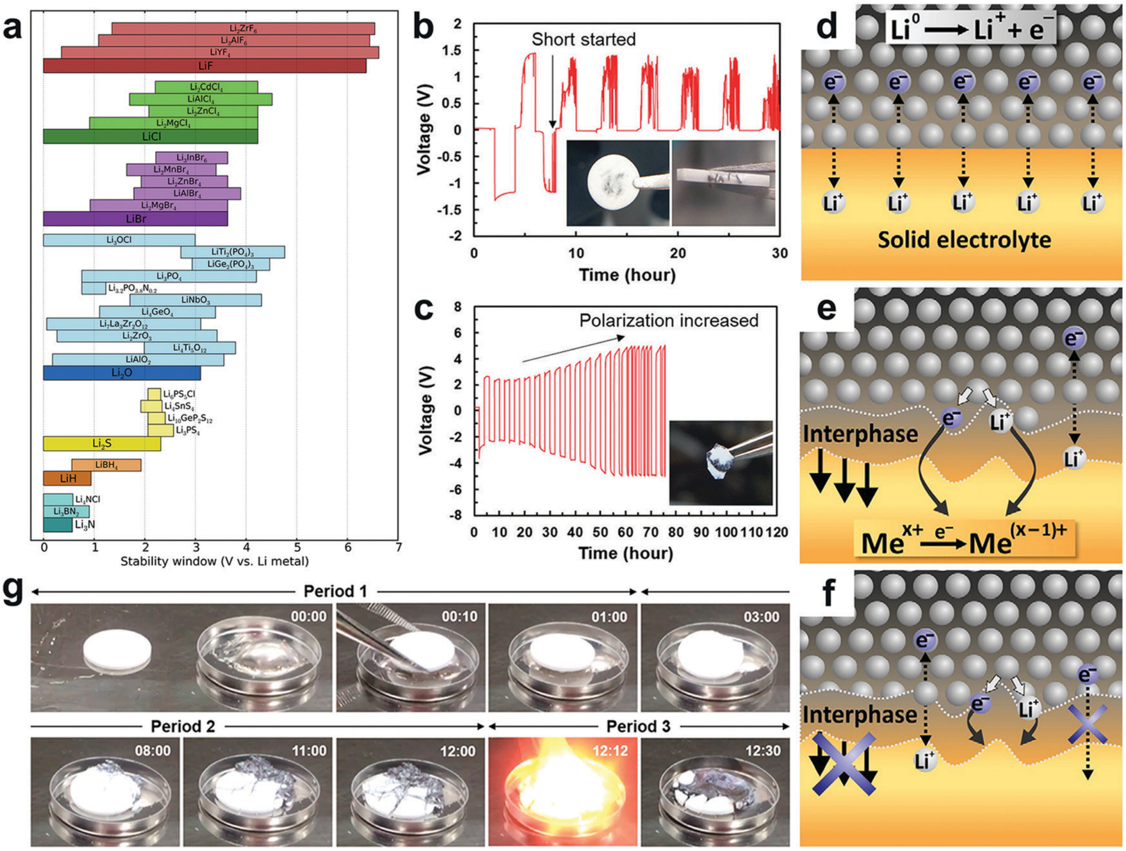

Fig. 12 Interfacial stability of Li/SSEs. (a) Electrochemical stability ranges of various electrolyte materials grouped by anion, with the corresponding binaries for comparison. The high-voltage stability of these materials is determined primarily by the anion. (Reproduced with permission.[137] Copyright 2016 American Chemical Society.) (b and c) Cyclic performance of (b) Li/LLZO/Li and (c) Li/LATP/Li symmetric cells at room temperature with a 0.1 mA cm^{-2} current density. Inset: Digital photographs of (b) the surface and cross section of the cycled LLZO and (c) the surface of the cycled LATP. (Reproduced with permission.[170] Copyright the Royal Society of Chemistry 2018.) (d–f) Three types of interfaces between lithium metal and the SSE. (d) Non-reactive and thermodynamically stable interface; (e) reactive and unstable MCI; and (f) reactive and metastable SEI. (Reproduced with permission.[182] Copyright 2015 Elsevier B.V.) (g) Sequential photographs of the contact between a sintered LAGP pellet and melted lithium metal at 200 °C in a glovebox (H_2O and O_2 levels of <0.1 ppm). The time is expressed as minutes : seconds. (Reproduced with permission.[192] Copyright 2017 American Chemical Society.)

between lithium and LLZO was investigated *via in situ* TEM by Ma *et al.*[205] They found that once the LLZO was brought into contact with the Li-metal electrode, a tetragonal-like LLZO interphase with a thickness of 5 unit cells formed and inhibited further chemical reaction between lithium and LLZO.[205] Tao *et al.* also conducted an *in situ* TEM study on the Li/LLZO interfacial reaction but drew a different conclusion.[206] They observed that during lithium plating into the Li/LLZO interface, LLZO remained unchanged, revealing the superior stability of LLZO to lithium.[206,207]

4.3.1.3. Lithium reactions with SSEs at high temperatures and thermal runaway. The highly reactive metallic lithium can even trigger the thermal runaway of SSLMBs at high temperatures where lithium contacts with LATP, LAGP and LLTO.[192,208] Chen *et al.* suggested that oxygen generation from SSEs at elevated temperatures was responsible for the thermal runaway of SSEs with the highly reactive lithium. By comparing the onset temperature and the heat-generation rate of different material systems, the thermal stability *versus* lithium of the four SSEs was identified to follow the order of LAGP < LATP < LLTO < LLZO. Chung and Kang observed that the chemically formed interphase between molten lithium and LAGP above 200 °C induces a rigorous chemical reaction, leading to a thermal runaway (Fig. 12g).[192] The thermal runaway indicates potential safety issues in SSLMBs induced by rigorous chemical reactions between metallic lithium and oxygen released from SSEs at increased temperatures. These results suggest that the notion that SSLMBs are safer than liquid electrolyte based lithium-ion or metal batteries is questionable.

In summary, the thermodynamic stability windows of most SSEs are narrow, but the experimentally observed stability windows are much wider than that predicted by theory. The discrepancy is explained in terms of kinetic stability; namely, interfacial reactions may generate stable interphases which act as SEIs to prevent further reactions between lithium and the SSEs. However, if the interphases are unstable, the kinetic stability fails. Lithium reacts with SSEs at high temperatures violently, causing thermal runaway.

4.3.2. Failure mechanisms of Li/NASICON and Li/sulfide interfaces in terms of electro-chemo-mechanics

4.3.2.1. Failure mechanisms of Li/NASICON interfaces. If the interphases formed at the Li/SSE interface are unstable and MIEC in nature, the interfacial reaction is sustainable, leading to the continuous thickening of the interphases and an increase of the interfacial mechanical stress, causing cracks and fracture of the SSEs, which in turn increase the interfacial resistance and polarization, leading to eventually failure of SSLMBs. As reported by Hartmann *et al.*, after only 1 h in contact with lithium metal, the total resistance of the symmetric LAGP and $Li_{1+x-y}Al_xTa_yGe_{2-x-y}(PO_4)_3$ (LATGP) cells increased to about 21 and 81 kΩ cm^2, respectively, and then quickly increased to ~72 kΩ cm^2 after 42 h and ~200 kΩ cm^2 after 90 h (Fig. 13a), respectively.[199] The continuous increase of resistance was ascribed to the thickening of the MCI induced by the reduction of Ti^{4+} (Fig. 13b), which increased the interfacial stress and induced cracks, fracture and even detachment of the SSE.[199] The resistance of the symmetric LAGP cell even continuously increased for 50 days due to the continuous reaction between lithium and LAGP.[192]

Unstable interphase formation causes large volume change at the interface, and thus induces mechanical failure of the SSE, which triggers the dysfunction of SSLMBs. Local volume expansion induced stress is the main factor in causing the mechanical failure. When the NASICON-type SSE contacted with lithium, the chemical reactions occurred and a new MCI formed (Fig. 13c), which nucleated and grew inhomogeneously at the interface (Fig. 13d). The interphase pervaded into both lithium and LAGP layers with a glacier-like morphology (Fig. 13e). The interphase consisted of many particles with sizes similar to those of LAGP particles. However, the particles in the interphase were rougher and more rounded than the LAGP particles (Fig. 13f). The newly formed non-uniform interphases induced inhomogeneous volume expansion which increased local internal stress in the interphase layer and the electrolyte, triggering the nucleation of cracks and fracture of the SSE (Fig. 13g–i). *In situ* X-ray computed tomography (CT) visualized the continuous formation of cracks with the continuous lithium deposition in a LAGP based SSLMB and confirmed that the volume expansion induced fracture of the LAGP SSE was the primary factor causing the resistance increase rather than the resistance of the interphase itself (Fig. 13g–i).[209] The reaction of lithium with LAGP caused amorphization and volume expansion of the interphase, which induced mechanical stress and fracture of the SSE along with a massive increase in interfacial resistance. Similar amorphization, volume expansion and fracture were observed in LATP SSE.[210]

Local reactivity heterogeneity between lithium and the SSE due to the non-uniform chemistry of the SSE surface including compositions and grain boundaries is another factor in generating mechanical instability of the Li/SSE interface. Wu *et al.* found that the reactions between LATP and lithium efficiently terminated the continuous lithium dendrite propagation, which was considered as a key factor in preventing the formation of lithium dendrites, but the reaction region expanded and eventually blocked the Li^+ ion transport, and finally the cell terminated by substantially increased resistance.[170] He *et al.* also investigated the failure mechanism of a LAGP based SSLMB and found that the chemical reactions between LAGP and molten lithium started from the grain boundaries, and then resulted in a change in the grain size of LAGP from 1 μm to 100 nm.[201] The composition of the grains changed with the degree of reaction for one refined particle and some grains lost their contact with LAGP after a heavy reaction due to the fast reaction along the grain boundaries. Finally, some of Ge^{4+} near the grain boundaries and surfaces were reduced to Ge^0 and even formed the Li–Ge alloy.[201]

In summary, the Li/NASICON interface is chemically/electrochemically unstable due to the mismatch of chemical potential between lithium and NASICON, leading to interfacial reactions and the interphase formation. The formation of interphases causes volume expansion and mechanical stress at the interface, which trigger cracking and fracture of the NASICON SSE, and eventually failure of SSLMBs.

4.3.2.2. Failure mechanisms of Li/sulfide interfaces. Volume expansion induced cracks accompanied by a continuous increase of interfacial resistances were also observed in SSLMBs with LGPS, $Li_{10}SiP_2S_{12}$ and $Li_{10}SnP_2S_{12}$ SSEs,[211,212] similar to SSLMBs with LATP and LAGP SSEs. Similar to the Li/NASICON interface, chemical reactions between lithium and the sulfide SSEs cause volume expansion due to the formation of interphases. The non-uniform reactions form inhomogeneous interphases and volume expansion, which induce local stress and cracks in the sulfide SSEs. The increased interphase layer with poor ionic conductivity and the formation of cracks increase the interfacial resistance of the Li/SSE interfaces. A continuous increase in impedance over time at open circuit and the formation of surface cracks were observed when LGPS contacted with lithium.[212] The increase of the Li/LGPS interfacial resistance was faster than that of the Li/$Li_7P_3S_{11}$ (LPS) interface. The thickness increase rate of the interphase layer in the Li/LGPS interface was 10 times faster than that of the Li/LPS interface. The faster interfacial reaction kinetics for the Li/LGPS interface was ascribed to the formation of Li–Ge alloy or a metallic Ge phase in the interphase layer with a higher electronic conductivity.[194] Han *et al.* investigated the effect of electronic conductivity on the interfacial stability of Li/LGPS and Li/LLZO interfaces.[213,214] They found that the stable electrochemical window became narrower when conductive carbon was added into these SSEs,[213,214] confirming the detrimental effect of electronic conductivity on the Li/SSE interfacial stability.[214]

By contrast, due to the formation of electronically insulating but thermodynamically stable interphases such as Li_2S, Li_3P and lithium halides, ceramic LPS,[31,215] argyrodite-type LPS-Cl[81] and halides doped sulfide glass SSEs[105,216] are kinetically stable with the lithium anode. However, these kinetically stable interfaces suffer from a similar lithium dendrite penetration problem to the Li/LLZO interface. For instance, the electrochemically deposited lithium metal in LPS propagated in a cellular manner, along pore channels, grain boundaries, or both, and then caused the short circuit of the battery.[36] The void formation in the Li/LPS-Cl interface in the stripping process was considered as a dominant factor in the formation of lithium dendrites during the plating process.[81] The accumulated voids

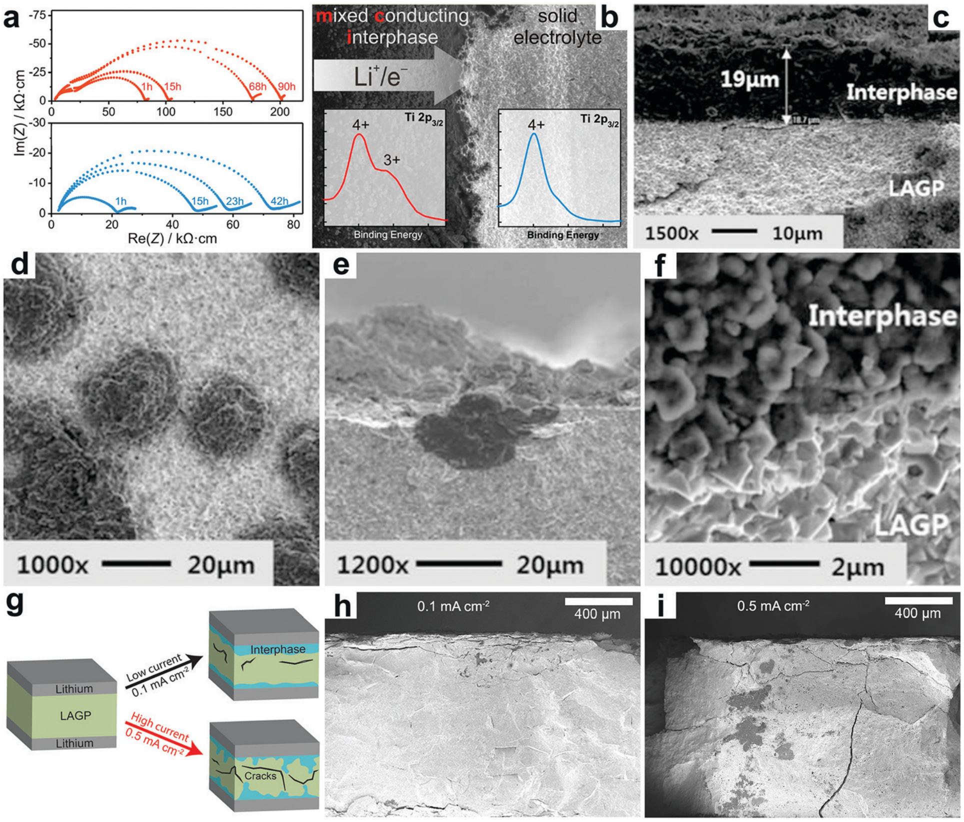

Fig. 13 Mechanical and electrochemical stability between lithium and inorganic SSEs. (a) Impedance spectra of (top) LATGP and (bottom) LAGP samples with lithium electrodes at room temperature (approximately 20 °C) in an Ar-filled glovebox. (Reproduced with permission.[199] Copyright 2013 American Chemical Society.) (b) Schematic for the degradation of LATP when it contacts with lithium and the formation of a MCI. (Reproduced with permission.[199] Copyright 2013 American Chemical Society.) (c) Cross-sectional SEM image of a Li/LAGP interphase layer formed after detaching a Li metal foil. (Reproduced with permission.[192] Copyright 2017 American Chemical Society.) (d) SEM image and (e) and (f) cross-sectional SEM images of the Li/LAGP interface after detaching lithium metal foil with the nucleation of the interphase. (Reproduced with permission.[192] Copyright 2017 American Chemical Society.) (g) Schematic for the mechanical degradation of LAGP during the charge–discharge process. (Reproduced with permission.[209] Copyright 2019 American Chemical Society.) (h and i) Low-magnification cross-sectional SEM images of LAGP cycled until failure at (h) 0.1 mA cm^{-2} and (i) 0.5 mA cm^{-2}. (Reproduced with permission.[209] Copyright 2019 American Chemical Society.)

during the stripping/plating cycles caused poor contact between Li and the SSE and increased the local current density, and the so-called current focusing ''hot spots'' induced dendrite formation when the apparent average current density was still lower than the CCD. The formation and expansion of voids as well as the lithium propagation during the plating/stripping cycle were visualized by Seitzman *et al.* using synchrotron-based X-ray tomography in a LPS based SSLMB.[82]

In summary, there are two distinct failure mechanisms in NASICON and sulfide SSE based SSLMBs: one is the unstable interphase formation which thickens continuously due to their MIEC nature and increases the interfacial impedance, and the other is the volume changes that arise from the interphase formation, causing cracks and fracture of the SSEs and mechanical failure of the SSLMBs.

4.3.3. Strategies for stabilization of Li/NASICON and Li/sulfide interfaces. Many efforts have been devoted towards engineering the interfaces between lithium and SSEs to improve the interfacial stability and the cycle performance of SSLMBs *via* the introduction of polymer or inorganic interlayers, and *in situ* construction of stable SEI layers and metallic buffer/protective layers.

4.3.3.1. Polymer protective layers. Wang *et al.* coated a thin PEO (LiTFSI) layer on the surface of lithium to avoid direct contact between lithium and LAGP SSE.[217] The reduction potential for Li^+ efficiently decreased after the PEO (LiTFSI) layer modification, and lithium dendrite growth was efficiently suppressed. Interface engineering by adding a LiCl containing thin thermosetting polymer, P(AA-*co*-MA)Li, layer, was conducted on the surface of a bare LAGP pellet before contacting with lithium to improve the stability of the interface.[201] Zhou *et al.* reported a polymer/LATP/polymer electrolyte based on cross-linked poly(ethylene glycol) methyl ether acrylate and achieved dendrite-free lithium deposition.[218] Jin *et al.* introduced a multifunctional nanoparticle-reinforced CPE layer in the LATP/Li interface to not only avoid side reaction but also reduce interfacial resistance.[219] Zhang *et al.* coated a PEO-based solid polymer electrolyte (SPE) of PEO–75% Li_2S–24% P_2S_5–1% P_2O_5 (LPOS) on a LAGP pellet to prevent the direct contact between lithium and LAGP.[220] The sticky PEO thin layer was used as an interfacial adhesive to link the compact LATP ceramic electrolyte and the lithium anode, and the interfacial resistance decreased from 2478 to 242 Ω cm^2.[221] A wetted polypropylene (PP) layer was introduced into the interface between LAGP and lithium, which successfully prevented the undesirable reactions.[222] The interfacial resistance of the SSLMB decreased from 421 to 51 Ω cm^2 after the introduction of the PP layer. A disparate-polymer protected LATP SSE, in which the anti-oxidative polyacrylonitrile (PAN) and the anti-reductive PEO were introduced into the SSE/cathode and SSE/anode interfaces to improve both their interfacial stabilities, respectively (Fig. 14a and b). The CV curve (Fig. 14c) exhibited a wide electrochemical window of the protected SSE, indicating the improvements of the interfacial stability of the Li/LATP interface.[223]

4.3.3.2. Artificial inorganic SEI layers. Artificial SEI films are widely used to improve the interfacial stability of Li/NASICON interfaces. In comparison with bare LATP, the ALD Al_2O_3-coated LATP exhibits a more stable cycling behavior with smaller voltage hysteresis for 600 h and a smaller interfacial resistance (Fig. 14d and e). Characterization *via* high-resolution TEM and electron energy loss spectroscopy (EELS) indicated that lithium penetration and Ti^{4+} reduction are significantly limited due to the Al_2O_3-coating layer.[224] Bai *et al.* doped ZnO *via* a surface coating method by magnetron sputtering to improve the stability of the LATP electrolyte to the attack of the lithium metal anode and to avoid the growth of lithium dendrites.[225] Wang *et al.* introduced a LiPON layer with a thickness of 500 nm between lithium and a LAGP–PEO composite SSE to provide a uniform Li^+ flux and suppress the lithium dendrites.[226] Jadhav *et al.* reported a LiPON thin film deposited on B_2O_3-added lithium aluminum germanium phosphate (B-LAGP) by the RF-sputtering technique to mitigate the reaction between lithium and B-LAGP.[227]

Artificial SEI films on the lithium anode are also efficient strategies to improve the interfacial compatibility between the lithium anode and sulfide SSEs.[212,228] As reported by Sang *et al.*,[228] the lithiated Al_2O_3 ($LiAlO_x$) interlayer functions to decrease the potential between lithium and LPS and suppress the LPS decomposition. However, Wang *et al.* found that the $LiAlO_x$ protective layer only offered finite interfacial stability due to the high stiffness of the $LiAlO_x$, which could not accommodate the lithium plating/stripping induced large stress/strain.[229] For this reason, they constructed an inorganic–organic hybrid interlayer (alucone) *via* molecular layer deposition (MLD) to improve the Li/LGPS interfacial stability. Davis *et al.* directly deposited a 20 nm Al_2O_3 layer on LGPS to investigate the impact of the Al_2O_3 artificial SEI on the interfacial stability between lithium and LGPS.[212] They also found finite interfacial stability and the Al_2O_3 artificial SEI just delayed the cell degradation; a lithium dendrite was observed when the crack was present in the lithiated Al_2O_3 artificial SEI layer.

4.3.3.3. In situ construction of stable SEIs. Since the reduction of Ti^{4+} and Ge^{4+} to form Ti^0 and Ge^0 is the main reason for the formation of the MCI layer, substituting the Ti^{4+}/Ge^{4+} with another element to *in situ* form a stable SEI is another strategy to obtain a stable interface between the lithium anode and NASION type SSE. Li *et al.* substituted Ti^{4+}/Ge^{4+} with Zr^{4+} to obtain a $LiZr_2(PO_4)_3$ electrolyte, which reacted with a metallic lithium anode to form a Li^+-conducting SEI layer containing Li_3P and Li_8ZrO_6 *in situ*.[230] The SEI passivation layer exhibited good wettability with both lithium and the $LiZr_2(PO_4)_3$ electrolyte, and thus improved the interfacial compatibility. Liu *et al.* reported using a plastic superconductive layer to protect the reaction between lithium and LAGP by *in situ* modifying the succinonitrile (SN)-based plastic interlayer with LLZAO nanowires (l-SN), which stabilized the interface, improved the interfacial stability and suppressed the lithium dendrites.[231]

Although sulfide SSEs have a limited thermodynamic electrochemical stability window around 1.7–2.1 V, the Li/sulfide SSE interface is kinetically stable due to the formation of interphases with high ionic conductivity and low electronic conductivity.[136,137,183] The *in situ* formation of interphases by tuning the composition of the SSE is considered as an efficient strategy to stabilize the Li/sulfide SSE interface. Fan *et al.* introduced a LiF-rich thin film *in situ* to suppress the lithium dendrite growth and block the side reaction between lithium and LPS SSE (Fig. 14f).[232] The CCD was increased from 0.7 mA cm^{-2} to 2.0 mA cm^{-2} (Fig. 14g and h), and the coulombic efficiency of the lithium plating/deposition increased from 88% of the pristine LPS to more than 98% for the LiF-coated LPS. Zhang *et al.* constructed an *in situ* formed LiH_2PO_4 protective layer to circumvent the chemical instability between lithium and LGPS SSE.[233] The Li/sulfide SSE interfacial stability as well as lithium dendrite suppression can be achieved by the incorporation of LiI into the electrolyte to *in situ* form a stable SEI film due to the high ionic conductivity and electronic insulation of LiI.[105,234] A high CCD of 3.9 mA cm^{-2} was achieved by using a 30 mol% LiI containing Li_2S–P_2S_5 glass SSE.[105] A new iodide-based phase, $Li_7P_2S_8I$, formed by the reaction of LiI with LPS at 200 °C, exhibited remarkable compatibility with the metallic lithium anode.[235] The Li/$Li_7P_2S_8I$/Li cell with the iodide-based $Li_7P_2S_8I$ SSE could be cycled 800 times, indicating the excellent lithium plating/stripping cycle life.

4.3.3.4. Metallic buffer layers. Thin metallic layers, such as Ge, Al and Cr,[236–238] are successfully used as the protective layers. An amorphous Ge thin film was sputtered on a LAGP surface, which not only suppressed the reduction reaction of Ge^{4+} with lithium, but also produced an intimate contact between lithium and the LAGP SSE (Fig. 14i–k).[236] Before Ge film coating, Ge^{4+} in the LAGP pellet would be reduced to Ge^{2+} and Ge^0 upon contacting with lithium; after sputtering the Ge film between LAGP and the lithium anode, Ge^{4+} was protected and remained stable after cycling (Fig. 14i and j). The cycle performance of a Li/Ge/LAGP/Ge/Li symmetric cell was better

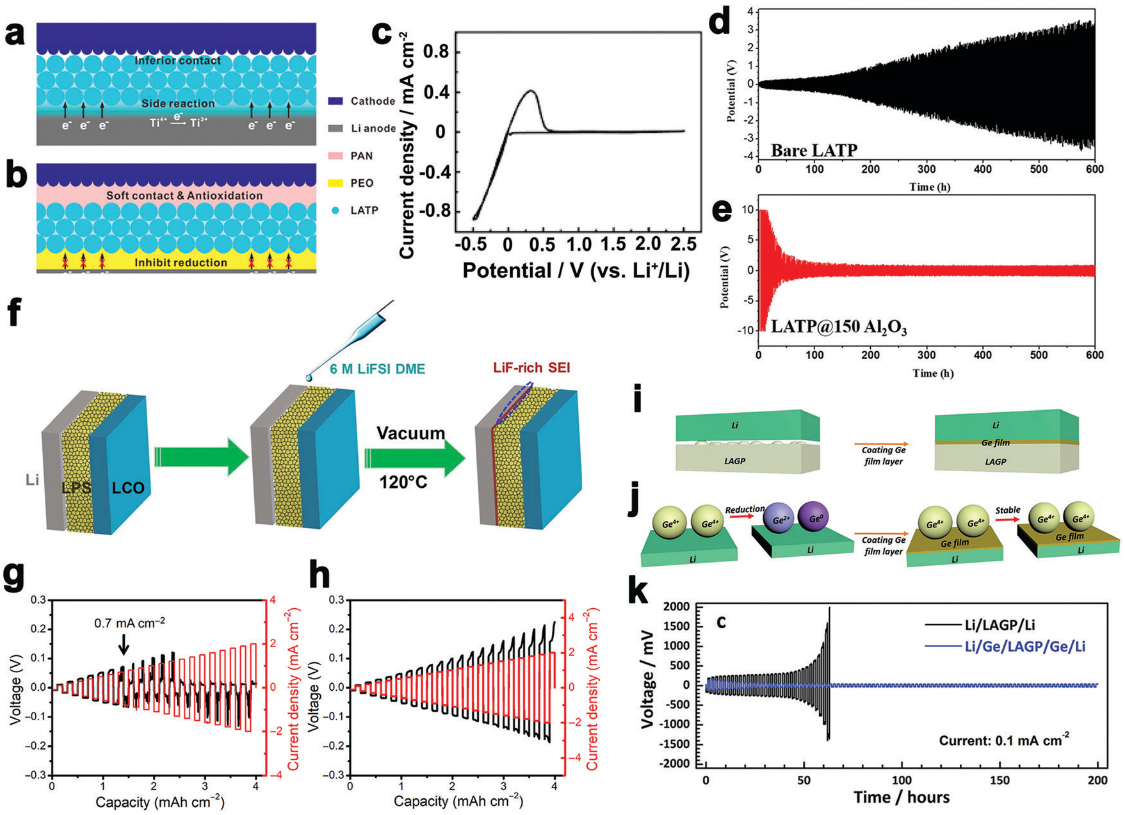

Fig. 14 Strategies for stabilization of Li/NASICON and Li/sulfide interfaces. (a and b) Illustrations of the solid full battery with (a) pristine LATP and (b) disparate-polymer protected SSE, in which anti-oxidative polyacrylonitrile (PAN) and anti-reductive PEO were introduced into the SSE/cathode and SSE/anode interfaces, respectively. (Reproduced with permission.[223] Copyright 2019 American Chemical Society.) (c) Cyclic voltammetry curve of the disparate-polymer protected SSE at 60 °C. (Reproduced with permission.[223] Copyright 2019 American Chemical Society.) (d and e) Cycling behavior of the Li/LATP/Li symmetrical cell without (d) and with (e) Al_2O_3 interlayer coatings at a current density of 0.01 mA cm^{-2}. (Reproduced with permission.[224] Copyright 2018 American Chemical Society.) (f) Schematic illustration of the pretreated processes for the formation of a LiF-rich SEI layer between the lithium metal and the LPS SSEs. (Reproduced with permission.[232] Copyright 2018 The Authors, some rights reserved; exclusive licensee American Association for the Advancement of Science.) (g and h) Galvanostatic lithium plating/stripping profiles in the Li/LPS/Li cell (g) and the Li/LiFSI@LPS/Li cell (h) at step-increased current densities. (Reproduced with permission.[232] Copyright 2018 The Authors, some rights reserved; exclusive licensee American Association for the Advancement of Science.) (i and j) Schematic diagrams of the amorphous Ge film coating between LAGP SSE and lithium metal to improve the Li/LAGP interfacial stability. (Reproduced with permission.[236] Copyright 2018 Wiley-VCH Verlag GmbH & Co. KGaA, Weinheim.) (k) Cycling performance of the Li/Ge/LAGP/Ge/Li and Li/LAGP/Li symmetric cells at a current density of 0.1 mA cm^{-2}. (Reproduced with permission.[236] Copyright 2018 Wiley-VCH Verlag GmbH & Co. KGaA, Weinheim.)

than that of a Li/LAGP/Li cell (Fig. 14k). A Li–Al alloy layer formed when the Al foil was assembled on the lithium–boron alloy anode, which reduced the side reaction between the lithium alloy anode and the NASICON SSE.[237] Cortes *et al.* investigated the reasons for the protective effect of a fine Cr metallic coating layer on the LAGP *via* sputtering.[238] They claimed that uniform metallic layers improved the initial physical contacts between lithium and LAGP. Moreover, the lithiated alloy interphase converted the lithium plating/stripping into the conversion reaction, promoting the reversible electrochemistry during the charge/discharge process.

A Au thin buffer layer was inserted into the Li/LPS interface by Kato *et al.* to prevent void formation after the initial lithium dissolution and increase the sites for lithium deposition, which efficiently reduced the interfacial resistance and enhanced the interfacial stability.[31] Li–In alloy electrodes have been widely used as the stable anodes in SSLMBs due to their high interfacial stability with sulfide SSEs than the pure lithium anode.[239–241] Nagao *et al.* reported that inserting a Li–In alloy thin layer at the interface between the lithium electrode and the sulfide SSE brought about a good cyclability and a high rate capability in SSLMBs because of the formation and retention of intimate contacts at the interface.[240]

In summary, the introduction of interlayers can form a stable SEI, improve the wettability, alleviate the deleterious interfacial reactions between lithium and NASICON or sulfide SSEs, thus improving the performance of SSLMBs. However, some of the introduced interlayers can only delay the interface degradation but cannot prevent it, as these interlayers suffer from similar chemical/electrochemical and electro-chemo-mechanical degradation to the SSEs. Therefore, carefully choosing the appropriate interlayers and controlling SEIs are critical to optimizing the performance of the Li/NASICON and Li/sulfide interfaces.

4.4. Electro-chemo-mechanics of Li/PEO interfaces

The electro-chemo-mechanics of Li/PEO interfaces plays important roles in the lithium dendrite suppression, interfacial resistance and cycling life of PEO based SSLMBs. From a pure mechanical perspective, the Monroe and Newman criterion[34] suggests that when the elastic modulus of the PEO is two times greater than that of lithium, dendrite growth is suppressed (a detailed discussion on this topic is presented in Section 3.2). However, lithium dendrites and cell failures were still observed when reinforced PEO SSEs[126,127] or stiff inorganic SSEs[155] with elastic moduli far greater than two times that of lithium were used in SSLMBs. Therefore, the Li/PEO interface stability and dendrite suppression are dictated by the electrochemical/chemical and mechanical coupling effects, meaning that in addition to the mechanical suppression strategy, chemical/electrochemical properties such as the high ionic conductivity, high lithium ion transference number, low resistance and low reactivity with lithium are also critical to the Li/PEO interface stability. Inorganic fillers, copolymer based PEO electrolytes and multilayer-structured PEO based composite electrolytes have been used to efficiently improve both the mechanical and electrochemical/chemical stability of the Li/PEO interfaces, which are reviewed in this section.

Interfaces with low resistance and fast ion transfer are also required to achieve the electrochemical stability of Li/PEO interfaces. However, as lithium metal is an active alkali metal, the as-received metallic lithium is inevitably composed of Li_2CO_3, LiOH and Li_2O in the surface layer,[242] which form the initial passivation film. Lithium also reacts with PEO to form a passivation layer between lithium and PEO[243–248] and the reaction is suggested to be similar to that in liquid electrolyte.[249] The reaction between lithium and liquid electrolyte forms a passivation layer on the surface of lithium called a SEI, which has been studied extensively;[67,134,187,188,190,250] however, the passivation layer in the Li/PEO interface was less well characterized; thus the reaction mechanisms between lithium and PEO are not well understood. Nevertheless, it is well recognized that lithium reacts not only with the salts in PEO but also with the backbones of PEO itself, forming a passivation layer between lithium and PEO, whose structure and composition are not well understood. For example, Fauteux proposed that LiF was formed in the passivation layer due to the reaction between lithium and the F-containing salt in the PEO electrolyte complexed with lithium triflate ($LiSO_3CF_3$) salt.[251] However, Vincent *et al.* argued that lithium sulfite and CF_3 radicals were the reaction products in the passivation layer due to the weaker C–S bonds as compared to the C–F bonds.[245] Xu *et al.* suggested that LiOH was formed in the passivation layer and the LiOH amount was determined by the water content in the polymer SSE.[252] Metallic lithium can even be directly dissolved in PEO, which was detected by the ^7Li NMR technique in a recent study by Galluzzo *et al.*[253] Therefore, more fundamental understanding of the nature of the SEI in the Li/PEO interface and interface engineering is required to obtain a stable Li/PEO interface with both enhanced mechanical properties and high ionic conductivity.

4.4.1. Inorganic fillers for improving the stability of Li/PEO interfaces. Inorganic additives have been widely used to improve both the mechanical and electrochemical stability of Li/PEO interfaces. Kalnaus *et al.* calculated the effective Young's modulus of PEO electrolyte with additives to identify appropriate composite structures that could block lithium dendrites.[254] Both inert fillers such as Al_2O_3,[255] TiO_2,[255] and SiO_2[115,256] and Li^+ conductive particles LLZO[257] and LATP[258] were used as the inorganic fillers to improve the mechanical properties and ionic conductivity of PEO electrolytes. Lin *et al.* introduced a stiff mesoporous SiO_2 aerogel backbone into a polymer-based electrolyte to achieve a high modulus of $\sim$0.43 GPa and a high ionic conductivity of 0.6 mS cm^{-2}, which efficiently suppressed lithium dendrites.[115] Zhang *et al.* dispersed LLZO nanoparticles into isolated PEO to obtain reinforced CPEs with high ionic conductivity, which suppressed lithium dendrites due to their enhanced mechanical properties and high ionic conductivity.[257] They also found that nanoscale LLZO particle filled PEO electrolytes exhibited higher ionic conductivity than microscale particle filled electrolytes because of their higher specific surface area and percolation effect.[257]

Borghini *et al.* studied the electrochemical properties of PEO based electrolytes, with and without the addition of dispersed γ-$LiAlO_2$ powder as a filler. The results clearly indicated that the use of the γ-$LiAlO_2$ ceramic filler combined with the $Li[(CF_3SO_2)_2N]$ salt greatly reduced the crystallization rate and enhanced the lithium/electrolyte interface stability.[259] Li *et al.* reported the effect of various ceramic fillers with PEO electrolyte. They found that the interfacial resistance largely depended on the properties of the added fillers. Specifically, a small amount of ferroelectric $BaTiO_3$ added into PEO improved the interface stability and lithium ion conductivity regardless of the lithium salt species.[122] Shin *et al.* studied the size effect of nano silica and micro γ-$LiAlO_2$ fillers on the electrochemical and interfacial properties of PEO–$LiN(SO_2CF_2CF_3)_2$ electrolyte using linear sweep voltammetry, alternating current impedance and galvanostatic stripping/deposition on symmetric non-blocking cells. They found that the presence of silica caused high interfacial resistances during storage under open circuit at 90 °C. Meanwhile, they observed a negative effect in that the silica containing polymer electrolytes showed the highest initial overpotential and an unstable behavior of the interface. These results suggest that the addition of nano silica into PEO electrolyte has a detrimental effect on the electrochemical and interfacial stability. By comparing the electrochemical properties of PEO with micro γ-$LiAlO_2$, they claimed that the favorable effect of inert fillers was only observed in polymer electrolytes most likely due to the presence of residual solvents or moisture trapped on the surface particles that were released into the polymer electrolyte,[260] which is not consistent with other reports.[122,259]

4.4.2. Structure modification of PEO for the electro-chemomechanics of Li/PEO interfaces. Structure modifications such as copolymerization[261,262] and blending[116,263] have been widely used to improve the mechanical properties of the substrate for PEO based SSEs. Chintapalli *et al.* utilized the SEO mixed with LiTFSI salt as the polymer electrolyte to harness the advantage of both the polystyrene block which provides mechanical stiffness and the PEO block that solvates and transports ions derived from LiTFSI. Wu *et al.* constructed a double network gel electrolyte blending polyvinylidene difluoride–hexafluoropropylene (PVDF–HFP) and PEO to integrate high ionic conductivity and high mechanical toughness.[116] The obtained electrolyte has a high modulus of 44.3 MPa and a high fracture energy of 69.5 $kJ\ m^{-2}$ as well as a high conductivity of 0.81 $mS\ cm^{-1}$ at 30 °C. Transparent flexible lithium ion conducting solid polymer electrolyte polydimethylsiloxane (PDMS), PEO and $LiClO_4$ exhibited high mechanical robustness and flexibility (Young's modulus $\sim$1 MPa) with an ionic conductivity of $\sim$0.03 $mS\ cm^{-1}$. The high mechanical properties and ionic conductivity enabled SSLMBs with these SSEs to exhibit high battery performances.[263]

4.4.3. Effect of the salt species on the formation of interlayers between lithium and PEO. While coupling PEO with different lithium salts, the ionic species play an important role in the interlayer formation in the Li/PEO interface. Ismail *et al.* studied lithium metal electrodes before and after contact with PEO electrolyte containing $LiN(SO_2CF_3)_2$ (LiTFSI) or $LiBF_4$.[242] They found that due to the adsorption of TFSI anions and/or the formation of polymeric forms of the anion, a thin and stable interface with less resistance seemed to be established. While in contact with the $LiBF_4$ containing PEO, a thick interfacial layer composed of LiF was formed.[242] Granvalet-Mancin *et al.* investigated the formation of a passivation layer between lithium metal and PEO electrolytes with lithium triflate ($LiSO_3CF_3$) salt *via* attenuated total reflection FTIR spectroscopy, AFM and electrochemical impedance spectroscopy.[243] They found that the first reaction for the formation of a passivation layer was the formation of the CF_3 radical, which quickly extracted a hydrogen from the polymer backbone, and somewhat later lithium broke the C–O bonds in the polymer backbone resulting in the formation of Li–O–R type compounds.[243] They suggested that many of the end groups resulting from these reactions were of the form CH_3–CH_2–. The formation of a passivation layer was found to increase the interfacial resistance, which is detrimental to Li/PEO interfaces; thus its formation should be mitigated. By introducing self-assembled molecular layers (semicrystalline wax from Petrolite Specialty Polymers, denoted as $H–(CH_2)_{32}–(CH_2–CH_2–O–)_{10}–H$) on the polymer electrolyte surface, the above passivation reactions were prevented. Fauteux studied the formation of a passivation layer in the Li/PEO interface at elevated temperatures, and evaluated the reaction between lithium and PEO with four lithium salts ($LiCF_3SO_3$, $LiAsF_6$, $LiClO_4$, and LiI).[249] For the $LiCF_3SO_3$ and $LiAsF_6$ salts, a LiF based SEI was formed as the passivation layer as a result of the reaction between lithium metal and the F-containing groups in the lithium salt. Li_2O and LiOH were formed in the passivation film for all four PEO electrolytes with different lithium salts, which might be attributed to the reaction between the trace amount of water in the electrolytes and the lithium anode. The results showed that the passivation layer formation occurred under open circuit conditions, implying chemical reaction between the lithium anode and PEO electrolyte. The nature of the salt in PEO and the chemical potential of the ionic species influence the kinetics of the passivation layer formation and growth.[249]

4.4.4. Effect of solvent on the electro-chemo-mechanics of Li/PEO interfaces. Solvents including organic carbonates, ethers and ionic liquids have been widely used as plasticizers to obtain gel polymer electrolytes (GPEs), which exhibit comparable ionic conductivity to liquid electrolyte. However, GPEs generally suffer from poor mechanical properties and low electrochemical stability due to the introduction of organic solvents. Incorporating inorganic additives, polymer blending,[264] constructing multilayered structures[265] and grafting branched structures[266] have been used to improve the mechanical properties and electrochemical stability of GPEs. The Young's modulus increased from 0 for LiTFSI–SN to a maximum $\sim$1.0 MPa by tuning the ratios of the blended SN, polyacrylonitrile and PEO.[264] A sandwich structure polymer/polymer-ceramic/polymer gel electrolyte composed of PVDF/LLTO–PEO/PVDF was constructed to suppress lithium dendrites by combining the advantages of inorganic and gel-type polymer electrolytes.[265] Chusid *et al.* reported *in situ* FTIR studies of lithium interactions with two polymer electrolytes: one was a PVDF–HFP with cyclic alkyl carbonates as plasticizers, suitable for ambient temperatures; and the other was a solvent free polymer, a derivative of PEO with a branched structure: poly[ethyleneoxide-2-(2-methoxyethoxy)ethyl glycidyl ether], suitable for elevated temperatures.[266] They found that the surface chemistry of lithium electrodes in contact with the former was dominated by alkyl carbonate solvent reduction to $ROCO_2Li$ surface species. In the latter, the surface reactions of lithium electrodes were dominated by salt and trace water reduction, with the surface species being $Li_2S_2O_4$, $Li_2NSO_2CF_3$, *etc.* The polymer itself seemed to be stable with lithium even at 60 °C.

4.4.5. Artificial interlayers. In order to minimize the reaction between lithium and PEO electrolyte, interlayers are introduced to enhance interfacial stability. Brown *et al.* positioned a diblock copolymer (PE-*b*-PEO) having a general chemical formula of $H–(CH_2)_{32}–(O\text{-}CH_2CH_2)_{10}–OH$ at the PEO electrolyte surface. The PE-*b*-PEO interlayer robustly adhered to the lithium, which resulted in an interfacial resistance three orders of magnitude lower than that of standard PEO.[267] Mason *et al.* investigated the self-assembled monolayer $H–(CH_2)_{32}–(CH_2–CH_2–O)_{10}–H$ modified Li/PEO interface; they found that samples with the monolayer developed interfacial passivation more slowly than the untreated PEO in contact with lithium. They asserted that the monolayer could be used to deter the formation of an interfacial barrier film.[268]

4.4.6. Interface stability between lithium and poly(propylene carbonate) (PPC) electrolyte. Wang *et al.* studied the degradation of PPC induced by a chemical reaction with lithium or the trace LiOH on the surface.[269] Initially fragmentation of the polymer PPC into lithium carbonate (I) and a polymeric primary radical or PPC fragmentation terminated with the hydroxy group occurred. The existence of LiOH accelerated the production of the intermediate (I). Then the intermediate (I) produced lithium alkoxide (II) by decarboxylation along with the generation of a lithium carbon dioxide radical. Next intermediate II tended to fragment into lithium alkoxide (III) and small molecule PC when there was no presence of cellulose in the system. The evolution from II to III generated a PC infiltrated interface. Furthemore, the authors used cellulose as a scaffold to restrain electrolyte and lithium reaction in the interface region, thus preventing further reaction of lithium with internal PPC. The interfacial reaction caused swelling of PPC, leading to a better physical contact between lithium and the polymer electrolyte, thus decreasing the interfacial resistance. The authors demonstrated that the cycling of a symmetrical Li/Li cell using bare PPC based SSE was inferior to that of a cell using cellulose confined PPC. They suggested that the *in situ* self-wetting process provides a new pathway for improving the interfacial compatibility and ionic conductivity of solid state batteries.

In summary, the electro-chemo-mechanics determines the chemical/electrochemical stability, interfacial stress and impedance of the Li/PEO interfaces. Introducing organic fillers or non-ion conducting nanoparticles enhances both the mechanical and ionic properties of the PEO SSEs, thus improving the dendrite suppression capability and reducing the interfacial impedance. Introducing interlayers, different salts and solvents in the PEO electrolyte can alter the structure and composition of the SEI in the Li/PEO interfaces, thus impacting the performance of the SSLMBs. The nature of the SEI in the Li/PEO interfaces is not well understood and calls for further investigations.

4.5. Characterization tools for lithium dendrites and interfacial evolutions

To suppress dendrite growth and optimize Li/SSE interfaces, it is critical to develop state-of-the-art characterization tools to understand the genesis of lithium dendrite growth and deleterious interphase formation. Unfortunately, the lithium dendrite growth and the interphase formation are buried in the Li/SSE interfaces or in the bulky SSEs, rendering them difficult to directly characterize. Another practical challenge that constrains the dendrite and interface characterization arises from the extreme reactivity of lithium metal and the SSEs with oxygen, moisture, and organic species,[270] making sample preparation and transfer extremely difficult. Nevertheless, many achievements have been made in the *in situ* and *operando* technologies for the characterization of the lithium stripping/plating process and Li/SSE interface evolutions, although more efforts should be devoted to these areas in future studies.[271]

In situ environmental transmission electron microscopy (ETEM) is an emerging technique to study the nucleation and propagation of lithium/sodium dendrites, and quantify the mechanical properties such as the yield strength and Young's modulus of lithium and sodium dendrites.[66,68,272] In a gaseous ambient such as CO_2, the surfaces of the freshly grown lithium or sodium dendrites are covered with thin layers of Li_2CO_3 or Na_2CO_3 with thicknesses generally less than about 20 nm, respectively, mimicking the formation of SEI layers on the lithium surface in liquid electrolyte based LIBs. The surface Li_2CO_3 or Na_2CO_3 layers protect the lithium or sodium dendrites from electron beam damage, thus enabling *in situ* dendrite growth and mechanical property characterization, which are not possible in a conventional high vacuum TEM. With an appropriate setup, it is even possible to investigate the electro-chemo-mechanics of lithium by *in situ* ETEM. Zhang *et al.*[66] and He *et al.*[68] developed an *in situ* AFM-ETEM platform to observe lithium dendrite growth and its stress generation (Fig. 4a). They found that lithium dendrites (whiskers) exhibit much higher yield strength than bulk lithium. Zhang *et al.* were able to measure the mechanical stress generation of a growing lithium dendrite under different applied voltages, and they found that the stress generated by a growing lithium dendrite can reach 130 MPa.

Cryogenic TEM is an emerging technique to image beam sensitive alkali metals such as lithium (Fig. 15a). HRTEM images of lithium dendrites[273–275] and SEIs,[273,276] and EELS mapping of SEIs[276] have been realized. There is no doubt that this technique can be extended to the studies of lithium dendrites and interfaces in SSLMBs.

In situ SEM imaging has been widely used for the investigation of the lithium dendrite nucleation and growth in polymer based SSLMBs[111,112,123,277,278] and sulfide glass SSE based SSLMBs.[103] These observations are usually restricted to the Li/SSE surface; information regarding the buried interface is still missing. Broadly used in the lithium dendrite investigations of liquid electrolyte based LIBs,[279] *in situ* optical microscopy has been making great strides in characterizing the dendrite

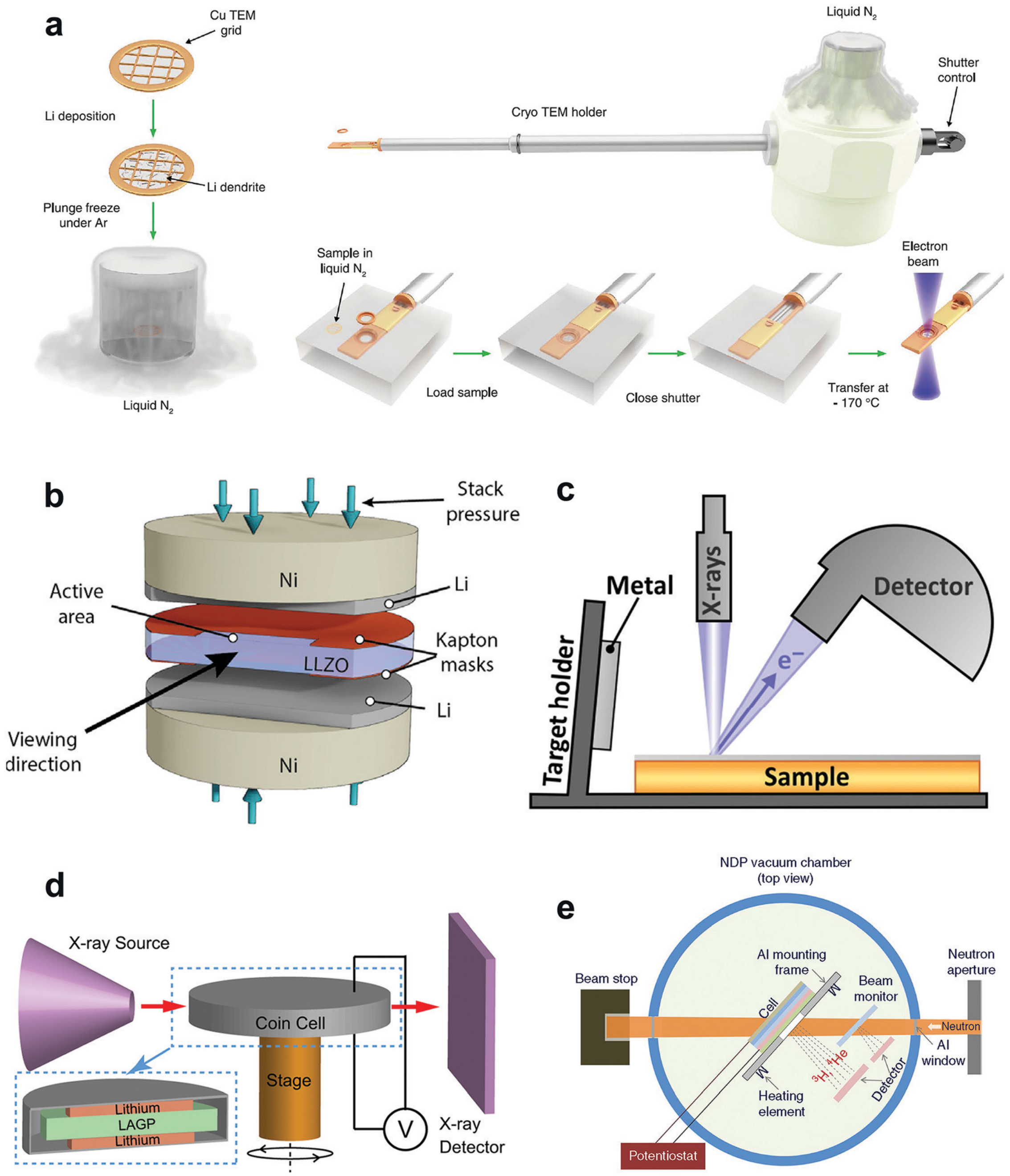

Fig. 15 Advanced characterization for lithium dendrites and Li/SSE interfaces. Schematics of (a) cryo-TEM measurement for lithium dendrites and SEI films (Reproduced with permission.[273] Copyright 2017 The Authors, some rights reserved; exclusive licensee American Association for the Advancement of Science), (b) *Operando* optical microscopy for lithium deposition (Reproduced with permission.[83] Copyright 2020 The Author(s). Published by Elsevier Inc.), (c) *In situ* XPS measurements for Li/SSE interfaces (Reproduced with permission.[182] Copyright 2015 Elsevier B.V.), (d) *In situ* X-ray CT for lithium deposition and Li/SSE interfacial evolution (Reproduced with permission.[283] Copyright 2019 American Chemical Society) and (e) NDP for lithium distribution (Reproduced with permission.[40] Copyright 2019 Springer Nature).

growth and the lithium penetration mechanisms in SSEs recently.[83,93,145,212,280,281] Kazyak *et al.* probed the coupled electro-chemo-mechanics of Li/LLZO interfaces by *operando* optical microscopy (Fig. 15b).[83] Quantitative analysis of synchronized electrochemistry with *operando* video microscopy revealed new insights into the nature of lithium propagation in SSEs. The authors observed lithium dendrite propagation from one electrode to the other, which is perhaps the clearest evidence so far that dendrites indeed penetrated through LLZO and caused a short circuit. They suggested that a singular mechanism is insufficient to describe the complexity of lithium propagation pathways. Krauskopf *et al.* probed again by *operando* optical microscopy that lithium deposition can generate large stress, breaking up the copper film current collector.[93] Similar phenomena have been reported by Motoyama *et al.*[91] and Citrin *et al.*[43] in LiPON SSE. They showed that surface flaws like surface ledges and grain boundaries are preferable locations for lithium nucleation. Good and maintained contact with a pre-existing reservoir of lithium metal or an alloy layer with fast lithium-diffusion properties on the anode side is suggested to be highly beneficial for the assembly of SSLMBs with a planar anode geometry employing crystalline inorganic SSE separators. SSLMBs without a (thin) lithium-metal reservoir in the as-assembled state will have greater issues with short circuiting.

The advantages of *operando* optical microscopy and SEM are at least two fold: firstly, they provide a global overview of the dendrite growth and interface evolution; and secondly, because the samples are large, these techniques permit electrochemistry and microstructural evolution correlations. The disadvantage is that their resolution is limited, as the detailed structures and compositions of the nucleation sites and the interfacial reaction products are not available. In this context, *in situ* TEM complements the cons of *operando* optical microscopy and SEM; however, *in situ* TEM lacks the big picture, and the electrochemistry is usually missing or not sufficient due to the small sample size in the restricted space in the TEM sample holders. Therefore a combination of *operando* optical microscopy, SEM and *in situ* TEM can cover the cross-length scale from the nanometer to millimeter range, providing a full picture of the lithium dendrite and interface problems in SSLMBs.

In situ XPS is an efficient technology to detect the composition and phase evolutions of the interface between lithium and SSEs as well as the *in situ* formed SEI (Fig. 15c).[182,194] Combined with AC impedance measurements, the *in situ* XPS revealed effectively the failure mechanism and stability of the Li/SSE interfaces. Synchrotron or *in situ* X-ray CT offers a powerful technique to image the lithium dendrite formation and propagation as well as the failure mechanisms of SSEs in SSLMBs (Fig. 15d).[282,283] *Operando* X-ray imaging was used to visualize the lithium dendrite growth.[284] The *in situ* CT imaging technique is not destructive and provides three-dimensional images of the interphases between the lithium anode and SSEs during the charge/discharge process. The cracks and pores and their evolutions can be clearly observed *via* this technique.[282,283] *In situ* Auger electron spectroscopy/microscopy (AES/AEM) techniques under ultrahigh vacuum combined with *in situ* SEM were used by Kim *et al.* to investigate the lithium stripping and plating in sulfide SSE based SSLMBs.[104] They found that lithium migration to the lithium metal anode was strongly dependent on the pressure applied to the sample during the charge/discharge cycles. At the sample position under excessively high local pressure, a large amount of lithium metal migrated to the anode, and irreversible growth of lithium metal was observed.

Due to the sensitivity of neutrons to light elements such as Li, B, and Na, NDP, as a non-destructive neutron analytical technique, has been widely used to detect the Li distribution and transport in SSLMBs. Han *et al.* investigated the dynamic evolution of the lithium concentration profiles in the LLZO, LPS, and LiPON SSEs (Fig. 15e).[40] Based on this advanced characterization, they suggested that high electronic conductivity is probably the root cause for the dendrite formation in SSEs.[40] Wang *et al.* used the *in situ* NDP to reveal the interfacial behavior of garnet SSE in contact with metallic Li during the plating and stripping processes.[133] They found that a 3D mixed electron–ion conductive framework was preferred as a Li metal host to decrease the amount of "dead" Li and overcome the large volume change. Li *et al.* found a similar phenomenon in the investigation of the Li/LLZTO interface *via in situ* NDP measurement.[285] The NDP technique was also used in the investigations of the lithium plating and stripping processes in liquid electrolyte based LMBs.[286,287] ^{7}Li NMR is a very powerful technique to study not only the chemical environment changes of lithium or lithium ions but also microstructural changes such as the formation of lithium dendrites or mossy lithium, and chemo-mechanical fracture of Li/SSE interfaces.[288,289] ^{7}Li NMR chemical shift imaging and electron microscopy were used by Marbella *et al.* to track lithium microstructural growth in the garnet-type SSE $Li_{6.5}La_3Zr_{1.5}Ta_{0.5}O_{12}$.[290] They followed the early stages of lithium microstructural growth during galvanostatic cycling, from the formation of lithium on the electrode surface to dendritic lithium connecting both electrodes in symmetrical cells, *via* this technique, and correlated these changes with alterations observed in the voltage profiles during cycling and impedance measurements. The advantage of NMR over SEM and TEM is that the former can provide quantitative information but the latter can only provide qualitative information.

5. Challenges and perspectives

The mechanical properties of lithium depend strongly on the length scale. Submicron sized lithium whiskers possess mechanical strength over 100 times higher than that of bulk lithium, twenty times higher than that of lithium spheres with diameters of a few microns to tens of microns, two times higher than that of lithium pillars with diameters ranging from 1 to 10 μm. The length scale of lithium dendrites in SSLMBs is usually in the range of a few hundred nanometers to less than 10 μm. Therefore the electro-chemo-mechanical properties of lithium dendrites need to be considered in the context of this strong size effect. Due to the size effect of lithium, controlling the morphology of the deposited lithium would be an efficient strategy to suppress lithium penetration into the SSEs. Uniform lithium deposition avoiding the formation of local nanosized lithium *via* interface engineering is critical to reduce the interfacial stress and suppress lithium dendrites. Artificial interlayers, pre-deposited lithium, surface modifications of lithium deposition substrates and so on are considered as the valid techniques to achieve uniform lithium deposition.

Furthermore, the dendrites in SSLMBs are usually covered with a surface SEI layer, and this surface layer has a strong influence on the mechanical properties of the dendrites. But quantitative investigations on the surface SEI layer effect on the mechanical properties of dendrites are lacking. Moreover, currently there is virtually no mechanical property investigation on thin films of Li_2O, Li_2CO_3, and LiOH with thicknesses of a few tens of nanometers, a length scale related to the SEI layer thickness.

The overpotential driven lithium dendrite growth and propagation can generate large stress in media such as SSEs; namely, a 100 mV overpotential can generate 750 MPa stress, which is much higher than the mechanical strengths of lithium whiskers and bulk lithium. This overpotential driven lithium growth generated stress is essential to the propagation of lithium in SSEs. In this case, lithium behaves as an incompressible fluid which flows like a viscous liquid.[79] It should be noted that most lithium creep experiments are conducted under very low stress, say close to the yield strength of bulk lithium, which is about 1 MPa; however, the flowing behavior of lithium in SSLMBs is usually driven under much higher stress of a few hundred MPa. Whether the experimental results obtained from the creep property measurements of lithium under low stress can be extrapolated to understand the flowing behavior of lithium under high stress is unknown. Furthermore, conventional creep experiments are conducted in tensile mode, but the propagation of lithium in SSEs is driven by compressive stress. It is questionable whether the tensile properties of lithium can be translated to the understanding of the compressive properties is uncertain and this warrants further investigations.

Regardless of the SSEs used, lithium dendrites tend to penetrate the SSEs at high current density or under high overpotential. In the case of LLZO, the CCD has increased to 1 mA cm^{-2}.[83,102,152,291,292] However, further increasing the CCD is hampered by the lack of fundamental understanding of the dendrite nucleation and propagation mechanisms; understanding and circumventing this grand challenge is critical to the development of SSLMBs for real applications.

Significant progress has been made towards understanding of the dendrite nucleation and propagation mechanisms,[36,38–40,83,138,282] but many unanswered questions remain. For example, where is the initial nucleation site of a dendrite? How does a dendrite propagate in the SSE? Cheng *et al.* observed lithium propagation along grain boundaries.[38] Porz *et al.* suggested that lithium propagates along cracks driven by the overpotential.[36] They later found that lithium can penetrate even single crystal LLZO, indicating that another propagation mechanism is operating. Han *et al.* suggested that lithium nucleates randomly inside the SSEs where the electronic conductivity is high, and then grows until the randomly nucleated lithium connects each other, forming a current path, thus causing a short circuit.[40] Song *et al.* suggested that the grain boundaries in LLCZN have higher electronic conductivity than the bulk; thus grain boundaries are the preferred nucleation sites for lithium, which then grows until they form a conducting network, thus causing a short circuit of SSLMBs.[293] Apparently we are still far away from a thorough understanding of the lithium nucleation and propagation mechanisms in SSEs. Ideal SSEs with suitable mechanical properties, homogeneous composition, high ionic conductivity and perfect electronic insulation would be the perpetually right pursuit for the development of SSLMBs.

Another critical issue in SSLMBs is the interface.[135] Theoretical modeling indicates that most SSEs are thermodynamically unstable towards lithium, as such interfacial reaction takes place at the Li/SSE interfaces, forming interphases. The formation of chemo-mechanics of the interphase has profound effects on the SSEs. Firstly, the formation of interphases causes large volume changes that generate large stress at the interface, which may fracture the SSE directly and cause the mechanical failure of SSLMBs. Secondly, the interphase may be electronically insulating and ionically conducting, or MIEC, and in the latter case, the interphase formation is sustainable, causing rapid electro-chemo-mechanical degradation of the SSEs. Applying a Li-alloying interlayer can delay the interfacial degradation due to the alloying reaction between lithium and the interlayer; however, the integrity of the interlayer degrades as well during battery cycling due to electro-chemo-mechanical stress. Most of the alloying interlayer experiences large volume changes, which introduce additional stress to the interface; consequently, stress induced mechanical degradation, such as fracture, void formation and pulverization, is expected. For example, voids and pulverization were directly observed by *in situ* TEM in Ge and Al nanowire electrodes during cycling. Therefore, one needs to be very careful in choosing the appropriate interlayers with long cycle lifetimes to boost the performance of SSLMBs.

In the same principle of using alloying interlayers to prevent the direct contact between lithium and SSEs, thus mitigating deleterious interfacial reaction, lithium alloy electrodes may be more stable in contact with SSEs due to their higher potentials compared to the Li/Li$^+$ redox couple. Alloy electrodes may face the same challenges as alloying interlayers: such as void formation and pulverization of the electrode after long cycles. Nevertheless, the interfacial reaction mechanisms and degradation mechanisms of alloy electrodes have not been well understood to date. Better interface engineering coupling the mechanics, chemistry and electrochemistry of lithium and SSEs or completely concept breakthroughs of Li/SSE interface science may provide a new perspective to obtain stable interfaces.

Combining SSEs such as LLZO with polymer electrolytes is another strategy to improve the physical contact between lithium and the electrolyte. The so-called ''ceramic-in-polymer'' or ''polymer-in-ceramic'' electrolyte combines the advantage of the high ionic conductivity of the LLZO ceramic with the flexibility of the polymer, and thus may enable large scale SSLMB manufacture.[294] However, the mixed electrolytes bring new problems; for example, the interface between the ceramic and the polymer may have huge impedance due to the presence of a space charge layer. The ion conduction mechanisms in the mixed SSEs are not well understood. Furthermore, the lithium dendrite penetration mechanism in the mixed SSEs and the interfacial reaction between lithium and the mixed SSEs are not explored.

With regard to the lithium anode, the dynamic morphological evolution of lithium deposition and stripping during cycling is unclear. What are the structural and morphological characteristics of the "hot spots" where lithium dendrites grow? How does "dead" lithium form in SSLMBs? These are unexplored areas in SSLMBs. Answering these questions may provide critical science to enable the lithium anode in SSLMBs.

"Dead" lithium consists of diverse lithium compounds within SEIs, such as LiF, Li_2CO_3, Li_2O, $ROCO_2Li$, and unreactive metallic lithium which is electrically isolated. The formation mechanism and quantification of "dead" lithium have been investigated in liquid organic electrolyte based LMBs.[131,132,295] The "dead" lithium in the SEI increases continuously with increased plating/stripping cycles due to the continuous formation and accumulation of SEIs. The metallic "dead" lithium was often derived from the preferred stripping from the root rather than the tip of the lithium dendrite.[132] In contrast to the large amount of work published on "dead" lithium in liquid electrolyte based LMBs, few research studies about "dead" lithium in SSLMBs were reported, possibly due to the buried interfaces in SSLMBs, rendering *in situ* observation difficult. The formation of "dead" lithium often causes the capacity loss and volume expansion of the lithium anode, which deteriorate the performance of LMBs. Strategies such as using suitable external stack pressure and improved wettability, reducing the interfacial resistance, thus rendering uniform lithium deposition/stripping, may be adopted. "Dead" lithium in SSLMBs remains an unexplored area, and more research work is needed in this area.

Finally, emerging characterization tools such as cryo-electron microscopy and ETEM are advancing rapidly in the characterization of lithium dendrites and SEIs. Cryo-electron microscopy and ETEM have great potential in probing the challenging issues in SSLMBs such as dendrites, SEIs, "dead" lithium and interface reactions, and facilitating the development of SSLMBs.

Abbreviations

AES/AEM	Auger electron spectroscopy/microscopy
AFM	Atomic force microscopy
AFM-ETEM	Atomic force microscopy-environmental transmission electron microscopy
ALD	Atomic layer deposition
bcc	Body-centered-cubic
B-LAGP	B_2O_3-Added lithium aluminum germanium phosphate
CCD	Critical current density
CF_x	Carbon monofluoride
CPE	Composite polymer electrolyte
CT	Computed tomography
CV	Cyclic voltammetry
ETEM	Environmental transmission electron microscopy
fcc	Face-centered-cubic
GPE	Gel polymer electrolyte
LAGP	$Li_{1+x}Al_xGe_{2-x}(PO_4)_3$
LLZAO	Al-Substituted LLZO
LALZWO	$Li_{5.9}Al_{0.2}La_3Zr_{1.75}W_{0.25}O_{12}$
LATP	$Li_{1+x}Al_xTi_{2-x}(PO_4)_3$
LATGP	$Li_{1+x-y}Al_xTa_yGe_{2-x-y}(PO_4)_3$
LGPS	$Li_{10}GeP_2S_{12}$
LIBs	Lithium ion batteries
LiPON	Lithium phosphorous oxynitride
LLCZN	$Li_{6.85}La_{2.9}Ca_{0.1}Zr_{1.75}Nb_{0.25}O_{12}$
LLTO	$Li_{0.33}La_{0.57}TiO_3$
LLZO	$Li_7La_3Zr_2O_{12}$
LLZTO	$Li_{7-x}La_3Zr_{2-x}Ta_xO_{12}$
LMBs	Lithium metal batteries
LPS	Li_3PS_4
LPS-Cl	Li_6PS_5Cl
MCI	Mixed conducting interphase
MIEC	Mixed ionic–electronic conductor
MLD	Molecular layer deposition
NASICON	Na-Superionic conductor
NDP	Neutron depth profiling
PE	Polyethylene
PECVD	Plasma-enhanced chemical vapor deposition
PEO	Polyethylene oxide
PP	Polypropylene
PPC	Poly(propylene carbonate)
PVDF–HFP	Polyvinylidene difluoride–hexafluoropropylene
SEI	Solid electrolyte interface
SEM	Scanning electron microscope
SEO	Polystyrene-*block*-poly(ethylene oxide)
SHE	Standard hydrogen electrode
$SOCl_2$	Thionyl chloride
SPE	Solid polymer electrolyte
SSEs	Solid state electrolytes
SSLMBs	Solid state lithium metal batteries
TEM	Transmission electron microscopy
XPS	X-ray photoelectron spectroscopy

Conflicts of interest

There are no conflicts to declare.

Acknowledgements

This work was financially supported by the National Key Research and Development Program of China (No. 2018YFB0104300), the National Natural Science Foundation of China (No. 51772262, 21406191, 11575154, 51971245, 51802277, 52022088, U20A20336, 21935009, 52002346), the Fok Ying-Tong Education Foundation of China (No. 171064), the Natural Science Foundation of Hebei Province (No. B2018203297, B2020203037), the Hebei One Hundred Talent Program (No. 4570028), the Beijing Natural Science Foundation (2202046), the Beijing Natural Science Foundation of China-Haidian Special Project (No. L182065), the High-Level Talents Research Program of Yanshan University (No. 00500021502, 005000201) and the Hunan Innovation Team (2018RS3091).

References

1 M. Winter, B. Barnett and K. Xu, *Chem. Rev.*, 2018, **118**, 11433–11456.

2 S. Fletcher, *Bottled Lightning: Superbatteries, Electric Cars, and the New Lithium Economy*, Hill & Wang, New York, 1st edn, 2011.

3 W. T. Brande, *A Manual of Chemistry*, John Murray, London, England, 2nd edn, 1821, vol. 2, pp. 57–58.

4 R. Wu, Y. Yan, G. Wang, L. E. Murr, W. Han, Z. Zhang and M. Zhang, *Int. Mater. Rev.*, 2015, **60**, 65–100.

5 K. T. Venkateswara Rao, W. Yu and R. O. Ritchie, *Metall. Trans. A*, 1989, **20**, 485–497.

6 R. Wagner, N. Preschitschek, S. Passerini, J. Leker and M. Winter, *J. Appl. Electrochem.*, 2013, **43**, 481–496.

7 M. J. Root, in *Batteries for Sustainability: Selected Entries from the Encyclopedia of Sustainability Science and Technology*, ed. R. J. Brodd, Springer-Verlag, New York, 2013, ch. 11, pp. 359–392.

8 K. Brandt, *Solid State Ionics*, 1994, **69**, 173–183.

9 T. Placke, R. Kloepsch, S. Dühnen and M. Winter, *J. Solid State Electrochem.*, 2017, **21**, 1939–1964.

10 G. Zhong, H. Chen, X. Huang, H. Yue and C. Lu, *Front. Chem.*, 2018, **6**, 50.

11 M. S. Whittingham, *Science*, 1976, **192**, 1126–1127.

12 D. Fouchard and J. B. Taylor, *J. Power Sources*, 1987, **21**, 195–205.

13 K. Brandt and F. C. Laman, *J. Power Sources*, 1989, **25**, 265–276.

14 C. Julien, A. Mauger, A. Vijh and K. Zaghib, *Lithium Batteries: Science and Technology*, Springer International Publishing, Switzerland, 1st edn, 2016.

15 M. M. Thackeray, C. Wolverton and E. D. Isaacs, *Energy Environ. Sci.*, 2012, **5**, 7854–7863.

16 C. Robillard, presented in part at the IEEE Power Engineering Society General Meeting, San Francisco, CA, USA, 16–16 June, 2005.

17 P. Dan, E. Mengeritsky, D. Aurbach, I. Weissman and E. Zinigrad, *J. Power Sources*, 1997, **68**, 443–447.

18 D. Fouchard and L. Lechner, *Electrochim. Acta*, 1993, **38**, 1193–1198.

19 R. Juza and V. Wehle, *Naturwissenschaften*, 1965, **52**, 560.

20 M. Bagouin, D. Guérard and A. Hérold, *C. R. Seances Acad. Sci., Ser. C*, 1966, **262**, 557–559.

21 D. Guérard and A. Hérold, *C. R. Seances Acad. Sci., Ser. C*, 1972, **275**, 571–572.

22 D. Guérard and A. Hérold, *Carbon*, 1975, **13**, 337–345.

23 A. N. Dey and B. P. Sullivan, *J. Electrochem. Soc.*, 1970, **117**, 222–224.

24 M. Arakawa and J.-I. Yamaki, *J. Electroanal. Chem. Interfacial Electrochem.*, 1987, **219**, 273–280.

25 R. Fong, U. V. Sacken and J. R. Dahn, *J. Electrochem. Soc.*, 1990, **137**, 2009–2013.

26 J. O. Besenhard, *Carbon*, 1976, **14**, 111–115.

27 R. Yazami and P. Touzain, *J. Power Sources*, 1983, **9**, 365–371.

28 K. Mizushima, P. C. Jones, P. J. Wiseman and J. B. Goodenough, *Solid State Ionics*, 1981, **3–4**, 171–174.

29 A. Yoshino, *Angew. Chem., Int. Ed.*, 2012, **51**, 5798–5800.

30 K. Xu, *Chem. Rev.*, 2004, **104**, 4303–4418.

31 A. Kato, H. Kowada, M. Deguchi, C. Hotehama, A. Hayashi and M. Tatsumisago, *Solid State Ionics*, 2018, **322**, 1–4.

32 J. Lau, R. H. DeBlock, D. M. Butts, D. S. Ashby, C. S. Choi and B. S. Dunn, *Adv. Energy Mater.*, 2018, **8**, 1800933.

33 N. Kamaya, K. Homma, Y. Yamakawa, M. Hirayama, R. Kanno, M. Yonemura, T. Kamiyama, Y. Kato, S. Hama, K. Kawamoto and A. Mitsui, *Nat. Mater.*, 2011, **10**, 682–686.

34 C. Monroe and J. Newman, *J. Electrochem. Soc.*, 2005, **152**, A396–A404.

35 K. Kerman, A. Luntz, V. Viswanathan, Y.-M. Chiang and Z. Chen, *J. Electrochem. Soc.*, 2017, **164**, A1731–A1744.

36 L. Porz, T. Swamy, B. W. Sheldon, D. Rettenwander, T. Frömling, H. L. Thaman, S. Berendts, R. Uecker, W. C. Carter and Y.-M. Chiang, *Adv. Energy Mater.*, 2017, **7**, 1701003.

37 Y. Ren, Y. Shen, Y. Lin and C.-W. Nan, *Electrochem. Commun.*, 2015, **57**, 27–30.

38 E. J. Cheng, A. Sharafi and J. Sakamoto, *Electrochim. Acta*, 2017, **223**, 85–91.

39 T. Swamy, R. Park, B. W. Sheldon, D. Rettenwander, L. Porz, S. Berendts, R. Uecker, W. C. Carter and Y.-M. Chiang, *J. Electrochem. Soc.*, 2018, **165**, A3648–A3655.

40 F. Han, A. S. Westover, J. Yue, X. Fan, F. Wang, M. Chi, D. N. Leonard, N. J. Dudney, H. Wang and C. Wang, *Nat. Energy*, 2019, **4**, 187–196.

41 K. B. Hatzell, X. C. Chen, C. L. Cobb, N. P. Dasgupta, M. B. Dixit, L. E. Marbella, M. T. McDowell, P. P. Mukherjee, A. Verma, V. Viswanathan, A. S. Westover and W. G. Zeier, *ACS Energy Lett.*, 2020, **5**, 922–934.

42 J. A. Lewis, J. Tippens, F. J. Q. Cortes and M. T. McDowell, *Trends Chem.*, 2019, **1**, 845–857.

43 M. A. Citrin, H. Yang, S. K. Nieh, J. Berry, W. Gao, X. Pan, D. J. Srolovitz and J. R. Greer, *MRS Bull.*, 2020, **59**, 1–14.

44 P. Wang, W. Qu, W.-L. Song, H. Chen, R. Chen and D. Fang, *Adv. Funct. Mater.*, 2019, **29**, 1900950.

45 F. Zhang, Q.-A. Huang, Z. Tang, A. Li, Q. Shao, L. Zhang, X. Li and J. Zhang, *Nano Energy*, 2020, **70**, 104545.

46 G. Richter, K. Hillerich, D. S. Gianola, R. Mönig, O. Kraft and C. A. Volkert, *Nano Lett.*, 2009, **9**, 3048–3052.

47 T. Zhu and J. Li, *Prog. Mater. Sci.*, 2010, **55**, 710–757.

48 M. D. Uchic, D. M. Dimiduk, J. N. Florando and W. D. Nix, *Science*, 2004, **305**, 986–989.

49 D. Hull and H. M. Rosenberg, *Philos. Mag.*, 1959, **4**, 303–315.

50 C. S. Barrett, *J. Jpn. Inst. Met.*, 1955, **84**, 2483–2489.

51 I. Gorgas, P. Herke and G. Schoeck, *Phys. Status Solidi A*, 1981, **67**, 617–623.

52 C. S. Barrett, *Phys. Rev.*, 1947, **72**, 245.

53 C. S. Barrett, *Acta Crystallogr.*, 1956, **9**, 671–677.

54 W. Pichl and M. Krystian, *Phys. Status Solidi*, 1997, **160**, 373–383.

55 S. Tariq, K. Ammigan, P. Hurh, R. Schultz, P. Liu and J. Shang, presented in part at the Proceedings of the 2003 Particle Accelerator Conference, Portland, OR, USA, 12–16 May, 2003.

56 R. P. Schultz, *Lithium: Measurement of Young's Modulus and Yield Strength*, B. Fermi National Accelerator Lab., IL (US) Report FERMILAB-TM-2191, USDOE Office of Energy Research (ER) (US), United States, 2002.

57 W. LePage, Y. Chen, E. Kazyak, K.-H. Chen, A. Sanchez, A. Poli, E. Arruda, M. Thouless and N. Dasgupta, *J. Electrochem. Soc.*, 2019, **166**, A89–A97.

58 A. Masias, N. Felten, R. Garcia-Mendez, J. Wolfenstine and J. Sakamoto, *J. Mater. Sci.*, 2019, **54**, 2585–2600.

59 W. M. Robertson and D. J. Montgomery, *Phys. Rev.*, 1960, **117**, 440–442.

60 C. D. Fincher, D. Ojeda, Y. Zhang, G. M. Pharr and M. Pharr, *Acta Mater.*, 2020, **186**, 215–222.

61 E. G. Herbert, S. A. Hackney, V. Thole, N. J. Dudney and P. S. Phani, *J. Mater. Res.*, 2018, **33**, 1347–1360.

62 Y. Wang, D. Dang, M. Wang, X. Xiao and Y.-T. Cheng, *Appl. Phys. Lett.*, 2019, **115**, 043903.

63 S. Hori, K. Saito and T. Hasegawa, *J. Jpn. Inst. Light Met.*, 2000, **50**, 660–665.

64 C. Xu, Z. Ahmad, A. Aryanfar, V. Viswanathan and J. R. Greer, *Proc. Natl. Acad. Sci. U. S. A.*, 2017, **114**, 57–61.

65 T. Slotwinski and J. Trivisonno, *J. Phys. Chem. Solids*, 1969, **30**, 1276–1278.

66 L. Zhang, T. Yang, C. Du, Q. Liu, Y. Tang, J. Zhao, B. Wang, T. Chen, Y. Sun, P. Jia, H. Li, L. Geng, J. Chen, H. Ye, Z. Wang, Y. Li, H. Sun, X. Li, Q. Dai, Y. Tang, Q. Peng, T. Shen, S. Zhang, T. Zhu and J. Huang, *Nat. Nanotechnol.*, 2020, **15**, 94–98.

67 W. Xu, J. Wang, F. Ding, X. Chen, E. Nasybulin, Y. Zhang and J.-G. Zhang, *Energy Environ. Sci.*, 2014, **7**, 513–537.

68 Y. He, X. Ren, Y. Xu, M. H. Engelhard, X. Li, J. Xiao, J. Liu, J.-G. Zhang, W. Xu and C. Wang, *Nat. Nanotechnol.*, 2019, **14**, 1042–1047.

69 P. Bai, J. Guo, M. Wang, A. Kushima, L. Su, J. Li, F. R. Brushett and M. Z. Bazant, *Joule*, 2018, **2**, 2434–2449.

70 K.-N. Tu, in *Solder Joint Technology: Materials, Properties, and Reliability*, ed. R. Hull, J. R. M. Osgood, J. Parisi and H. Warlimont, Springer, New York, NY, 2007, vol. 117, pp. 153–181.

71 B. Z. Lee and D. N. Lee, *Acta Mater.*, 1998, **46**, 3701–3714.

72 K. Zeng and K. N. Tu, *Mater. Sci. Eng., R*, 2002, **38**, 55–105.

73 Y. Wang, J. E. Blendell and C. A. Handwerker, *J. Mater. Sci.*, 2014, **49**, 1099–1113.

74 M. W. Barsoum, E. N. Hoffman, R. D. Doherty, S. Gupta and A. Zavaliangos, *Phys. Rev. Lett.*, 2004, **93**, 206104.

75 J. R. Greer, W. C. Oliver and W. D. Nix, *Acta Mater.*, 2005, **53**, 1821–1830.

76 Z. W. Shan, R. K. Mishra, S. A. Syed Asif, O. L. Warren and A. M. Minor, *Nat. Mater.*, 2008, **7**, 115–119.

77 A. Yulaev, V. Oleshko, P. Haney, J. Liu, Y. Qi, A. A. Talin, M. S. Leite and A. Kolmakov, *Nano Lett.*, 2018, **18**, 1644–1650.

78 P. M. Sargent and M. F. Ashby, *Scr. Metall.*, 1984, **18**, 145–150.

79 Y. Chen, Z. Wang, X. Li, X. Yao, C. Wang, Y. Li, W. Xue, D. Yu, S. Y. Kim, F. Yang, A. Kushima, G. Zhang, H. Huang, N. Wu, Y.-W. Mai, J. B. Goodenough and J. Li, *Nature*, 2020, **578**, 251–255.

80 K.-H. Chen, K. N. Wood, E. Kazyak, W. S. LePage, A. L. Davis, A. J. Sanchez and N. P. Dasgupta, *J. Mater. Chem. A*, 2017, **5**, 11671–11681.

81 J. Kasemchainan, S. Zekoll, D. Spencer Jolly, Z. Ning, G. O. Hartley, J. Marrow and P. G. Bruce, *Nat. Mater.*, 2019, **18**, 1105–1111.

82 N. Seitzman, H. Guthrey, D. Sulas-Kern, H. Platt, M. Al-Jassim and S. Pylypenko, *J. Electrochem. Soc.*, 2018, **165**, A3732–A3737.

83 E. Kazyak, R. Garcia-Mendez, W. S. LePage, A. Sharafi, A. L. Davis, A. J. Sanchez, K.-H. Chen, C. Haslam, J. Sakamoto and N. P. Dasgupta, *Matter*, 2020, **2**, 1025–1048.

84 A. S. Westover, N. J. Dudney, R. L. Sacci and S. Kalnaus, *ACS Energy Lett.*, 2019, **4**, 651–655.

85 R. Koerver, W. Zhang, L. de Biasi, S. Schweidler, A. O. Kondrakov, S. Kolling, T. Brezesinski, P. Hartmann, W. G. Zeier and J. Janek, *Energy Environ. Sci.*, 2018, **11**, 2142–2158.

86 E. G. Herbert, W. E. Tenhaeff, N. J. Dudney and G. M. Pharr, *Thin Solid Films*, 2011, **520**, 413–418.

87 S. Yu, R. D. Schmidt, R. Garcia-Mendez, E. Herbert, N. J. Dudney, J. B. Wolfenstine, J. Sakamoto and D. J. Siegel, *Chem. Mater.*, 2016, **28**, 197–206.

88 J. Wolfenstine, H. Jo, Y.-H. Cho, I. N. David, P. Askeland, E. D. Case, H. Kim, H. Choe and J. Sakamoto, *Mater. Lett.*, 2013, **96**, 117–120.

89 J. E. Ni, E. D. Case, J. S. Sakamoto, E. Rangasamy and J. B. Wolfenstine, *J. Mater. Sci.*, 2012, **47**, 7978–7985.

90 S. Yu and D. J. Siegel, *ACS Appl. Mater. Interfaces*, 2018, **10**, 38151–38158.

91 M. Motoyama, M. Ejiri and Y. Iriyama, *Electrochemistry*, 2014, **82**, 364–368.

92 M. Motoyama, M. Ejiri and Y. Iriyama, *J. Electrochem. Soc.*, 2015, **162**, A7067–A7071.

93 T. Krauskopf, R. Dippel, H. Hartmann, K. Peppler, B. Mogwitz, F. H. Richter, W. G. Zeier and J. Janek, *Joule*, 2019, **3**, 2030–2049.

94 K. Yan, Z. Lu, H.-W. Lee, F. Xiong, P.-C. Hsu, Y. Li, J. Zhao, S. Chu and Y. Cui, *Nat. Energy*, 2016, **1**, 16010.

95 S. Narayan and L. Anand, *Extreme Mech. Lett.*, 2018, **24**, 21–29.

96 R. D. Armstrong, T. Dickinson and J. Turner, *Electrochim. Acta*, 1974, **19**, 187–192.

97 Y. M. Chiang, D. P. Birnie and W. D. Kingery, *Physical Ceramics: Principles for Ceramic Science and Engineering*, John Wiley & Sons, New York, 1997.

98 M. W. Barsoum, *Fundamentals of Ceramics*, The Mc Graw-Hill Companies Inc., New York, 1997.

99 J. Wolfenstine, J. L. Allen, J. Sakamoto, D. J. Siegel and H. Choe, *Ionics*, 2018, **24**, 1271–1276.

100 Z. Liu, W. Fu, E. A. Payzant, X. Yu, Z. Wu, N. J. Dudney, J. Kiggans, K. Hong, A. J. Rondinone and C. Liang, *J. Am. Chem. Soc.*, 2013, **135**, 975–978.

101 Y. Seino, T. Ota, K. Takada, A. Hayashi and M. Tatsumisago, *Energy Environ. Sci.*, 2014, **7**, 627–631.

102 R. Garcia-Mendez, F. Mizuno, R. Zhang, T. S. Arthur and J. Sakamoto, *Electrochim. Acta*, 2017, **237**, 144–151.

103 M. Nagao, A. Hayashi, M. Tatsumisago, T. Kanetsuku, T. Tsuda and S. Kuwabata, *Phys. Chem. Chem. Phys.*, 2013, **15**, 18600–18606.

104 S. H. Kim, K. Kim, H. Choi, D. Im, S. Heo and H. S. Choi, *J. Mater. Chem. A*, 2019, **7**, 13650–13657.

105 F. Han, J. Yue, X. Zhu and C. Wang, *Adv. Energy Mater.*, 2018, **8**, 1703644.

106 Y.-H. Cho, J. Wolfenstine, E. Rangasamy, H. Kim, H. Choe and J. Sakamoto, *J. Mater. Sci.*, 2012, **47**, 5970–5977.

107 A. Sakuda, A. Hayashi, Y. Takigawa, K. Higashi and M. Tatsumisago, *J. Ceram. Soc. Jpn.*, 2013, **121**, 946–949.

108 F. P. McGrogan, T. Swamy, S. R. Bishop, E. Eggleton, L. Porz, X. Chen, Y.-M. Chiang and K. J. Van Vliet, *Adv. Energy Mater.*, 2017, **7**, 1602011.

109 T. Kelly, B. M. Ghadi, S. Berg and H. Ardebili, *Sci. Rep.*, 2016, **6**, 20128.

110 S.-O. Tung, S. Ho, M. Yang, R. Zhang and N. A. Kotov, *Nat. Commun.*, 2015, **6**, 6152.

111 M. Rosso, C. Brissot, A. Teyssot, M. Dollé, L. Sannier, J.-M. Tarascon, R. Bouchet and S. Lascaud, *Electrochim. Acta*, 2006, **51**, 5334–5340.

112 M. L. Dollé, L. Sannier, B. Beaudoin, M. Trentin and J.-M. Tarascon, *Electrochem. Solid-State Lett.*, 2002, **5**, A286–A289.

113 L. Frenck, G. K. Sethi, J. A. Maslyn and N. P. Balsara, *Front. Energy Res.*, 2019, **7**, 115.

114 G. Stone, S. Mullin, A. Teran, D. Hallinan Jr, A. Minor, A. Hexemer and N. Balsara, *J. Electrochem. Soc.*, 2012, **159**, A222–A227.

115 D. Lin, P. Y. Yuen, Y. Liu, W. Liu, N. Liu, R. H. Dauskardt and Y. Cui, *Adv. Mater.*, 2018, **30**, 1802661.

116 H. Wu, Y. Cao, H. Su and C. Wang, *Angew. Chem., Int. Ed.*, 2018, **57**, 1361–1365.

117 F. Alloin, A. D'Aprea, N. E. Kissi, A. Dufresne and F. Bossard, *Electrochim. Acta*, 2010, **55**, 5186–5194.

118 J. Ji, B. Li and W.-H. Zhong, *Electrochim. Acta*, 2010, **55**, 9075–9082.

119 P. Barai, K. Higa and V. Srinivasan, *Phys. Chem. Chem. Phys.*, 2017, **19**, 20493–20505.

120 C. Monroe and J. Newman, *J. Electrochem. Soc.*, 2003, **150**, A1377–A1384.

121 A.-Y. Jee, H. Lee, Y. Lee and M. Lee, *Chem. Phys.*, 2013, **422**, 246–250.

122 Q. Li, H. Y. Sun, Y. Takeda, N. Imanishi, J. Yang and O. Yamamoto, *J. Power Sources*, 2001, **94**, 201–205.

123 C. Brissot, M. Rosso, J. N. Chazalviel and S. Lascaud, *J. Power Sources*, 1999, **81–82**, 925–929.

124 S. Liu, N. Imanishi, T. Zhang, A. Hirano, Y. Takeda, O. Yamamoto and J. Yang, *J. Electrochem. Soc.*, 2010, **157**, A1092–A1098.

125 K. J. Harry, K. Higa, V. Srinivasan and N. P. Balsara, *J. Electrochem. Soc.*, 2016, **163**, A2216–A2224.

126 N. S. Schauser, K. J. Harry, D. Y. Parkinson, H. Watanabe and N. P. Balsara, *J. Electrochem. Soc.*, 2015, **162**, A398–A405.

127 K. J. Harry, D. T. Hallinan, D. Y. Parkinson, A. A. MacDowell and N. P. Balsara, *Nat. Mater.*, 2014, **13**, 69–73.

128 M. Rosso, T. Gobron, C. Brissot, J. N. Chazalviel and S. Lascaud, *J. Power Sources*, 2001, **97–98**, 804–806.

129 R. Khurana, J. L. Schaefer, L. A. Archer and G. W. Coates, *J. Am. Chem. Soc.*, 2014, **136**, 7395–7402.

130 K. N. Wood, M. Noked and N. P. Dasgupta, *ACS Energy Lett.*, 2017, **2**, 664–672.

131 C. Fang, J. Li, M. Zhang, Y. Zhang, F. Yang, J. Z. Lee, M.-H. Lee, J. Alvarado, M. A. Schroeder, Y. Yang, B. Lu, N. Williams, M. Ceja, L. Yang, M. Cai, J. Gu, K. Xu, X. Wang and Y. S. Meng, *Nature*, 2019, **572**, 511–515.

132 J.-I. Yamaki, S.-I. Tobishima, K. Hayashi, S. Keiichi, Y. Nemoto and M. Arakawa, *J. Power Sources*, 1998, **74**, 219–227.

133 C. Wang, Y. Gong, J. Dai, L. Zhang, H. Xie, G. Pastel, B. Liu, E. Wachsman, H. Wang and L. Hu, *J. Am. Chem. Soc.*, 2017, **139**, 14257–14264.

134 B. Wu, S. Wang, W. J. Evans Iv, D. Z. Deng, J. Yang and J. Xiao, *J. Mater. Chem. A*, 2016, **4**, 15266–15280.

135 S. Lou, F. Zhang, C. Fu, M. Chen, Y. Ma, G. Yin and J. Wang, *Adv. Mater.*, 2020, 2000721, DOI: 10.1002/adma.202000721.

136 Y. Zhu, X. He and Y. Mo, *ACS Appl. Mater. Interfaces*, 2015, **7**, 23685–23693.

137 W. D. Richards, L. J. Miara, Y. Wang, J. C. Kim and G. Ceder, *Chem. Mater.*, 2016, **28**, 266–273.

138 T. Krauskopf, H. Hartmann, W. G. Zeier and J. Janek, *ACS Appl. Mater. Interfaces*, 2019, **11**, 14463–14477.

139 D. Spencer Jolly, Z. Ning, J. E. Darnbrough, J. Kasemchainan, G. O. Hartley, P. Adamson, D. E. J. Armstrong, J. Marrow and P. G. Bruce, *ACS Appl. Mater. Interfaces*, 2020, **12**, 678–685.

140 M. J. Wang, R. Choudhury and J. Sakamoto, *Joule*, 2019, **3**, 2165–2178.

141 D. P. Wilkinson, H. Blom, K. Brandt and D. Wainwright, *J. Power Sources*, 1991, **36**, 517–527.

142 T. Hirai, I. Yoshimatsu and J. Yamaki, *J. Electrochem. Soc.*, 1994, **141**, 611–614.

143 A. Louli, M. Genovese, R. Weber, S. Hames, E. Logan and J. Dahn, *J. Electrochem. Soc.*, 2019, **166**, A1291–A1299.

144 X. Zhang, Q. Wang, K. Harrison, K. Jungjohann, B. Boyce, S. Roberts, P. Attia and S. Harris, *J. Electrochem. Soc.*, 2019, **166**, 3639–3652.

145 J.-M. Doux, H. Nguyen, D. H. S. Tan, A. Banerjee, X. Wang, E. A. Wu, C. Jo, H. Yang and Y. S. Meng, *Adv. Energy Mater.*, 2020, **10**, 1903253.

146 F. Wu, W. Fitzhugh, L. Ye, J. Ning and X. Li, *Nat. Commun.*, 2018, **9**, 4037.

147 W. Fitzhugh, F. Wu, L. Ye, H. Su and X. Li, *Small*, 2019, **15**, 1901470.

148 Y. Su, L. Ye, W. Fitzhugh, Y. Wang, E. Gil-González, I. Kim and X. Li, *Energy Environ. Sci.*, 2020, **13**, 908–916.

149 H. Huo, J. Luo, V. Thangadurai, X. Guo, C.-W. Nan and X. Sun, *ACS Energy Lett.*, 2020, **5**, 252–262.

150 X. Fu, T. Wang, W. Shen, M. Jiang, Y. Wang, Q. Dai, D. Wang, Z. Qiu, Y. Zhang, K. Deng, Q. Zeng, N. Zhao, X. Guo, Z. Liu, J. Liu and Z. Peng, *Adv. Mater.*, 2020, **32**, 2000575.

151 M. Wang and J. Sakamoto, *J. Power Sources*, 2018, **377**, 7–11.

152 A. Sharafi, E. Kazyak, A. L. Davis, S. Yu, T. Thompson, D. J. Siegel, N. P. Dasgupta and J. Sakamoto, *Chem. Mater.*, 2017, **29**, 7961–7968.

153 H. Zheng, S. Wu, R. Tian, Z. Xu, H. Zhu, H. Duan and H. Liu, *Adv. Funct. Mater.*, 2020, **30**, 1906189.

154 W. Luo, Y. Gong, Y. Zhu, K. K. Fu, J. Dai, S. D. Lacey, C. Wang, B. Liu, X. Han, Y. Mo, E. D. Wachsman and L. Hu, *J. Am. Chem. Soc.*, 2016, **138**, 12258–12262.

155 C.-L. Tsai, V. Roddatis, C. V. Chandran, Q. Ma, S. Uhlenbruck, M. Bram, P. Heitjans and O. Guillon, *ACS Appl. Mater. Interfaces*, 2016, **8**, 10617–10626.

156 W. Feng, X. Dong, P. Li, Y. Wang and Y. Xia, *J. Power Sources*, 2019, **419**, 91–98.

157 W. Feng, X. Dong, Z. Lai, X. Zhang, Y. Wang, C. Wang, J. Luo and Y. Xia, *ACS Energy Lett.*, 2019, **4**, 1725–1731.

158 W. Luo, Y. Gong, Y. Zhu, Y. Li, Y. Yao, Y. Zhang, K. Fu, G. Pastel, C.-F. Lin, Y. Mo, E. D. Wachsman and L. Hu, *Adv. Mater.*, 2017, **29**, 1606042.

159 C. Wang, H. Xie, L. Zhang, Y. Gong, G. Pastel, J. Dai, B. Liu, E. D. Wachsman and L. Hu, *Adv. Energy Mater.*, 2018, **8**, 1701963.

160 H. Huo, Y. Chen, R. Li, N. Zhao, J. Luo, J. G. Pereira da Silva, R. Mücke, P. Kaghazchi, X. Guo and X. Sun, *Energy Environ. Sci.*, 2020, **13**, 127–134.

161 J. Fu, P. Yu, N. Zhang, G. Ren, S. Zheng, W. Huang, X. Long, H. Li and X. Liu, *Energy Environ. Sci.*, 2019, **12**, 1404–1412.

162 H. Xu, Y. Li, A. Zhou, N. Wu, S. Xin, Z. Li and J. B. Goodenough, *Nano Lett.*, 2018, **18**, 7414–7418.

163 C. Wang, Y. Gong, B. Liu, K. Fu, Y. Yao, E. Hitz, Y. Li, J. Dai, S. Xu, W. Luo, E. D. Wachsman and L. Hu, *Nano Lett.*, 2017, **17**, 565–571.

164 Y. Zhang, J. Meng, K. Chen, H. Wu, J. Hu and C. Li, *ACS Energy Lett.*, 2020, **5**, 1167–1176.

165 Y. Li, X. Chen, A. Dolocan, Z. Cui, S. Xin, L. Xue, H. Xu, K. Park and J. B. Goodenough, *J. Am. Chem. Soc.*, 2018, **140**, 6448–6455.

166 H. Huo, Y. Chen, N. Zhao, X. Lin, J. Luo, X. Yang, Y. Liu, X. Guo and X. Sun, *Nano Energy*, 2019, **61**, 119–125.

167 A. Gupta and J. Sakamoto, *Electrochem. Soc. Interface*, 2019, **28**, 63–69.

168 A. Sharafi, H. M. Meyer, J. Nanda, J. Wolfenstine and J. Sakamoto, *J. Power Sources*, 2016, **302**, 135–139.

169 X. Han, Y. Gong, K. Fu, X. He, G. T. Hitz, J. Dai, A. Pearse, B. Liu, H. Wang, G. Rubloff, Y. Mo, V. Thangadurai, E. D. Wachsman and L. Hu, *Nat. Mater.*, 2017, **16**, 572–579.

170 B. Wu, S. Wang, J. Lochala, D. Desrochers, B. Liu, W. Zhang, J. Yang and J. Xiao, *Energy Environ. Sci.*, 2018, **11**, 1803–1810.

171 S. Xu, D. W. McOwen, L. Zhang, G. T. Hitz, C. Wang, Z. Ma, C. Chen, W. Luo, J. Dai, Y. Kuang, E. M. Hitz, K. Fu, Y. Gong, E. D. Wachsman and L. Hu, *Energy Storage Mater.*, 2018, **15**, 458–464.

172 N. Eustathopoulos and R. Voytovych, *J. Mater. Sci.*, 2016, **51**, 425–437.

173 J. Duan, W. Wu, A. M. Nolan, T. Wang, J. Wen, C. Hu, Y. Mo, W. Luo and Y. Huang, *Adv. Mater.*, 2019, **31**, 1807243.

174 Y. Huang, B. Chen, J. Duan, F. Yang, T. Wang, Z. Wang, W. Yang, C. Hu, W. Luo and Y. Huang, *Angew. Chem., Int. Ed.*, 2020, **59**, 3699–3704.

175 J. Wen, Y. Huang, J. Duan, Y. Wu, W. Luo, L. Zhou, C. Hu, L. Huang, X. Zheng, W. Yang, Z. Wen and Y. Huang, *ACS Nano*, 2019, **13**, 14549–14556.

176 Y. Shao, H. Wang, Z. Gong, D. Wang, B. Zheng, J. Zhu, Y. Lu, Y.-S. Hu, X. Guo, H. Li, X. Huang, Y. Yang, C.-W. Nan and L. Chen, *ACS Energy Lett.*, 2018, **3**, 1212–1218.

177 S.-H. Wang, J. Yue, W. Dong, T.-T. Zuo, J.-Y. Li, X. Liu, X.-D. Zhang, L. Liu, J.-L. Shi, Y.-X. Yin and Y.-G. Guo, *Nat. Commun.*, 2019, **10**, 4930.

178 L. Cheng, W. Chen, M. Kunz, K. Persson, N. Tamura, G. Chen and M. Doeff, *ACS Appl. Mater. Interfaces*, 2015, **7**, 2073–2081.

179 Y. Nomura, K. Yamamoto, T. Hirayama, E. Igaki and K. Saitoh, *ACS Energy Lett.*, 2020, **5**, 2098–2105.

180 Y. Nomura, K. Yamamoto, M. Fujii, T. Hirayama, E. Igaki and K. Saitoh, *Nat. Commun.*, 2020, **11**, 2824.

181 A. C. Buechele, L. C. De Jonghe and D. Hitchcock, *J. Electrochem. Soc.*, 1983, **130**, 1042–1049.

182 S. Wenzel, T. Leichtweiss, D. Krüger, J. Sann and J. Janek, *Solid State Ionics*, 2015, **278**, 98–105.

183 Y. Zhu, X. He and Y. Mo, *J. Mater. Chem. A*, 2016, **4**, 3253–3266.

184 C. H. Chen and K. Amine, *Solid State Ionics*, 2001, **144**, 51–57.

185 X. Xu, Z. Wen, X. Yang, J. Zhang and Z. Gu, *Solid State Ionics*, 2006, **177**, 2611–2615.

186 I. Kokal, M. Somer, P. H. L. Notten and H. T. Hintzen, *Solid State Ionics*, 2011, **185**, 42–46.

187 A. Wang, S. Kadam, H. Li, S. Shi and Y. Qi, *npj Comput. Mater.*, 2018, **4**, 15.

188 E. Peled, *J. Electrochem. Soc.*, 1979, **126**, 2047–2051.

189 J. Steiger, D. Kramer and R. Mönig, *J. Power Sources*, 2014, **261**, 112–119.

190 E. Peled and S. Menkin, *J. Electrochem. Soc.*, 2017, **164**, A1703–A1719.

191 X.-B. Cheng, R. Zhang, C.-Z. Zhao and Q. Zhang, *Chem. Rev.*, 2017, **117**, 10403–10473.

192 H. Chung and B. Kang, *Chem. Mater.*, 2017, **29**, 8611–8619.

193 S. Wenzel, D. A. Weber, T. Leichtweiss, M. R. Busche, J. Sann and J. Janek, *Solid State Ionics*, 2016, **286**, 24–33.

194 S. Wenzel, S. Randau, T. Leichtweiß, D. A. Weber, J. Sann, W. G. Zeier and J. Janek, *Chem. Mater.*, 2016, **28**, 2400–2407.

195 S. Wang, H. Xu, W. Li, A. Dolocan and A. Manthiram, *J. Am. Chem. Soc.*, 2018, **140**, 250–257.

196 X. Yu, J. B. Bates, G. E. Jellison Jr and F. X. Hart, *J. Electrochem. Soc.*, 1997, **144**, 524–532.

197 X. Lü, G. Wu, J. W. Howard, A. Chen, Y. Zhao, L. L. Daemen and Q. Jia, *Chem. Commun.*, 2014, **50**, 11520–11522.

198 M. H. Braga, J. A. Ferreira, V. Stockhausen, J. E. Oliveira and A. El-Azab, *J. Mater. Chem. A*, 2014, **2**, 5470–5480.

199 P. Hartmann, T. Leichtweiss, M. R. Busche, M. Schneider, M. Reich, J. Sann, P. Adelhelm and J. Janek, *J. Phys. Chem. C*, 2013, **117**, 21064–21074.

200 S. P. Ong, Y. Mo, W. D. Richards, L. Miara, H. S. Lee and G. Ceder, *Energy Environ. Sci.*, 2013, **6**, 148–156.

201 L. He, Q. Sun, C. Chen, J. A. S. Oh, J. Sun, M. Li, W. Tu, H. Zhou, K. Zeng and L. Lu, *ACS Appl. Mater. Interfaces*, 2019, **11**, 20895–20904.

202 Y. Xiao, Y. Wang, S.-H. Bo, J. C. Kim, L. J. Miara and G. Ceder, *Nat. Rev. Mater.*, 2020, **5**, 105–126.

203 M. Kotobuki, H. Munakata, K. Kanamura, Y. Sato and T. Yoshida, *J. Electrochem. Soc.*, 2010, **157**, A1076–A1079.

204 J. Wolfenstine, J. L. Allen, J. Read and J. Sakamoto, *J. Mater. Sci.*, 2013, **48**, 5846–5851.

205 C. Ma, Y. Cheng, K. Yin, J. Luo, A. Sharafi, J. Sakamoto, J. Li, K. L. More, N. J. Dudney and M. Chi, *Nano Lett.*, 2016, **16**, 7030–7036.

206 X. Tao, Y. Liu, W. Liu, G. Zhou, J. Zhao, D. Lin, C. Zu, O. Sheng, W. Zhang, H.-W. Lee and Y. Cui, *Nano Lett.*, 2017, **17**, 2967–2972.

207 Y. Shen, Y. Zhang, S. Han, J. Wang, Z. Peng and L. Chen, *Joule*, 2018, **2**, 1674–1689.

208 R. Chen, A. M. Nolan, J. Lu, J. Wang, X. Yu, Y. Mo, L. Chen, X. Huang and H. Li, *Joule*, 2020, **4**, 812–821.

209 J. A. Lewis, F. J. Q. Cortes, M. G. Boebinger, J. Tippens, T. S. Marchese, N. Kondekar, X. Liu, M. Chi and M. T. McDowell, *ACS Energy Lett.*, 2019, **4**, 591–599.

210 J. Zhu, J. Zhao, Y. Xiang, M. Lin, H. Wang, B. Zheng, H. He, Q. Wu, J. Y. Huang and Y. Yang, *Chem. Mater.*, 2020, **32**, 4998–5008.

211 P. Bron, B. Roling and S. Dehnen, *J. Power Sources*, 2017, **352**, 127–134.

212 A. L. Davis, R. Garcia-Mendez, K. N. Wood, E. Kazyak, K.-H. Chen, G. Teeter, J. Sakamoto and N. P. Dasgupta, *J. Mater. Chem. A*, 2020, **8**, 6291–6302.

213 F. Han, T. Gao, Y. Zhu, K. J. Gaskell and C. Wang, *Adv. Mater.*, 2015, **27**, 3473–3483.

214 F. Han, Y. Zhu, X. He, Y. Mo and C. Wang, *Adv. Energy Mater.*, 2016, **6**, 1501590.

215 Z. Liu, A. Borodin, G. Li, X. Liu, Y. Li and F. Endres, *J. Phys. Chem. C*, 2020, **124**, 300–308.

216 Y. Wang, D. Lu, J. Xiao, Y. He, G. J. Harvey, C. Wang, J.-G. Zhang and J. Liu, *Energy Storage Mater.*, 2019, **19**, 80–87.

217 C. Wang, Y. Yang, X. Liu, H. Zhong, H. Xu, Z. Xu, H. Shao and F. Ding, *ACS Appl. Mater. Interfaces*, 2017, **9**, 13694–13702.

218 W. Zhou, S. Wang, Y. Li, S. Xin, A. Manthiram and J. B. Goodenough, *J. Am. Chem. Soc.*, 2016, **138**, 9385–9388.

219 Y. Jin, C. Liu, X. Zong, D. Li, M. Fu, S. Tan, Y. Xiong and J. Wei, *J. Power Sources*, 2020, **460**, 228125.

220 Z. Zhang, Y. Zhao, S. Chen, D. Xie, X. Yao, P. Cui and X. Xu, *J. Mater. Chem. A*, 2017, **5**, 16984–16993.

221 Z. Yang, H. Yuan, C. Zhou, Y. Wu, W. Tang, S. Sang and H. Liu, *Chem. Eng. J.*, 2020, **392**, 123650.

222 D. Bosubabu, J. Sivaraj, R. Sampathkumar and K. Ramesha, *ACS Appl. Energy Mater.*, 2019, **2**, 4118–4125.

223 J.-Y. Liang, X.-X. Zeng, X.-D. Zhang, T.-T. Zuo, M. Yan, Y.-X. Yin, J.-L. Shi, X.-W. Wu, Y.-G. Guo and L.-J. Wan, *J. Am. Chem. Soc.*, 2019, **141**, 9165–9169.

224 Y. Liu, Q. Sun, Y. Zhao, B. Wang, P. Kaghazchi, K. R. Adair, R. Li, C. Zhang, J. Liu, L.-Y. Kuo, Y. Hu, T.-K. Sham, L. Zhang, R. Yang, S. Lu, X. Song and X. Sun, *ACS Appl. Mater. Interfaces*, 2018, **10**, 31240–31248.

225 H. Bai, J. Hu, Y. Duan, T. Kozawa, M. Naito, J. Zhang and S. Dong, *Ceram. Int.*, 2019, **45**, 14663–14668.

226 C. Wang, G. Bai, Y. Yang, X. Liu and H. Shao, *Nano Res.*, 2019, **12**, 217–223.

227 H. S. Jadhav, R. S. Kalubarme, A. H. Jadhav and J. G. Seo, *Electrochim. Acta*, 2016, **199**, 126–132.

228 L. Sang, K. L. Bassett, F. C. Castro, M. J. Young, L. Chen, R. T. Haasch, J. W. Elam, V. P. Dravid, R. G. Nuzzo and A. A. Gewirth, *Chem. Mater.*, 2018, **30**, 8747–8756.

229 C. Wang, Y. Zhao, Q. Sun, X. Li, Y. Liu, J. Liang, X. Li, X. Lin, R. Li, K. R. Adair, L. Zhang, R. Yang, S. Lu and X. Sun, *Nano Energy*, 2018, **53**, 168–174.

230 Y. Li, W. Zhou, X. Chen, X. Lü, Z. Cui, S. Xin, L. Xue, Q. Jia and J. B. Goodenough, *Proc. Natl. Acad. Sci. U. S. A.*, 2016, **113**, 13313–13317.

231 Q. Liu, Q. Yu, S. Li, S. Wang, L. Zhang, B. Cai, D. Zhou and B. Li, *Energy Storage Mater.*, 2020, **25**, 613–620.

232 X. Fan, X. Ji, F. Han, J. Yue, J. Chen, L. Chen, T. Deng, J. Jiang and C. Wang, *Sci. Adv.*, 2018, **4**, eaau9245.

233 Z. Zhang, S. Chen, J. Yang, J. Wang, L. Yao, X. Yao, P. Cui and X. Xu, *ACS Appl. Mater. Interfaces*, 2018, **10**, 2556–2565.

234 M. Suyama, A. Kato, A. Sakuda, A. Hayashi and M. Tatsumisago, *Electrochim. Acta*, 2018, **286**, 158–162.

235 E. Rangasamy, Z. Liu, M. Gobet, K. Pilar, G. Sahu, W. Zhou, H. Wu, S. Greenbaum and C. Liang, *J. Am. Chem. Soc.*, 2015, **137**, 1384–1387.

236 Y. Liu, C. Li, B. Li, H. Song, Z. Cheng, M. Chen, P. He and H. Zhou, *Adv. Energy Mater.*, 2018, **8**, 1702374.

237 H. Zhong, L. Sang, F. Ding, J. Song and Y. Mai, *Electrochim. Acta*, 2018, **277**, 268–275.

238 F. J. Q. Cortes, J. A. Lewis, J. Tippens, T. S. Marchese and M. T. McDowell, *J. Electrochem. Soc.*, 2020, **167**, 050502.

239 B. R. Shin, Y. J. Nam, D. Y. Oh, D. H. Kim, J. W. Kim and Y. S. Jung, *Electrochim. Acta*, 2014, **146**, 395–402.

240 M. Nagao, A. Hayashi and M. Tatsumisago, *Electrochemistry*, 2012, **80**, 734–736.

241 M. Tatsumisago, F. Mizuno and A. Hayashi, *J. Power Sources*, 2006, **159**, 193–199.

242 I. Ismail, A. Noda, A. Nishimoto and M. Watanabe, *Electrochim. Acta*, 2001, **46**, 1595–1603.

243 M. Le Granvalet-Mancini, T. Hanrath and D. Teeters, *Solid State Ionics*, 2000, **135**, 283–290.

244 P. G. Bruce and F. Krok, *Solid State Ionics*, 1989, **36**, 171–174.

245 C. A. Vincent, *Prog. Solid State Chem.*, 1987, **17**, 145–261.

246 D. Aurbach and E. Granot, *Electrochim. Acta*, 1997, **42**, 697–718.

247 D. Aurbach, M. L. Daroux, P. W. Faguy and E. Yeager, *J. Electrochem. Soc.*, 1988, **135**, 1863–1871.

248 A. Lisowska-Oleksiak, *Solid State Ionics*, 1999, **119**, 205–209.

249 D. Fauteux, *J. Electrochem. Soc.*, 1988, **135**, 2231–2237.

250 D. Aurbach, *J. Power Sources*, 2000, **89**, 206–218.

251 D. Fauteux, *Solid State Ionics*, 1985, **17**, 133–138.

252 C. Xu, B. Sun, T. Gustafsson, K. Edström, D. Brandell and M. Hahlin, *J. Mater. Chem. A*, 2014, **2**, 7256–7264.

253 M. D. Galluzzo, D. M. Halat, W. S. Loo, S. A. Mullin, J. A. Reimer and N. P. Balsara, *ACS Energy Lett.*, 2019, **4**, 903–907.

254 S. Kalnaus, A. S. Sabau, W. E. Tenhaeff, N. J. Dudney and C. Daniel, *J. Power Sources*, 2012, **201**, 280–287.

255 G. X. Wang, L. Yang, J. Z. Wang, H. K. Liu and S. X. Dou, *J. Nanosci. Nanotechnol.*, 2005, **5**, 1135–1140.

256 D. Lin, W. Liu, Y. Liu, H. R. Lee, P.-C. Hsu, K. Liu and Y. Cui, *Nano Lett.*, 2016, **16**, 459–465.

257 J. Zhang, N. Zhao, M. Zhang, Y. Li, P. K. Chu, X. Guo, Z. Di, X. Wang and H. Li, *Nano Energy*, 2016, **28**, 447–454.

258 Y.-J. Wang, Y. Pan and D. Kim, *J. Power Sources*, 2006, **159**, 690–701.

259 M. C. Borghini, M. Mastragostino, S. Passerini and B. Scrosati, *J. Electrochem. Soc.*, 1995, **142**, 2118–2121.

260 J.-H. Shin and S. Passerini, *Electrochim. Acta*, 2004, **49**, 1605–1612.

261 M. Chintapalli, T. N. P. Le, N. R. Venkatesan, N. G. Mackay, A. A. Rojas, J. L. Thelen, X. C. Chen, D. Devaux and N. P. Balsara, *Macromolecules*, 2016, **49**, 1770–1780.

262 N. S. Wanakule, A. Panday, S. A. Mullin, E. Gann, A. Hexemer and N. P. Balsara, *Macromolecules*, 2009, **42**, 5642–5651.

263 A. B. Puthirath, S. Patra, S. Pal, M. Manoj, A. Puthirath-Balan, S. Jayalekshmi and N. Tharangattu N, *J. Mater. Chem. A*, 2017, **5**, 11152–11162.

264 M. Patel and A. J. Bhattacharyya, *Electrochem. Commun.*, 2008, **10**, 1912–1915.

265 H. Li, M. Li, S. H. Siyal, M. Zhu, J.-L. Lan, G. Sui, Y. Yu, W. Zhong and X. Yang, *J. Membr. Sci.*, 2018, **555**, 169–176.

266 O. Chusid, Y. Gofer, D. Aurbach, M. Watanabe, T. Momma and T. Osaka, *J. Power Sources*, 2001, **97–98**, 632–636.

267 N. R. Brown, T. Makkapati and D. Teeters, *Solid State Ionics*, 2016, **288**, 207–212.

268 R. N. Mason, M. Smith, T. Andrews and D. Teeters, *Solid State Ionics*, 1999, **118**, 129–133.

269 C. Wang, H. Zhang, J. Li, J. Chai, S. Dong and G. Cui, *J. Power Sources*, 2018, **397**, 157–161.

270 K. N. Wood, K. X. Steirer, S. E. Hafner, C. Ban, S. Santhanagopalan, S.-H. Lee and G. Teeter, *Nat. Commun.*, 2018, **9**, 2490.

271 Y. Li, Z. Gao, F. Hu, X. Lin, Y. Wei, J. Peng, J. Yang, Z. Li, Y. Huang and H. Ding, *Small Methods*, 2020, **4**, 2000111.

272 Q. Liu, L. Zhang, H. Sun, L. Geng, Y. Li, Y. Tang, P. Jia, Z. Wang, Q. Dai, T. Shen, Y. Tang, T. Zhu and J. Huang, *ACS Energy Lett.*, 2020, **5**, 2546–2559.

273 Y. Li, Y. Li, A. Pei, K. Yan, Y. Sun, C.-L. Wu, L.-M. Joubert, R. Chin, A. L. Koh, Y. Yu, J. Perrino, B. Butz, S. Chu and Y. Cui, *Science*, 2017, **358**, 506–510.

274 X. Wang, M. Zhang, J. Alvarado, S. Wang, M. Sina, B. Lu, J. Bouwer, W. Xu, J. Xiao, J.-G. Zhang, J. Liu and Y. S. Meng, *Nano Lett.*, 2017, **17**, 7606–7612.

275 X. Wang, Y. Li and Y. S. Meng, *Joule*, 2018, **2**, 2225–2234.

276 M. J. Zachman, Z. Tu, S. Choudhury, L. A. Archer and L. F. Kourkoutis, *Nature*, 2018, **560**, 345–349.

277 F. Orsini, A. du Pasquier, B. Beaudouin, J. M. Tarascon, M. Trentin, N. Langenhuizen, E. de Beer and P. Notten, *J. Power Sources*, 1999, **81–82**, 918–921.

278 M. Golozar, A. Paolella, H. Demers, S. Bessette, M. Lagacé, P. Bouchard, A. Guerfi, R. Gauvin and K. Zaghib, *Commun. Chem.*, 2019, **2**, 131.

279 S. J. Harris, A. Timmons, D. R. Baker and C. Monroe, *Chem. Phys. Lett.*, 2010, **485**, 265–274.

280 Y.-S. Hong, N. Li, H. Chen, P. Wang, W.-L. Song and D. Fang, *Energy Storage Mater.*, 2018, **11**, 118–126.

281 K. N. Wood, E. Kazyak, A. F. Chadwick, K.-H. Chen, J.-G. Zhang, K. Thornton and N. P. Dasgupta, *ACS Cent. Sci.*, 2016, **2**, 790–801.

282 F. Shen, M. B. Dixit, X. Xiao and K. B. Hatzell, *ACS Energy Lett.*, 2018, **3**, 1056–1061.

283 J. Tippens, J. C. Miers, A. Afshar, J. A. Lewis, F. J. Q. Cortes, H. Qiao, T. S. Marchese, C. V. Di Leo, C. Saldana and M. T. McDowell, *ACS Energy Lett.*, 2019, **4**, 1475–1483.

284 S.-H. Yu, X. Huang, J. D. Brock and H. D. Abruña, *J. Am. Chem. Soc.*, 2019, **141**, 8441–8449.

285 Q. Li, T. Yi, X. Wang, H. Pan, B. Quan, T. Liang, X. Guo, X. Yu, H. Wang, X. Huang, L. Chen and H. Li, *Nano Energy*, 2019, **63**, 103895.

286 M. Liu, Z. Cheng, K. Qian, T. Verhallen, C. Wang and M. Wagemaker, *Chem. Mater.*, 2019, **31**, 4564–4574.

287 S. Lv, T. Verhallen, A. Vasileiadis, F. Ooms, Y. Xu, Z. Li, Z. Li and M. Wagemaker, *Nat. Commun.*, 2018, **9**, 2152.

288 F. Aguesse, W. Manalastas, L. Buannic, J. M. Lopez del Amo, G. Singh, A. Llordés and J. Kilner, *ACS Appl. Mater. Interfaces*, 2017, **9**, 3808–3816.

289 R. Bhattacharyya, B. Key, H. Chen, A. S. Best, A. F. Hollenkamp and C. P. Grey, *Nat. Mater.*, 2010, **9**, 504–510.

290 L. E. Marbella, S. Zekoll, J. Kasemchainan, S. P. Emge, P. G. Bruce and C. P. Grey, *Chem. Mater.*, 2019, **31**, 2762–2769.

291 M. Wang, J. B. Wolfenstine and J. Sakamoto, *Electrochim. Acta*, 2019, **296**, 842–847.

292 C. Yang, H. Xie, W. Ping, K. Fu, B. Liu, J. Rao, J. Dai, C. Wang, G. Pastel and L. Hu, *Adv. Mater.*, 2019, **31**, 1804815.

293 Y. Song, L. Yang, W. Zhao, Z. Wang, Y. Zhao, Z. Wang, Q. Zhao, H. Liu and F. Pan, *Adv. Energy Mater.*, 2019, **9**, 1900671.

294 L. Chen, Y. Li, S.-P. Li, L.-Z. Fan, C.-W. Nan and J. B. Goodenough, *Nano Energy*, 2018, **46**, 176–184.

295 Y.-C. Hsieh, M. Leißing, S. Nowak, B.-J. Hwang, M. Winter and G. Brunklaus, *Cell Rep. Phys. Sci.*, 2020, **1**, 100139.